UC Santa Barbara
UC Santa Barbara Electronic Theses and Dissertations

Title

Elucidating Phosphate Cluster Formation Mechanisms through Nuclear Magnetic Resonance

Permalink

https://escholarship.org/uc/item/44t6964v

Author

Nowotarski, Mesopotamia S.

Publication Date

2023

Peer reviewed|Thesis/dissertation

University of California
Santa Barbara

Elucidating Phosphate Cluster Formation Mechanisms through Nuclear Magnetic Resonance

A dissertation submitted in partial satisfaction
of the requirements for the degree

Doctor of Philosophy

in

Chemistry

by

Mesopotamia S. Nowotarski

Committee in charge:

Professor Songi Han, Co-chair
Professor Matthew Fisher, Co-chair
Professor Bradley Chmelka
Professor Matthew Helgeson
Professor Arnab Mukherjee

September 2023

The Dissertation of Mesopotamia S. Nowotarski is approved.

Professor Bradley Chmelka

Professor Matthew Helgeson

Professor Arnab Mukherjee

Professor Matthew Fisher, Committee Co-chair

Professor Songi Han, Committee Co-chair

August 2023

Elucidating Phosphate Cluster Formation Mechanisms through Nuclear Magnetic Resonance

Dedication

In loving memory of my mother, MaryAnn Nowotarski. She supported me throughout my entire PhD and life, and was the best mother one could have. She was a lifelong learner herself and remains an inspiration.

Acknowledgements

I would like to express my sincere gratitude to my parents, James and MaryAnn Nowotarski; They have supported me through thick and thin. My cat, Kish, deserves a degree of her own. I would like to acknowledge my friends for all their love and support over the years including but not limited to (in no particular order): Brandon Shippy, Aleksei Khindanov, Rebecca Jindra, Tanner Hadick, Jackson Sheppard, Mark Cavalieri, Manik Goyal, Sterling St. John, Toshi Shimasaki, Dan Hajnos, Yuri Lensky, Francisco Ballesteros, Taylan Clement, and many others.

My collaborative projects have been fruitful thanks to many excellent researchers and mentors who have greatly contributed to the studies presented in this dissertation. Thank you to the entire Han lab for continuing discussions and guidance, especially Raj Chacklashiya, Dr. Michael Vigers, Dr. Tarnuma Tabassum, Dr. Miranda Li, Brittany Puzio, Dr. Khanh Nguyen, Karen Tsay, Dr. Kan Tagami, Samantha Ausman, and Thomas Webber. I truly appreciate my undergraduate students (and friends), Hunter Coffaro and Michael Lum, for going above and beyond. The most gratutude towards the post-doctoral fellows, Dr. Sheetal Jain and Dr. Lokeswara Rao Potnuru, for priceless patience and sharing of their knowledge. A special shoutout to Dr. Joshua Straub for extensive collaboration throughout our years working together on the Quantum Brain project. To my committee, I am extremely grateful for your suggestions, help, and accommodation throughout my Ph.D. To the NMR spectroscopy facility supervisors Dr. Zhou and Dr. Hu, thank you for your help and continuous accommodation of my unique requests. Having the opportunity to work on such a unique project as the Quantum Brain, I am proud and grateful for collaboration and input from all colleagues. I am also very thankful for guidance and support from Dr. Robby Nadler, in writing skills and life navigation.

Curriculum Vitæ
Mesopotamia S. Nowotarski

Education

2023	Ph.D. in Chemistry, University of California, Santa Barbara.
	NSF GRFP Fellow.
2018	B.S. in Biochemistry, Florida State University.
2018	B.S. in Environmental Science, Florida State University.

Publications

Published Manuscripts:

1. **Nowotarski, M. S.**; Straub, J. S.; Lu, J.; Sheth, T.; Jiao, S.; Fisher, M. P.; Shell, M. S.; Helgeson, M. E.; Jerschow, A.; Han, S. Phosphates form spectroscopically dark state assemblies in common aqueous solutions. *PNAS* 2022, 120, 1–10. (doi.org/10.1073/pnas.2206765120)

In Preparation Manuscripts:

1. **Nowotarski, M. S.**; Potnuru, L. R.; Straub, J. S.; Chaklashiya, R.; Shimasaki, T.; Pahari, B.; Coffaro, H.; Jain, S.; Han, S. DNP Enhanced Multiple Quantum Solid State NMR Spin Counting of Molecular Assemblies in Vitrified Solutions. Submitted *JPC Letters*, 2023.

2. Lu, J.; Straub, J. S.; **Nowotarski, M. S.**; Han, S.; Xu, X.; Jerschow, A. Spectroscopically dark phosphate features revealed by chemical exchange saturation transfer. Submitted *NMR in Biomedicine*, 2023.

3. Straub, J. S.; Patel, M.; **Nowotarski, M. S.**; Potnuru, L. R.; Fisher, M.P.A.; Helgeson, M.E. A differential lithium isotope effect on the in vitro formation of calcium phosphate. In preparation.

4. Potnuru, L. R.; Dubose, A.; **Nowotarski, M. S.**; Vigers, M.; Zhang, H.; Puzio, B.; Han, S. Phosphorylated Tau Fibrils are Stabilized by Higher Order Phosphate Arrangements: Revealed by Multiple Quantum Solid-State 31P NMR Spin Counting under DNP conditions. In preparation.

5. Straub, J. S.; Patel, M.; **Nowotarski, M. S.**; Fisher, M.P.A.; Helgeson, M.E. Direct evidence for free calcium phosphate prenucleation species in solution. In preparation.

Published Book Chapter:

1. Acquah, S. F. A.; Leonhardt, B. E.; **Nowotarski, M. S.**; Magi, J. M.; Chambliss, K. A.; Venzel, T. E. S.; Delekar, S. D.; Al-Hariri, L. A. Carbon Nanotubes and Graphene as Additives in 3D Printing. *Carbon Nanotubes - Current Progress of their Polymer Composites* 2016. (doi.org/10.5772/63419)

Abstract

Elucidating Phosphate Cluster Formation Mechanisms through Nuclear Magnetic Resonance

by

Mesopotamia S. Nowotarski

Phosphates play a ubiquitous role in biology, from structural components including cell membranes and bone to energy storage via ATP, but the solution phase space leading to the formation of phosphate clustering is not entirely understood. My work will help elucidate the role of phosphate clusters in biological solutions and the unresolved formation pathway of bone. Furthermore, my research will shed additional insight onto ^{31}P nuclei quantum mechanical properties, specifically those found in Posner Clusters of molecular formula $Ca_9(PO_4)_6$, which are implicated to function as a platform for quantum computation in cognitive processes.

This dissertation will show with solution nuclear magnetic resonance (NMR) experiments that simple phosphate species including orthophosphates, pyrophosphates, and adenosine phosphates associate into dynamic assemblies in dilute aqueous solutions that are spectroscopically "dark", highlighting a hitherto unreported property of phosphate's native state in biological solutions. This dissertation will also discuss solid state NMR spin counting experiments of calcium phosphate species at varying time points in their structural evolution that were vitrified at 100 K and show calcium phosphate prenucleation clusters with a minimum of five dipolar coupled ^{31}P atoms. These results provide a novel basis for the characterization of nonclassical growth pathways and led to developments in freeze quench instrumentation, also showcased here.

Contents

Chapter 1

Introduction

Brain activity is commonly monitored via electrophysiological activity generated by electro-chemical transmitters exchanging information between anatomically localized neurons, resulting in the formation of ionic currents [1]. While it is known that information necessary for this activity is stored within neurons, the physical means of this storage of information remains unidentified [2]. In addition to this enigmatic storage of memories, the exact chemical species composition that results in a unique ionic current is unknown [3]. My PhD work revolves around a proposal for neuronal information storage and indirectly, how neuro-electrical signals are influenced by a specific source of calcium. Understanding how memories are stored will allow for simultaneous monitoring of both the information and the resulting commands from the recruitment of this information.

It is known that the brain accesses memories via localized neurons in functionalized anatomic regions of the brain and that this information is connected via the neuronal network by transfers of electro-chemical signals [2]. This holds true except for the case when a response requires instantaneous engagement of nonlocal neuronal clusters found in multiple parts of the brain, which is not possible within the current working theory due to signal transfer time limitations [2]. The ability to globally connect information and access

multiple parts of the brain at the same time presents an interesting biophysical dilemma. A possible solution presents itself if one considers that quantum information processing may play a role in memory storage. Quantum information processing would allow for memories stored in a quantum state to non-locally communicate with quantum states in other neurons while independently firing via a process called entanglement. Quantum entanglement is an isolated, distance independent phenomenon utilized in quantum computers that connects spatially separated quantum bits (qubits) of information (similar to ones and zeros in a conventional computer but with greater computational power) stored in the form of quantum degrees of freedom, such as nuclear spins [4]. If quantum entanglement is allowing different regions of the brain to communicate through space, then global storage of information is not mutually exclusive to storage in localized regions of the brain. While evidence suggests that quantum mechanics is operational in certain biological systems [5], the possibility of mammalian brain quantum computing has largely been ignored due to the need to identify a stable biogenic species that can both store and readout quantum information in the form of qubits for sufficiently long times as well as connect spatially separate neurons via biologically isolated, entangled quantum states.

Demonstrating that quantum information processing plays a role in the human brain is a daunting challenge that also requires a model for transport of quantum information stored in the qubits throughout the brain and for a quantum-to-biochemical readout that influences how neurons fire. While a theory of orchestrated objective reduction was presented by Sir Roger Penrose and Stuart Hameroff in 1998 [6], where neuronal microtubules were proposed to store and process information and memory in a quantum state allowing for quantum entanglement timescales up to 500 ms, objective reduction has yet to be proven. The key to solving this mystery of quantum information processing occurred when Dr. Matthew Fisher, 2015 Oliver Buckley Prize in Condensed Matter Physics awardee and my co-advisor, proposed that the nuclear spin states of biologically

abundant phosphorus atoms in a compound of molecular formula $Ca_9(PO_4)_6$, could serve as rudimentary, biologically optimized quantum entangled bits of information in the brain [7]. The isolated ^{31}P nuclear spins in this molecule, named as a Posner cluster (PC), provide the singular, biologically relevant, protected nuclear spin environment for quantum computation with the necessary lifetimes of information storage [7]. These molecules have been proposed to propagate through the brain via mitochondrial fission and fusion, resulting in physical transport of information throughout the brain while maintaining nonlocal quantum entanglement [8]. The memories stored in PCs integrate into the current framework of brain electro-chemical signaling as the information stored in PCs is transferred into a biochemical signal via pH modulated disassociation. This dissociation results in the release of Ca^{+2}, and subsequent calcium mediated release of the neurotransmitter glutamate from presynaptic neurons [9]. This ionic calcium release may moderate synaptic activity via established neurochemical Ca^{+2} signaling pathways [7, 10].

Proposal of quantum cognition emerged from an interest in the efficacy of lithium (natural isotopic abundance: 7.59 % ^6Li and 92.41 % ^7Li) for treatment of mood disorders (including major depression and biopolar disorder) despite no concrete evidence on how lithium mechanistically stabilizes mood [9]. Lithium was originally discovered as an effective treatment for mania when John Cade injected guinea-pigs with lithium urate and lithium carbonate, noting their lethargy, and then later human patients who responded positively [11]. A thought-provoking study was completed where mothering rats were given a diet including ^7Li or ^6Li and their behavior was completely opposite [12]. Mothers fed ^6Li exhibited overgrooming and overnursed, while those fed ^7Li were apathetic and nursed infrequently. A simple monovalent cation, this isotopic observed effect can not be explained by any known models. Additional lithium studies have been completed showing maternal exposure to higher levels of residential lithium in drinking water during

pregnancy was associated with a moderate increase in autism spectrum disorder and congenital malformations risk in offspring [13, 14, 15]. However, lower levels of lithium in public water supplies have also been linked to higher suicide rates [16, 17, 18] and increased rates of dementia [19, 20]. Additional complexity occurs when high levels of lithium in the public water supply have been shown to stimulate multiple types of stem cells, including ones found in the brain, blood, and bones [48, 50]. There are additional studies on the effects of lithium supplementation [21] and therapies [22], including usage of natural healing lithium mineral springs. The isotopic effect of lithium, coupled with the clear impact on brain function, led Dr. Fisher to his theory on quantum cognition and the potential existence of PCs in the brain, with which lithium may be interacting [7, 23].

While relevance of PCs to quantum computers and quantum biology is riveting, their more practical implication lies in their application to vertebrate bone. The structural integrity of vertebrate bone is primarily due to calcium phosphate matrices formed from amorphous calcium phosphate (ACP) and crystalline hydroxyapatite (HAp) [24] that mineralize on collagen fibrils. Bone material regeneration from HAp has been demonstrated, but results in weak mechanical properties and inadequate bone resorption, thus limiting bio-implantation [25]. This restricted solid-state morphological control is attributed to the presently enigmatic mineralization pathway of bone [26]. To achieve robust bone material of a specific calcium phosphate phase [27, 28, 29, ?] that is readily available, sterilizable, and cost effective [25], it is crucial to identify a metastable solution intermediate that can exchange between solution, glass, and crystalline bone phases. Foundational to identifying this key transient species was the X-ray powder diffraction study of HAp's crystal unit cell which revealed spherical 1 nm diameter clusters of molecular formula $Ca_9(PO_4)_6$ [24]. These PCs have been postulated to serve as a prenucleation cluster (PNC) mediating ACP's formation and subsequent phase transformation into HA [24].

Prior research has supported the existence of PCs [30, 24, 31, 32, 33]; however, the arrangement of atoms in a PC remained inaccessible until ab initio calculations proposed an energetically supported, S_6 symmetric structure (Fig. 1.1 inset) [30]. Features of the unrestricted PC resulting from this putative model, such as nuclear spin properties, size, chemical reactivity, aggregation rate, phase transitions, and resulting concentration, are critical to understanding the mechanistic role of PC in the bone mineralization pathway. Consequentially, these same features contribute to the nontrivial spectroscopic characterization of a PC and have thus rendered it evasive to current experimental confirmation. The objective of my PhD is to experimentally isolate a free-floating Posner cluster and confirm its structure.
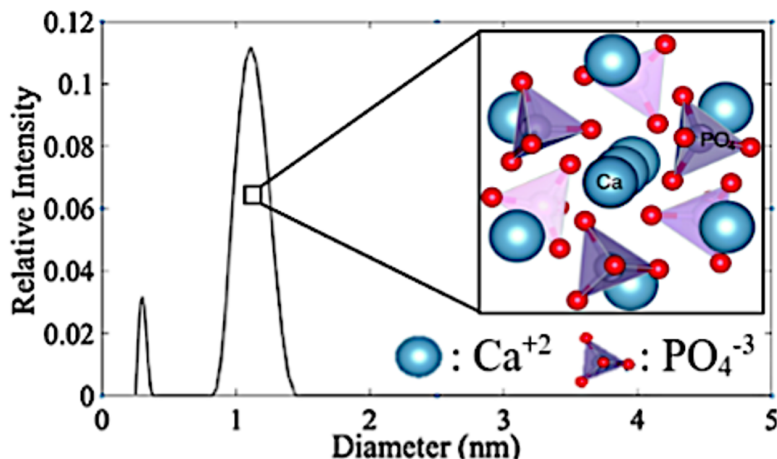
Figure 1.1: DLS of a pH 7.4 simple SBF composed of 250 mM KCl, 2 mM NaPO$_4$, and 5 mM CaCl$_2$ [34]. The 1 nm peak is implicated to contain PCs with a structure as illustrated [30]. Reproduced here with the permission of Joshua Straub.

Prior empirical evidence supports PC formation, revealing insights into their aggregate seeding, kinetics, phase transitions, and phosphate bridging modes determined by cryo-TEM, phase shift interferometry, calcium K-Edge XANES spectroscopy, and dynamic light scattering (DLS) [30, 31, 32, 33]. Still, in-depth structural characterization of the PC has not been accomplished due to inadequate experimental designs. Recent development of cross-correlating detectors (CCDs) for DLS allows for access to short time

delays, corresponding to small, rapidly diffusing particles that could not previously be accurately sized. Our team improved the DLS experiment performed on simulated body fluids (SBFs) by using a CCD DLS setup [26] and characterizing the phase diagram of calcium phosphate at 298 K [34] to ensure optimal PC conditions. To improve resolution of the PC signal, we also removed the TRIS buffer which dominates the scattering signal due to high concentration and similar size to a PC. Our reproducible working manuscript results [34] (Fig. 1.1) demonstrate a dissociated ionic species signal at 0.35 nm diameter and the formation of an approximate 1 nm diameter aggregate. The 1 nm signal persists only when both calcium and phosphate ions are present, indicating this signal is composed of a calcium phosphate cluster. In agreement with electronic structure calculations [30], this 1 nm diameter species has been assigned as the first clearly observed free-floating PC. Alternate calcium phosphate prenucleation cluster candidates include tricalcium phosphate (TCP) $[Ca_3(PO_4)_2]$, and brushite monomers $[CaHPO_4]$, of which the latter is proposed to be similar in size to a PC. There is evidence that both PCs and TCPs independently persist depending on pH regimes; the PNC is identified by the protonation state of phosphate after addition of calcium (inferred via pH monitoring), where PCs are likely to form at pH 7 and above while TCP forms at pH 6 and below [34]. While these results are promising, a more concrete way to ascertain the exact composition of a PNC under varying conditions is necessary, which can be accomplished through solid state NMR structural analysis.

To overcome PC isolation and characterization challenges, I utilized the 100 % abundant ^{31}P nuclear spins in a PC as probes to study its structure and dynamics with solution and solid-state NMR spectroscopic techniques. I investigated the ^{31}P atomic arrangement in the elusive PC with a **two-pronged approach: determination of a PC's unique (1) dynamic behavior and (2) ^{31}P spin population.** Aim (1) is focused on phosphate cluster formation and optimization under varying solution conditions, with

Aim (2) focused on utilization of the aforementioned optimal conditions to identify the structure and dynamical properties of PCs.

Aim (1) Determination of Dynamic Behavior: The focus of my research began with elucidating the phase diagram and formation mechanisms of phosphate clusters through performing NMR lineshape and relaxation experiments as a function of pH and salt concentrations. While phosphates and polyphosphates play ubiquitous roles in biology as integral structural components of cell membranes and bone, or as vehicles of energy storage via adenosine triphosphate and phosphocreatine, the solution phase space of phosphate species appears more complex than previously known. We completed routine ^{31}P solution NMR lineshape relaxation measurements on dissolved monophosphate samples as a control for calcium phosphate mechanistic studies, which resulted in discovery of an interesting phenomenon. In Chapter 2, NMR and cryogenic transmission electron microscopy (cryo-TEM) experiments that suggest phosphate species including orthophosphates, pyrophosphates and adenosine phosphates associate into dynamic assemblies in dilute solutions that are spectroscopically 'dark' will be presented. Cryo-TEM provides visual evidence of formation of spherical assemblies tens of nanometers in size, while NMR indicates that a majority population of phosphates remain as unassociated ions in exchange with spectroscopically invisible assemblies via chemical exchange saturation transfer (CEST) (See Fig. 1.2). The formation of these assemblies is reversibly and entropically driven by the partial dehydration of phosphate groups, as verified by ^{31}P Diffusion Ordered Spectroscopy (DOSY), indicating a thermodynamic state of assembly held together by multivalent interactions between the phosphates. Molecular dynamics simulations further corroborate that orthophosphates readily cluster in aqueous solution. This surprising discovery that phosphate-containing molecules, ubiquitously present in the biological milieu, can readily form dynamic assemblies under a wide range of commonly used solution conditions, highlights a hitherto unreported property of phosphate's
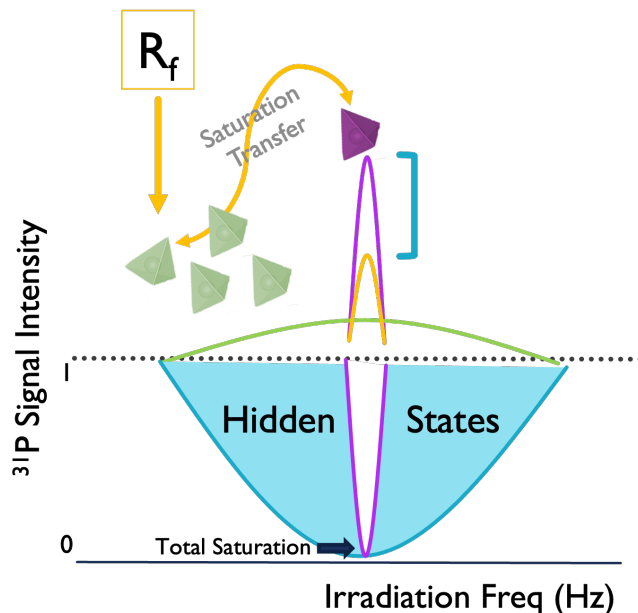
native state in biological solutions.

Figure 1.2: CEST Experiment Illustration. When irradiating radiofrequency signal (yellow arrows) adjacent to the visible 1D NMR signature (purple), if there is a hidden state (green) in exchange with the 1D signal (purple), one can detect the change in 1D signature (yellow peak) as a CEST signal (blue).

With the main goal being to stabilize and characterize calcium phosphate prenucleation clusters (purportedly a PC), we advanced to optimizing calcium phosphate solution conditions, including temperature (must be below 313 K), pH, and salt concentrations under which water soluble, nm-sized, calcium phosphate clusters are most stable and populated [34, 35]. These studies resulted in two different solution compositions, a simplified and a modified simulated body fluid which will be discussed in the next chapter.

Aim (2) Determination of textsuperscript31P Spin Population: To firmly identify structure and determine ^{31}P spin population incorporation in a PC, I analyzed the quantitative clustering of ^{31}P nuclei in monophosphate, molecular ATP, ACP, HAp (as controls), and a vitrified SBF and mSBF using solid-state NMR methods, as discussed in Chapter 3. In nonclassical nucleation theory, PNCs form, aggregate, and crystallize to

produce higher order assemblies (Fig. 1.3). Microscopy and X-Ray techniques have limited utility for PNC analysis due to small size (0.5 - 3 nm) and time stability constraints. We present a new approach for analyzing PNC formation based on ^{31}P NMR spin counting of vitrified molecular assemblies. The use of glassing agents ensures that vitrification generates amorphous aqueous samples and offers conditions to perform dynamic nuclear polarization (DNP) amplified NMR spectroscopy. We demonstrate that molecular adenosine triphosphate (ATP), along with crystalline (HAp), amorphous (ACP), and clustered calcium phosphate (mSBF) materials formed via a non-classical growth pathway can be differentiated from one another by the number of dipolar coupled ^{31}P clustered spins (Fig. 1.3).
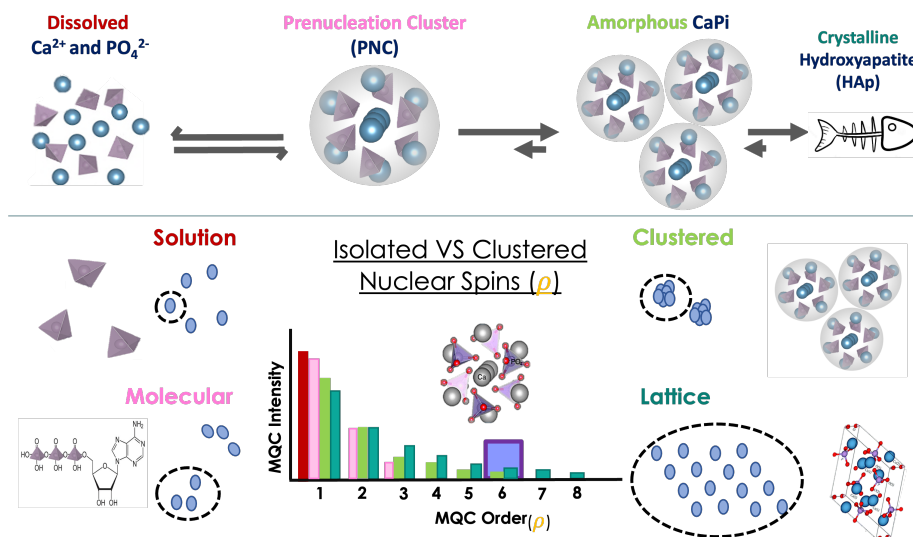
Figure 1.3: Calcium Phosphate Nucleation Pathway and Spin Counting Basics. Nucleation of calcium phosphate is seen on the top portion, with the amorphous and crystalline phases varying depending on conditions. The chemical composition of ACP has been argued as a glass phase consisting of PCs and water [36]. Spin counting of systems with varying degrees of spin organization and the resulting expected number of extracted spins (multiple quantum coherence order - MQCO p) is seen on the bottom portion. HAp structure reproduced from Zilm, et al [37]. [37].

The counting of nuclear spins is achieved through Multiple Quantum NMR experiments, as visualized in Fig. 1.4. The results presented in Chapter 3 [35] are the first

report of Multi-Quantum spin counting of assemblies formed in solution as captured under vitrified DNP conditions, which can be useful for future analysis of PNCs and other aqueous molecular clusters. This spin counting data through multiple quantum ^{31}P NMR experiments allows us to distinguish a PC from any other calcium phosphate complex through assignment of the PCs six distance dependent dipolar coupled ^{31}P nuclei based off the PCs putative structure [30]. A potential future direction would be to run atomic distance solid state NMR measurements, such as Centerband-only detection of exchange (CODEX), REDOR, or spc5 which can quantify the number of exchanging nuclei as well as the average ^{31}P-^{31}P atom bond distances through dipolar interactions, and compare with the appropriate predicted interatomic distances of a PC [30]. In addition, enriched ^{43}Ca-^{31}P distance measurements, ^{31}P lifetime measurements [38], and mitochondrial DNP are of future experimental interest.

Stabilization of a PC and subsequent capture in a vitrified state presents multiple experimental obstacles. Vitrification requires glassing agents for conventional DNP, which can, and we show, change the phase boundary of dissolved species of experimental interest depending on conditions. In Chapter 3, we additionally investigate molecular crowding pressure and solubility via glassing agent choice and alternate vitrification technique options, including the development of a rapid freeze quench apparatus. In addition, the S_6 symmetry and mobility of the six ^{31}P nuclear spins in a rapidly tumbling PC are theorized to result in a long NMR T1 relaxation time/entanglement time extending 21 days [30], thus leading to prohibitively long (up to thousands of days) required experimental time. In addition, the conversion of PCs into ACP and HAp in solution leads to a maximum calculated PC concentration of a simple SBF from DLS of approximately 10 μM ^{31}P. To combat these sensitivity issues, signal amplification via dynamic nuclear polarization enhanced NMR and addition of paramagnetic polarizing agent AMUPol to decrease T1 time will lead to increased analyte concentration.
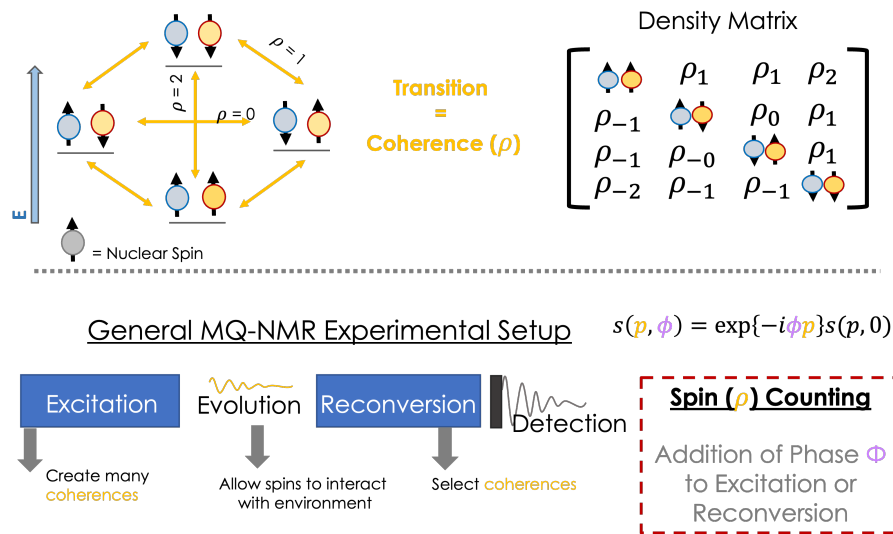
Figure 1.4: Multiple Quantum (MQ) Nuclear Magnetic Resonance Basics. Spins can be induced experimentally through selective radiofrequency irradiation to flip together at the same time and phase, which is defined as a coherence and can encoded in a density matrix shown. Zero Quantum ($p = 0$), Single Quantum ($p = 1$), and Double Quantum ($p = 2$) spin transitions are shown. MQ-NMR experimental pulse sequence setup requires an excitation, evolution, and reconversion blocks for creation, interaction, and selection of coherences, however there is no evolution period for SC experiments. The equation shown relates the incremented phase phi between successive points in the indirect NMR experimental dimension with the signal, s, which has passed through coherence order p [39].

In summary, my work is focused on elucidating the underlying mechanisms leading to the formation of various phosphate clusters. I am specifically searching for a metastable prenucleation cluster which can be structurally, magnetically, and dynamically assigned to a Posner cluster (PC) of molecular formula $Ca_9(PO_4)_6$ and size 1 nm [24, 30]. Phosphates play a ubiquitous role in biology, from structural components including cell membranes and bone to energy storage via ATP, but the solution phase space leading to the formation of phosphate clustering is not entirely understood. My work will lend insights into the role of phosphate clusters in bone's unresolved formative pathway, of which PCs have been postulated to serve as a metastable solution intermediate [24], allowing for further medical developments of bioprosthetics, synthetic scaffolding, targeted

inhibition of damaging mineralization, and selective growth promotion therapies [25, 40]. Development of improved synthetic bone could replace casts and amputation in favor of a resilient, responsive, and cheap bioceramics and/or injectable cements with improved compressive strength and solution interaction, both which can be distributed worldwide [25]. Furthermore, my research will shed additional insight onto ^{31}P nuclei quantum mechanical properties, specifically those found in PCs which are implicated to function as a platform for quantum computation in cognitive processes [7], which may lead to medical advancements in neurodegenerative diseases and brain computer interface training, design, and implementation. In addition, the magnetic structure-function relationship of PCs that I am investigating and the resulting ^{31}P nuclei long relaxation times are of fundamental interest to the chemistry and physics communities for development of MRI contrast agents and liquid state NMR molecular quantum computing [30].

Chapter 2

Phosphate Solution Conditions and Hidden States

2.1 Permissions and Attributions

1. The content of chapter 2 and appendix A has been published in PNAS [41] and submitted to NMR in Biomedicine (Lu, J., et al.). It is reproduced here with the permission of the National Academy of Sciences: `http://https://www.pnas.org/doi/10.1073/pnas.2206765120` and main author Jiaqi Lu.

2.2 Introduction

Phosphate containing species are in constant flux throughout the phosphorus cycle and accumulate within the cells of all living organisms. Cellular energy is primarily harvested through the dynamical formation and breakage of phosphoanhydride chemical bonds of adenosine phosphates [42, 43]. Free phosphates and their subsequent assembly are also involved in bone formation and growth [44, 45, 46], however the underlying

assembly mechanisms of phosphate species and other ions that lead to bone formation processes are not well understood. An understanding of the equilibrium between free phosphates and higher-order phosphate assemblies in the form of polyphosphates and phosphate clusters would provide further insight into the mechanisms involving biological energy storage and/or the engineering of biological structures.

^{31}P nuclear magnetic resonance (NMR) offers useful information about the composition, dynamics, and structural properties of lipid membrane interfaces [47, 48, 49], phosphorylated biomolecules [50, 51, 52], polyphosphates [53, 54] and precursors of bone formation [55]. We performed ^{31}P NMR to investigate the native state of phosphate species as a function of temperature with the initial intent to subsequently study the formation processes of calcium phosphate clusters. In this process, we encountered peculiar ^{31}P NMR line broadening with increasing temperature of aqueous solution of pure phosphates. Such characteristics cannot be explained by the usual temperature dependent T_2 relaxation due to increasing molecular tumbling of small molecules with increasing temperature. ^{31}P NMR line broadening as a function of pH, phosphate concentration, and counter cation species has been described in the literature [56, 57, 58], however line broadening with increasing temperature has not been reported before.

Underscoring these unexpected observations, we present experimental results showing that phosphate containing species, including orthophosphate, pyrophosphate, and adenosine diphosphate assemble into hitherto unreported spectroscopically 'dark' species, whose fractional population increases with increasing temperature. This observation is shown to be consistent with the dehydration entropy-driven formation of dynamic phosphate assemblies. ^{31}P NMR Chemical Exchange Saturation Transfer (CEST) reveals that phosphates assemble into species with broad spectroscopic signatures, whose population is in exchange with NMR-detectable phosphate species. A sub-population of these assemblies are also observed in cryogenic transmission electron microscopy (cryo-TEM)

images to exhibit droplet-like spherical assemblies up to 50 nm in diameter. The discovery that common phosphate-containing molecules can readily assemble into higher order species in water under physiological conditions in the absence of biologically activated processes should be relevant to a variety of biological and biochemical processes that use phosphate containing species as building blocks, energy sources or reactants in an aqueous environment.

2.3   Results and Discussion

2.3.1   Phosphate Species Solution NMR Properties

Unexpected NMR relaxation behavior

A series of ^{31}P NMR spectra were acquired of an aqueous solution of sodium orthophosphate at 10 mM concentration, pH 4.5 and as a function of temperature between 293 K and 343 K. Each spectrum consists of a single ^{31}P NMR line that shows significant broadening with increasing temperature, as shown in Fig. 2.1A. The full width at half maximum (FWHM) linewidth increases from 0.74 to 1.21 Hz, while the chemical shift only slightly changes from 0.14 to 0.58 ppm as referenced to 85% H_3PO_4 at 293 K. To test the consistency and generality of this observation, these measurements were repeated for solutions of orthophosphates at concentrations of 100 mM and 1 M, at varying pH from 4 to 10, at field strengths corresponding to ^{1}H NMR frequencies of 400 MHz and 500 MHz, and for solutions of orthophospates with sodium and potassium counterions, as shown in Fig. A1, A2, A3, and A4. Under every condition tested, the general trend of ^{31}P NMR line broadening with increasing temperature was observed.

To further explore this observation, we tested a series of phosphate-containing species in addition to orthophosphates, such as pyrophosphate, adenosine diphosphate (ADP)

and adenosine triphosphate (ATP). While the extent of ^{31}P NMR line broadening with increasing temperature varies between the different species and solution conditions, the general trend of line broadening with increasing temperature persists for all phosphate containing species tested here (Fig. 2.1B), suggesting that there is a common underlying molecular mechanism for solvent-exposed phosphate groups. To further our understanding, additional solvents were quickly analyzed with dissolved monophosphate, where acetic acid and pure D_2O still exhibited line broadening with increasing temperature, however DMSO and water/DMSO mixtures had the reverse trend. We took this even further and investigated dimethyl methylphosphonate, an organophosphorus compound closely resembling phosphate in structure, and found this line broadening trend to persist as well. We could not trivially investigate RNA or DNA due to the inherent nature of spontaneous double strand formation in water.

This line broadening is surprising, as it is inconsistent with expected trends for small molecules, including ionic species. Increasing temperature should generally lead to motional narrowing of NMR resonances of small molecules as their tumbling rate increases. An exception to this trend would be a case where increasing chemical exchange rate leads to a transition from an intermediate to a faster exchange regime, where the chemical shifts of the two species significantly diverge, given that the line width is proportional to the square of the chemical shift difference. In such a case, however, one would normally observe the splitting of the broad line into additional narrow resonances at sufficiently high temperatures, which was not observed for any of the phosphate-containing species studied under a wide range of experimental conditions. An additional possibility is scalar relaxation of the second kind, which has been observed to lead to line broadening with increasing temperature [59]. However, for such a case the proton exchange rate should be of the same order of magnitude as the linewidth, i.e. on the order of a few Hz, which is not the case for our phosphate solutions, given that the second order rate constant for

proton exchange between monobasic and dibasic phosphate is $1.45 * 10^9$ mole^{-1} l sec. $^{-1}$, orders of magnitudes larger than Hz [60].
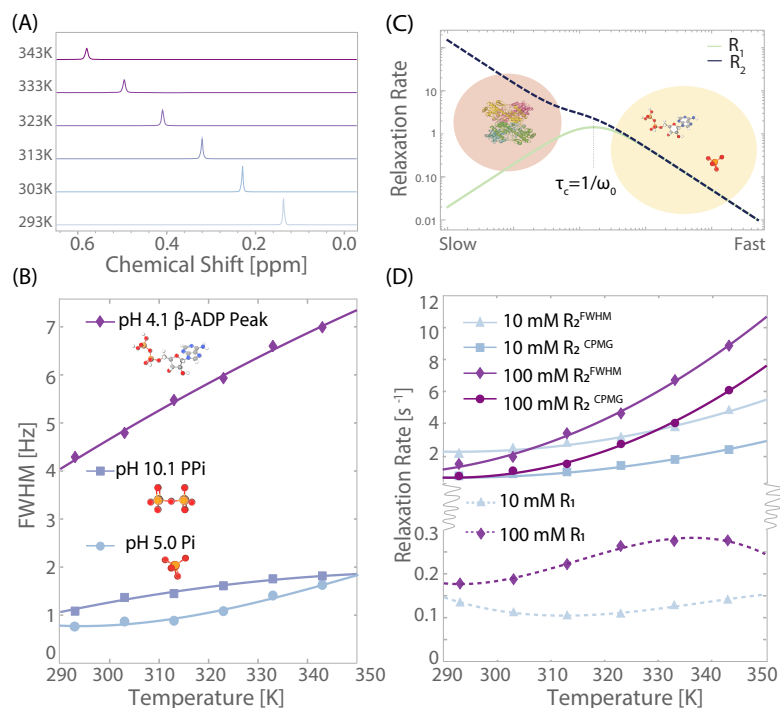

Figure 2.1: ^{31}P NMR results for phosphate-containing species. (A) 1D NMR spectra from 10 mM sample in (D) taken at every 10 K showing line broadening in orthophosphate. (B) Linewidths for orthophosphate, pyrophosphate, ADP, and ATP as a function of temperature showing monotonic increase with temperature. Solid lines are quadratic fits to data to guide the eye. (C) R_1 and R_2 curves as a function of molecular tumbling rate from Bloembergen-Purcell-Pound theory. Cartoons illustrate the approximate locations of ionic phosphate, ADP, and a standard protein based on tumbling rates. (D) R_2 as extracted from a CPMG pulse sequence and from FWHM for 10 mM and 100 mM monobasic sodium orthophosphate pH 4.5 as a function of temperature, showing monotonic increase in R_2 in each case. Solid lines are quadratic fits to data to guide the eye. R_1 for 10 mM, 100 mM, monobasic sodium orthophosphate pH 4.5 as a function of temperature showing different curve shapes as a function of concentration. Solid lines are cubic fits to data to guide the eye.

To further examine the nature of the underlying process leading to the observed line broadening and its temperature-dependence, we measured the ^{31}P NMR spin-spin relaxation rate, R_2, at varying temperatures from 293 K to 343 K. This allowed us to assess whether the ^{31}P NMR line broadening with increasing temperature originates from

inhomogeneous broadening due to the presence of multiple distinct spectral components or lifetime broadening. The value for R_2 in Hz measured by the Carr-Purcell-Meibom-Gill (CPMG) [61, 62] sequence was compared to that extracted from the FWHM (following $R_2 = \pi \cdot$ FWHM) for a 10 mM and 100 mM solution of sodium orthophosphate, as shown in Fig. 2.1D. We found that the two showed comparable trends for broadening, with slightly higher (1-2 Hz) values for the FWHM-derived linewidth compared to that directly measured via R_2, likely due to field inhomogeneities and small temperature gradients. This observation verified that the phosphate linewidth is primarily broadened by the dynamical properties of a homogeneous spectral population. This correspondence was found consistently across all samples tested. The expected trend from Bloembergen-Purcell-Pound (BPP) theory [63] of decreasing R_2 with increasing molecular tumbling rate, i.e. temperature, is shown in Fig. 2.1C to contrast to the experimental trend shown in Fig. 2.1D.

The temperature-dependence of the spin-lattice relaxation rate, R_1, provides further information on the molecular-scale dynamical properties of these phosphate solutions. We measured R_1 for a serious of phosphate concentrations, and again, observed unexpected values and trends. As illustrated in Fig. 2.1C, small molecular species tumble in the 'fast' regime- where rotational correlation time is faster than the Larmor frequency- and so R_1 is expected to monotonically decrease with increasing temperature, and to be nearly identical with the R_2 values. Instead, we observe R_1 values for orthophosphates at concentrations from 10 mM to 100 mM that are as many as one to two orders of magnitude smaller than the R_2 values of the same samples. This observation suggests that the monitored phosphate species experience much slower dynamics than those of isolated orthophosphate monomers. Assuming a random field relaxation mechanism, the molecular tumbling correlation time would have to be larger than 10 ns, corresponding to a hydrodynamic diameter of larger than 4.4 nm according to the Stokes-Einstein relation

in order to result in the observed difference between R_1 and R_2.

This consideration leads to the question of whether the states of phosphates giving rise to the observed properties correspond to phosphate assemblies. When examining the shape of change in R_1 with increasing temperature, we observed a subtle deviation from BPP theory for the solution of sodium orthophosphates at 10 mM concentration (Fig. 2.1D). The initial decrease of R_1 with temperature is expected, but not the observed increase at temperatures above 310 K. This latter observation is again consistent with a temperature-induced formation of larger phosphate assemblies, as such assemblies would lead to a lower rotational correlation time, effectively moving in the direction of the "slower" motion regime (towards the left of the x axis) as illustrated in Fig. 2.1C. A similar trend is observed for 10 mM potassium orthophosphate samples (see Fig. A1).

The temperature dependence of R_1 for sodium orthophosphates at higher concentrations (100 mM) showed a local maximum with increasing temperature (Fig. 2.1D).This trend is again inconsistent with the dynamical properties of small molecules in solution. According to BPP theory, a local maximum in R_1 is expected only for species with rotational correlation times, τ_c, matching the inverse nuclear Larmor frequency, ω_0 (Fig. 2.1C). At 11.7 Tesla and a ^{31}P NMR frequency of $\frac{\omega_0}{2\pi} = 200$ MHz, assuming a random field relaxation mechanism, we estimate $\tau_c = 800$ ps following $\tau_c = \frac{1}{\omega_0}$. A rotational correlation time in this range implies a particle diameter of 2 nm for a spherical object according to the Stokes-Einstein relation. Regardless of the exact shape of the species, this size is several fold larger than that of monomeric orthophosphates [64].

The observed temperature-dependent trends in R_1 and R_2 are consistent with (a) the phosphate molecules assembling into larger species, whose tumbling rate lies in the slow motion regime, with correlation time τ_c exceeding ω_0, or (b) phosphate molecules being in exchange with spectroscopically invisible species that have much higher R_1 and R_2 rates. Explanation (b) would again be consistent with phosphate assemblies, since there

are no other constituents than phosphate ions in the solution. Higher temperatures may facilitate the growth in population and size of such assemblies and/or accelerate the exchange, and hence enhance R_1 and R_2 of the detected ^{31}P NMR signal. It is also possible that monomeric phosphates coexist with spectroscopically invisible phosphate clusters across the temperature range tested, and that heating increases the relative abundance of this invisible species. Either scenario suggests the formation of larger phosphate assemblies, with enhanced populations and/or exchange rates at elevated temperatures, yielding much greater R_2 values compared to R_1 and consistent with our observed trends in relaxation with temperature. Notably, after cooling the sample that was heated back down to its initial temperature, the relaxation rates return to their initial values (Fig. A5), suggesting that the assembly formation is reversible.

If larger assemblies are forming, it is important to consider their nature, and in particular the interactions leading to their formation. One possibility is that the new assemblies are polyphosphates formed by the enhanced formation of P-O-P bonds at elevated temperatures. The ^{31}P chemical shift for phosphates is known to shift by approximately -10 ppm with each P-O-P bond formed and by a maximum of 5 ppm from the unprotonated to triply protonated states [65, 66]. This is inconsistent with our observed chemical shifts that move systematically downfield, but only very slightly, by a maximum of 0.5 ppm when the temperature is increased from 293 K to 343 K. Hence, the observed chemical shift change is too small to be attributed to covalent P-O-P bond formation. The observed 0.5 ppm chemical shift change could instead be the result of changes in the equilibrium P-O bond length, potentially induced by non-covalent association of phosphate molecules. Such changes could be mediated by hydrogen bond interactions that, in turn, can be modulated by changes in phosphate hydration. Notably, all four oxygens of the phosphate group can serve as hydrogen bond donors or acceptors, depending on the protonation, hydration and partial charge state of the group, hence allowing for mul-

tivalent interactions that can give rise to the formation of larger assemblies, while still maintaining rapid exchange with ionic phosphates and small clusters held together by weak interactions. In any case, the species forming must either have the same chemical shift as the orthophosphate ions and/or be so broad as to be rendered spectroscopically invisible.

2.3.2   Hidden Solution Phosphate Aggregate Species Discovery

Indirect observation of phosphate assemblies by ^{31}P CEST

To test whether the phosphate species are in exchange with a spectroscopically dark population, we performed chemical exchange saturation transfer (CEST) experiments. CEST typically provides a means of identifying signatures of exchangeable species with distinct chemical shifts from the visible species, but below the direct NMR detection limit. This effect is achieved by saturating a selected region in the spectroscopically invisible region of the spectrum, followed by the detection of the (visible) signal of a major species (in this case, monomeric phosphates) that is in exchange with the species below the NMR detection limit. Repeating these experiments with different saturation frequencies across the complete spectral region and saturation power permits scanning of an entire spectrum for potentially exchanging species. This procedure has been widely employed, for example, to identify weakly populated states of peptides and proteins whose protons are in exchange with water[67, 68], and in this context is often referred to as DEST (for dark state exchange saturation transfer)[69]. The sensitivity enhancement effect for the dark species is achieved because exchange can occur many times during the saturation pulse, and thereby transfer saturation levels between the visible and invisible species repeatedly. In the CEST experiment of this study, we recorded ^{31}P NMR spectra of the visible ^{31}P NMR signals following rf irradiation (with nutation frequency of 150

Hz for 5 s) at a specified resonance frequency in what can be seen as a one-dimensional pump-probe experiment. Here, the pump frequency is stepped through a frequency range of approximately 8000 Hz, centered around the one visible ^{31}P NMR peak. In this fashion, CEST can test for the existence of spectroscopic dark states that are in exchange with phosphate species at frequencies within the scanned range. A plot of the detected intensity vs. saturation frequency offset is called a Z-spectrum.
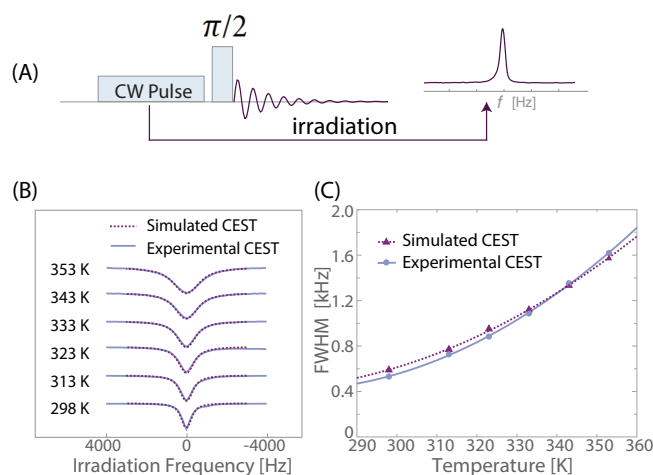

Figure 2.2: ^{31}P CEST results for 100 mM orthophosphate (pH=4.5). (*A*) CEST pulse sequence. (*B*) The experimental and simulated CEST Z-spectra as a function of temperature with 150Hz of the irradiation pulse power. (*C*) The width at half height of both the experimental and simulated Z-spectrum dips from (B) as a function of temperature. The solid and dashed line represent a quadratic fit to data as a guide for the eye.

Fig. 2.2*B,C* shows the both the measured (solid lines) and the simulated (dashed lines) Z-spectra as a function of temperature of a 100 mM orthophosphate solution. It is seen clearly that the widths of the dips in the Z-spectra increase with increasing temperature, which is consistent with the unexpected trend observed with the R_2 and linewidth data.

In the absence of exchange, one expects the width of the dip in the Z-spectrum (at half maximum) to be approximately a factor two times the rf nutation frequency (here 150 Hz) [70]. In all cases for CEST measurements (both as a function of temperature

and as a function of irradiation power), we observed the dip widths to be significantly larger (a factor of 3-10 larger than the nutation frequency) than the expected two-fold the nutation frequency (see Fig. A10). This finding is a clear sign that there must be significant underlying exchange processes with spectroscopically silent species, and that these processes change with temperature.

These results further corroborate the assumption that exchange occurs with a population exhibiting a broad spectroscopic signature, which is invisible to direct spectroscopic detection. The relative population of this spectroscopically 'dark' species may also be increasing with increased temperature. When the solutions are cooled back down to 298 K after heating, the Z-spectrum dip width returns to the originally measured value (Fig. A6), indicating reversible assembly formation. Similar CEST results were observed for a range of pH values of orthophosphate solutions (Fig. A7) and for ADP (Fig. A8), suggesting that this behavior is common among several phosphate-containing molecular species in aqueous solution.

In order to further substantiate the hypothesis and generate a potential model, simulations were performed that could simultaneously satisfy the values and temperature trends of R_2 and CEST data. For the simulation, a two-pool model was used, with A referring to the detectable pool (phosphate monomers) and B to the spectroscopically silent pool (the assemblies). The model used separate R_1 and R_2 for pools A and B, exchange rate constants for the forward and backward interconversion processes $A \longleftrightarrow B$, and the relative populations of the pools, considering first-order kinetics. The rate constants were assumed to be of Arrhenius type, and the forward rate constant was parameterized using an Arrhenius pre-factor k_0 and activation energy E_a. The change of enthalpy ΔH_{PA} and change of entropy ΔS_{PA} for assembly formation derived from this simulation (shown in Appendix A) were then used to find the assembly population, p_B, using the Boltzmann factor $p_B = \exp(-\Delta G_{PA}/(RT))/(1 + \exp(-\Delta G_{PA}/(RT)))$, where

$\Delta G_{PA} = \Delta H_{PA} - T\Delta S_{PA}$. The temperature dependence entered through the $T\Delta S_{PA}$ term, while ΔH_{PA} and ΔS_{PA} were assumed constant. At each temperature, these relationships were used to calculate the forward and backward exchange rates, and the McConnell equations solved iteratively to satisfy the experimental R_2 and CEST data using the Spinach software package [71].

Simulations of the R_2 data as a function of temperature of the 100 mM NaH_2PO_4 sample (at pH=4) led to the following parameters to describe the exchange process: $\Delta H_{PA} = 25$ kJ/mol, $\Delta S_{PA} = 30$ J/(mol K), $k_0 = 20,000$ s^{-1}, and $E_a = 10$ kJ/mol. We then calculated the relative fraction for the B population, p_B, as described earlier. The forward and backward exchange rates are obtained via $k_f = k_0 \exp(E_a/RT)$, and $k_b = k_f(1-p_B)/p_B$, in steady state. For CEST simulations, R_1 was set equal to the measured values (shown in Fig. 2.1) for both pools (after verifying that setting $R_1^B = 0.1R_1^A$ to $10R_1^A$ did not change the quality and results of the fit), and R_2^A set equal to R_1^A, assuming a fast motion regime for the small molecular entity. Modeling of the R_2 data indicated that $k_f \gg p_B\Delta R_2$ is likely, where $\Delta R_2 = R_2^B - R_2^A$. In this regime, $R_2 \approx p_B\Delta R_2$ [72]. We therefore used this expression to determine the R_2^B values for the CEST simulation by using the fitted p_B values, the experimental R_2 values and relying on $R_1^A = R_2^A$, i.e. by equating R_2^A to the experimental R_1 values. These values ranged from 450 to $1,000$ s^{-1} over the experimental temperature range (increasing with increasing temperature), corresponding to linewidths exceeding 1400 Hz that hence is easily beyond the detection limit.

Using this approach, a consistent model was found to fit concurrently the experimental R_2 and CEST data (see Fig. 2.2 and Fig. A10). The key takeaway is that increasing temperature leads to either larger or less mobile assemblies, as reflected in increasing R_2^B with temperature (see Fig. A11), an increase in both k_f with increasing temperature (see A10A), with the rates spanning 350-660 Hz. Most critically, the model that describes the
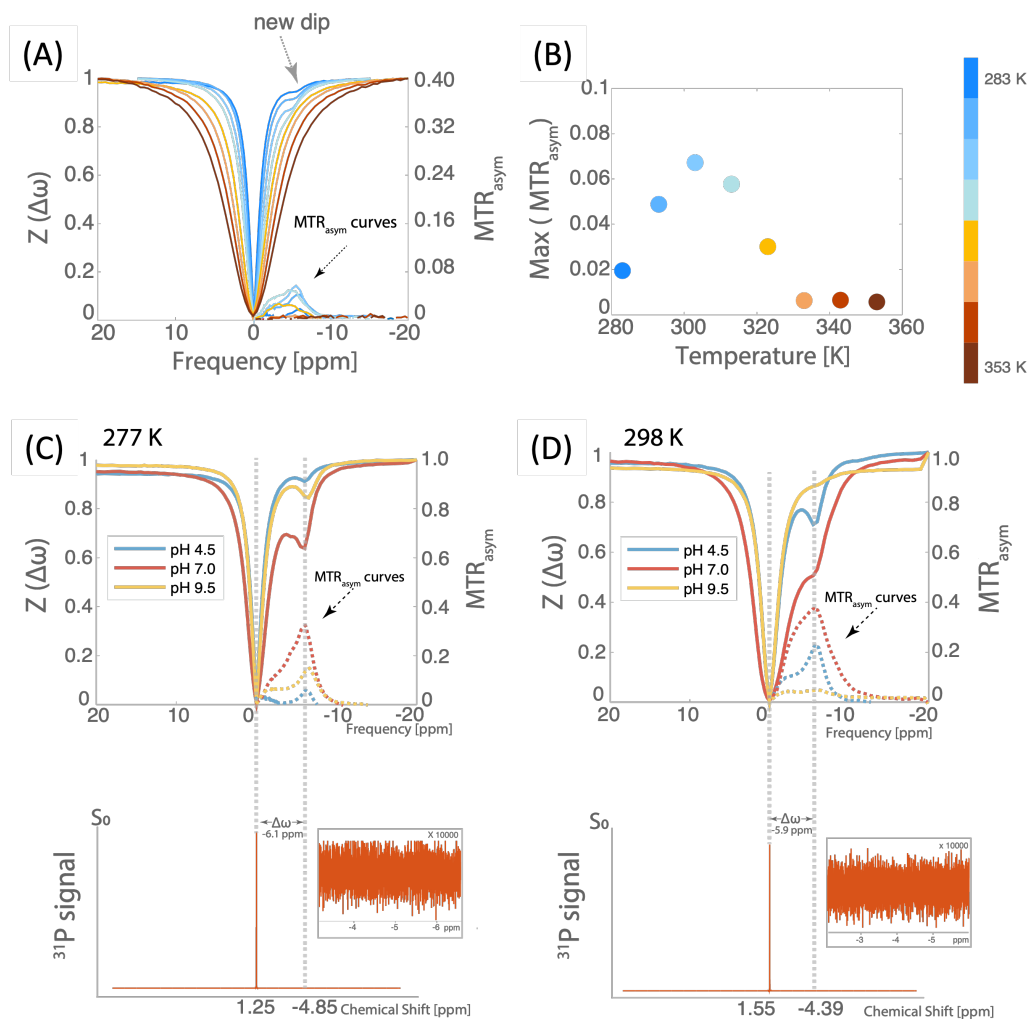
Figure 2.3: ^{31}P CEST results for 100 mM sodium orthophosphate. (A) Temperature dependence in 10% D_2O (pH 4.5) from 283 K to 353 K in increments of 10 K. (B) The maximum value of MTR_{asym} of the series shown in (A) at each corresponding temperature. (C) CEST Z-spectra and MTR_{asym} curves pH dependence (top) and ^{31}P 1D NMR spectrum (bottom) in pure D_2O (pH 4.5, 7.0 and 9.5) at 298 K. (D) CEST Z-spectra and MTR_{asym} curves pH dependence (top) and ^{31}P 1D NMR spectrum (bottom) in pure D_2O (pH 4.5, 7.0 and 9.5) at 277 K. Reproduced here with the permission of Jiaqi Lu.

R_2 and CEST data finds the fractional population of the assemblies, p_B, to be very small, but to grow with temperature (A10C), with $p_B = 0.0013$ of phosphates at 293 K and 0.0073 at 353 K. While the absolute value of p_B in a dilute solution of monophosphates is small, the size of the assembly (the B pool) may comprise of a very large number

25

of monomers (the A species), as reflected in the extremely high R_2^B rates. Assemblies formation, even with a small p_B, can have a significant impact on biological assemblies between phosphate-containing species in closer proximity.

[31]P CEST irradiation regime expansion and exploration of lower temperatures revealed the appearance of a distinct hidden pool of phosphate aggregates exchanging with monomeric phosphates for 100 mM sodium phosphate as shown in Fig. 2.3. The CEST effect is usually analyzed using the magnetic transfer ratio asymmetry (MTR_{asym}) metric obtained from Z-spectra (CEST spectra) plotted as a function of RF irradiation frequency [73, 74]. These pronounced dips several ppm upfield of the main phosphate resonance at low temperatures are undetectable with direct ^{31}P NMR spectroscopy. This effect becomes relatively weak at higher temperatures and more pronounced at pH 7 and in pure D_2O. At the lowest temperatures (283 K, 293 K, and 303 K), a clear extra dip is observed in the Z-spectra approximately 5 ppm upfield of the main ^{31}P resonance. We note that the chemical shift of the maximum intensities of MTR_{asym} are at -5.5 ppm in the temperature range of 283 K to 313 K, however the chemical shift shifts further downfield as temperature increases beyond 313 K. This phenomenon could be attributed to alterations in the fractional population and/or the exchange rate between the monomeric phosphate groups and the phosphate clusters. This phenomenon was likewise observed in biologically significant triphosphate solution samples at 277 K under comparable experimental conditions. Polyphosphate exhibited similar phemonema as well, however there was 1D direct phosphorous signal within the chemical shift range of the CEST observed peak, complicating interpretation.

Cryo-TEM

While there is compelling evidence for assembly formation, the previous measurements did not provide direct observation of the assemblies due to their spectroscopically

dark nature. We hence used cryogenic transmission electron microscopy (cryo-TEM) to determine whether the phosphates assemble into large and persistent enough clusters to be imaged. Cryo-TEM was performed on ADP solutions that were vitrified after heating for at least 48 hours. Phosphate-containing solutions tested showed evidence of assemblies forming at diameters ranging from 30-50 nm in diameter (Fig. 2.4A,B, Fig. A12). This is in contrast to a 500 mM KCl control solution, where a majority of features were at diameters of 50 nm and greater, consistent with consensus within previous cryo-TEM literature establishing that the most abundant form of ice artifacts are at sizes greater than 50 nm [75, 76]. Given that these samples were prepared under identical conditions, we take this difference in the 30-50 nm region of the particle size distributions between the phosphate-containing solutions and the KCl control to indicate the presence of phosphate assemblies. Amongst the conditions tested, the abundance of assemblies appeared higher in solutions heated at 343 K compared to solutions that are unheated or salt controls without phosphate present (Fig. A13). Additionally, ADP samples from different sources, and prepared on different days, showed an abundance of these features (Fig. 2.4A,B and A12). Such analysis of cryo-TEM micrographs cannot provide quantitative analysis of the whole sample, given the nature of the thin film of water that forms before vitrification that can affect which particles may be imaged. Still, this methodology provides evidence that these features are not artifacts of sample preparation. We also found that for samples of 100 mM and 1 M sodium monophosphate the size distribution of structures is independent of phosphate concentration (Fig. A14), providing additional evidence that these are equilibrium structures. Notably, the entire phosphate-containing population is part of or is in exchange with the assemblies, given the homogeneously broadened nature of the ^{31}P NMR line. This suggests that the monomeric ADP and monophosphate populations are at thermodynamic equilibrium with the assemblies that may exist as liquid droplets, given their spherical shape. The phosphate assembly may

27

be driven by liquid-liquid phase separation. However, further validating such hypothesis

is outside the scope of this study, given that the assemblies evade quantitative analysis.
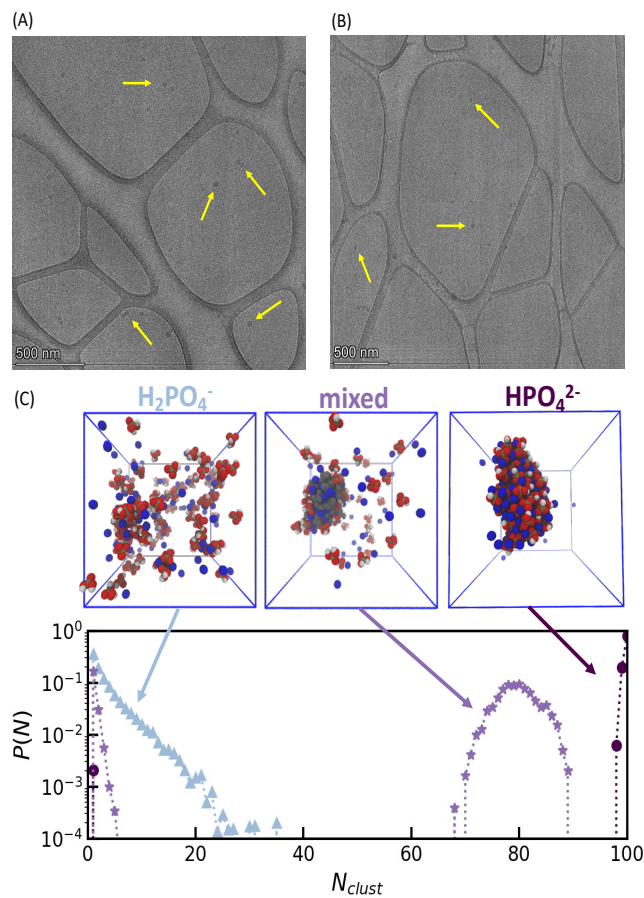

Figure 2.4: Evidence of phosphate assemblies from TEM and MD simulations. (A, B) TEM images of phosphate assemblies (yellow arrows) after heating phosphate solutions show droplet-like features forming at 25-50 nm in size. Samples were from different sources and prepared on different days. (A) 100 mM potassium ADP heated to 343 K before vitrification. (B) 100 mM sodium ADP heated to 343 K before vitrification. (C) Cluster size distributions from MD simulations at 343 K show the fraction, $P(N)$, of phosphate ions in a cluster of size N_{clust}. The insets show snapshots of phosphate assemblies (red and white) and sodium ions (blue) from the simulations. The cluster size distribution and snapshots show that HPO_4^{2-} strongly assembles in contrast to $H_2PO_4^-$. When $H_2PO_4^-$ is mixed with HPO_4^{2-}, the latter induces clustering of $H_2PO_4^-$. In this mixed system, the HPO_4^{2-} ions are grayed out to highlight the clustering of $H_2PO_4^-$. Simulation snapshots are visualized using Visual Molecular Dynamics.[77]

28

Molecular Dynamics Simulations

We next used molecular dynamics (MD) simulations to probe whether monomeric phosphate species can form stable clusters under the relevant aqueous solution conditions. We simulated three different solutions of orthophosphates: HPO_4^{2-}, $H_2PO_4^-$, and a 1:1 mixture of HPO_4^{2-} and $H_2PO_4^-$ using a modified GAFF forcefield [78] and TIP3P water [79]. The simulated systems each contain 100 total orthophosphates, enough Na^+ ions to neutralize them (200, 100, and 150, respectively), and water molecules to solvate to approximately 1 M orthophosphate concentration (4759, 4852, 4801 water molecules, respectively). We also simulated two less concentrated systems ($\sim$78 mM), comprising (1) 3 HPO_4^{2-} ions, 6 Na^+ ions, and 2149 water molecules and (2) 3 $H_2PO_4^-$ ions, 3 Na^+ ions, and 2149 water molecules to more carefully probe the temperature-dependent water-phosphate, phosphate-phosphate, and counterion-phosphate interactions. Additional details regarding the systems and simulation workflow are provided in the Appendix A (Table S1). At 343 K, the HPO_4^{2-} system shows a strong tendency to assemble, forming a cluster comprising all 100 phosphate ions in the simulation box. The cluster size distribution for the HPO_4^{2-} system, represented as the fraction, $P(N)$, of phosphate ions in clusters of size N_{clust}, is therefore peaked at the maximum number of HPO_4^{2-} ions of 100 (Fig. 2.4C). We hypothesize that the equilibrium cluster size is larger than accessible by atomistic MD. This result is consistent with the observation of large phosphate assemblies visible to cryo-TEM, giving rise to distinct NMR spectral and relaxation properties. Interestingly, the $H_2PO_4^-$ system shows a much weaker tendency to assemble, with a peak in the cluster size distribution at $N_{clust} = 1$, indicating a preference to remain unaggregated at these conditions. However, in the mixed system, the presence of HPO_4^{2-} induces assembly of $H_2PO_4^-$ ions, and the system forms an assembly that comprises all 50 HPO_4^{2-} in the simulation box and some $H_2PO_4^-$ (Fig. A16 B-D). The three systems exhibit qual-

itatively the same behavior at 293 K (Fig. A16A). The simulations are limited to system sizes smaller than the experimentally observed assemblies, as well as constant ionization state (as opposed to constant pH), which limits our ability to draw conclusions regarding the temperature dependence and size distributions of the observed clustering behavior. However, the MD simulations do confirm that orthophosphates cluster under comparable conditions as experimentally probed.

In addition, the sodium ions were observed to be involved in the phosphate assemblies by the MD simulations, and therefore the linewidth of sodium in the presence and absence of phosphate was investigated. While the ^{23}Na NMR line was found to narrow with increasing temperature, the ^{23}Na linewidth was broader for samples of NaCl with phosphate present as compared to NaCl without phosphates at both 298 K and 343 K (Fig. A17). This observed increase in linewidth for ^{23}Na when phosphate is added to solution is consistent with the sodium ions also being incorporated into the phosphate assemblies. Although the ^{23}Na still narrows with temperature, this can be explained by the mechanisms that traditionally lead to line narrowing at higher temperature (such as larger fluctuations in electric field gradients and increased molecular tumbling rates) overcoming effects of a larger population of sodium ions being incorporated into assemblies. Since the relaxation mechanisms of the sodium, in monomer or assembled state, are quite different from the mechanisms for phosphates [80], the overall effect of increased temperature on ^{23}Na NMR could still be line narrowing, but with different magnitudes of linewidths depending on whether phosphates are present to form assemblies.

DOSY NMR

Having established that larger phosphate assemblies exist in solution, we next explore the potential mechanisms of their assembly and, in particular, the temperature-dependent behavior. We performed pulsed field gradient (PFG) NMR, specifically Diffusion Ordered

Spectroscopy (DOSY), to measure the self diffusion coefficients of the ^{31}P NMR signal-bearing species, and hence their hydrodynamic diameter. DOSY measurements were performed on a 100 mM sodium orthophosphate solution of pH 4.5 at 293 K, 343 K, and again at 293 K after cooling in order to assess the reversible formation of any structures at elevated temperatures. The results show that the phosphate species in solution diffuse with a single translational diffusion coefficient, as demonstrated by the linear relationship between Log(ψ) and the square of the gradient strength, where ψ is the signal attenuated by molecular motion along the gradient axis (Fig. 2.5A) [81]. This observation of a uniform diffusion coefficient did not change with increasing temperature. However, the diffusion coefficient significantly increased from $7.5 * 10^{-10}$ m^2/s at 293 K to $3.2 * 10^{-9}$ m^2/s at 343 K. We confirmed that this increase is not due to convection effects by comparing diffusion values measured with a convection-compensated pulse sequence (Fig. A18), as well as in the presence and absence of capillaries added to the sample tube to disrupt convective flow (Fig. A19) [82]. To convert these diffusion coefficients to hydrodynamic diameters, we used the Stokes-Einstein relationship to account for the increased thermal energy and the decreased viscosity of water at elevated temperature. The extracted (temperature-corrected) hydrodynamic diameters for orthophosphate ions show a reversible and significant decrease by 1.8 Å at 343 K compared to 293 K (Fig. 2.5B), suggesting partial dehydration of hydrated orthophosphate ions in water. Similar increases in the diffusion coefficient and decreases in the hydrodynamic diameter were observed for monophosphate ions in 100 mM and 1 M potassium phosphate samples and 1 M sodium phosphate samples (Fig. A20 and A21).

How do we reconcile the observation of assembly of orthophosphates according to ^{31}P NMR relaxation and CEST studies with the apparent decrease in the hydrodynamic radius of orthophosphate molecules, implying the partial dehydration of the detected phosphate ions at elevated temperatures? Presumably, the partially dehydrated phos-

phate groups can more strongly interact with other phosphate groups through stronger hydrogen bond formation. Hence, they may more readily assemble into, and exchange with, dynamic phosphate clusters. It is known that a single deprotonated orthophosphate moiety, the $H_2PO_4^-$ ion, carries 11 water molecules within its hydration shell at infinite dilution (the HPO_4^{-2} ion carries 20 water molecules) [83]. The ^{31}P DOSY result for samples of pH 4.2, where the large majority of the population is in the $H_2PO_4^-$ protonation state, suggests a decrease in the hydrodynamic diameter from 6 Å to 4.2 Å. This change in hydrodynamic radius is consistent with a decrease in hydrodynamic volume by 70 Å^3. Assuming a water radius of 1.4 Å[84], this result suggests a loss of 6 hydration water molecules upon heating, yielding a total of 5 remaining hydration water molecules per orthophosphate at 343 K. Given that the temperature dependent characteristics of ^{31}P NMR linewidth and relaxation data were observed across a wide pH range from 2 to 11, we expect both $H_2PO_4^-$ and HPO_4^{-2} ions to experience loss of hydration water with increasing temperature.

To further validate this experimental analysis based on DOSY, we performed MD simulations of less concentrated HPO_4^{2-} and $H_2PO_4^-$ systems discussed earlier. MD calculations show a decrease of water coordination from 13.4 to 13.1 per HPO_4^{2-} molecule and from 16.5 to 15.7 per $H_2PO_4^-$ with increasing temperature from 293 K to 343 K (Fig. A15C), corresponding to the range of temperatures experimentally probed. These results are qualitatively consistent with the trends observed experimentally. Although this average change is relatively small, it is being driven by very large changes in hydration for the phosphates forming assemblies. Additionally, the decrease in the hydration number of orthophosphates is less dramatic in the MD simulations, as the computational analysis does not probe hydrodynamic radii, but rather local density.

Is DOSY then detecting the phosphates within clusters directly? As discussed, phosphorus spins in these clusters undergo rapid relaxation due to their slower tumbling rates,

and thus have very broad resonance lines, largely invisible to ^{31}P NMR. Thus, DOSY measurements should only be sensitive to the free phosphate ions that exist in equilibrium with these larger, spectroscopically dark, assemblies. The DOSY results reveal that free phosphate ions exchanging with the phosphate assemblies are more dehydrated at elevated temperatures, and hence potentially have a greater tendency to assemble into larger clusters.

Examining entropy-driven assembly

What then is the driving force for the formation of soluble, non-covalent, phosphate assemblies at equilibrium that are reversibly promoted at elevated temperature? Considering the Gibbs free energy for assembly, ΔG_{PA}, an increasing tendency to assemble ($\Delta\Delta G_{PA} < 0$) at higher temperature requires that ΔS_{PA} for assembly be positive, so that the entropic contribution lowers the free energy of assembly as temperature is increased, since generally ΔH increases (i.e. is less favorable) with increasing temperature [85]. The thermodynamic parameters found in fitting our experimental R_2 and CEST data of a $\Delta H_{PA} = 25 kJ/mol$ and $\Delta S_{PA} = 30$ J/(mol K) is consistent with an entropy-driven assembly. However, considering the fit value of $\Delta H_{PA} = 25 kJ/mol$ and a 0.6 % population growth from 20 to 70 °C for a NaH$_2$PO$_4$ sample, the largest ΔH extracted would amount to only 0.002 J//g solution for assembly formation of a 1 M potassium orthophosphate sample, rendering direct experimental verification of these thermodynamic values on our DSC instrument unfeasible. Nonetheless, an extensive set of experimental data provided strong evidence for a favorable phosphate assembly with increasing temperature, implying that the phosphate assembly is enhanced by entropy gain with increasing temperature.

Possible sources for this putative entropy gain are depletion interactions, including excluded volume effects, counterion release, and/or dehydration of the phosphate

moiety[86]. Excluded volume interactions between phosphates would not be expected to reduce the hydrodynamic diameters of individual phosphate monomers, and species with overlapping volume would co-diffuse, resulting in slower diffusion, neither of which effects are observed by DOSY. Another commonly expected source of entropy gain upon assembly of charged species is the release of bound counterions, however potassium and sodium ions are not strongly bound to phosphate, making its release a less likely source for significant entropy increase. This assessment is consistent with our MD simulation results, which show that there is no significant change in the number of counterions coordinated with HPO_4^{-2} and a slight increase in the counterion coordination number for $H_2PO_4^-$ in the less concentrated ($\sim$78 mM) systems (Fig. A15I). This analysis further supports our expectation that the phosphate-cation interaction is weak, making counterion release an unlikely driver of phosphate assembly. Furthermore, the observed changes in the hydrodynamic diameter of orthophosphates with increasing temperature as measured by DOSY are very similar between potassium and sodium phosphate samples (Fig. 2.5A and Fig. A21). Since sodium and potassium ions are approximately 1 Å different in size [87], a difference in the change of the hydrodynamic diameter is expected if counterion release was a major contributor to these observed size changes of orthophosphates.

Hence, the most likely source of increase in the total entropy is the shedding of water that is more strongly associated with the phosphate ions than with bulk water, also referred to as the hydration shell. Water forms networked hydrogen bonds and strongly solvates phosphate anions, offering ample opportunities for entropy increase upon its partial release. DOSY experiments and MD simulations confirm that water molecules are released to bulk when increasing the temperature from 293 to 343 K. In a recent study, dehydration-driven entropy increase has been shown to be a primary driver of liquid-liquid phase separation induced by polyelectrolyte assembly processes in water [88].
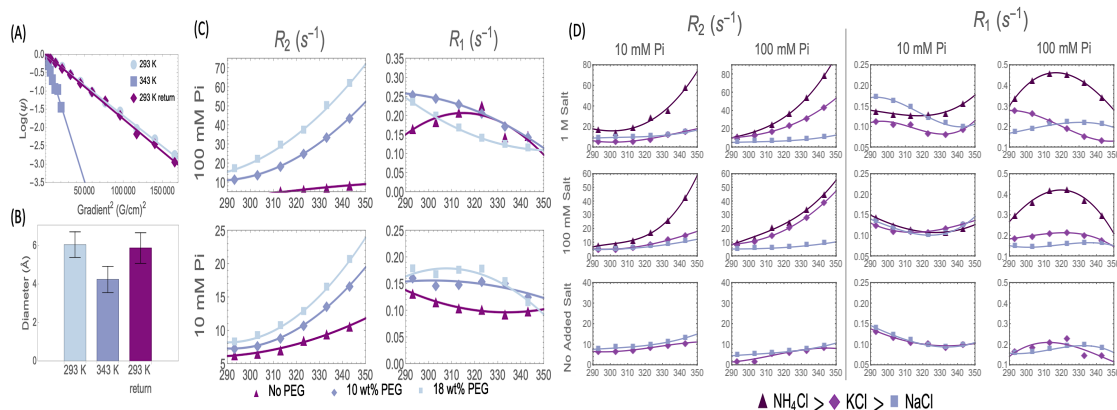
Figure 2.5: Evidence of entropically driven assembly. (*A*) 100 mM sodium phosphate at pH 4.2 ^{31}P DOSY fits of Log(ψ) vs gradient strength squared show a linear relationship, indicating that a single diffusion coefficient can describe behavior of phosphorous entities contributing to the observed NMR line. (*B*) Hydrodynamic diameters extracted from the diffusion coefficient from fits in (*A*). (*C*) R_2 and R_1 for potassium phosphate pH 4.5 in the presence of 6k MW polyethylene glycol (PEG) at varying PEG concentrations. Solid lines are quadratic fits to data to guide the eye. (*D*) R_2 and R_1 for orthophosphate pH 4.5 samples at 10 and 100 mM, with varying types of cationic salt chlorides and concentrations. Salt added samples are sodium phosphate salts, while no additional salt samples shown are monophosphate salts with the corresponding potassium or sodium cationic species. Solid lines are third order polynomial fits to data to guide the eye. The R_2 trends follow the predicted trends for the Hofmeister series, while R_1 shows little difference at 10 mM phosphate concentration, but significant differences for different salts at 100 mM.

Manipulation of depletion interactions

Since the experimental results so far suggest dehydration entropy as the driver of phosphate assembly, we designed further experiments to deliberately modulate the phosphate-water interactions by known factors. Since we established a viable interpretation for the change in ^{31}P NMR linewidth and relaxation data, we rely on these readouts to evaluate phosphate assembly formation as a function of temperature.

One can amplify dehydration by the addition of hydrophilic molecular crowders or salting-out salts along the Hofmeister series. The introduction of molecular crowders is a common technique used to reduce the volume of water available for the other molecules of interest in aqueous solution, thus increasing the effective concentration of the dissolved

molecule [88]. A commonly used molecular crowder is polyethylene glycol (PEG); its strong affinity for water over the temperature range of interest is known to drive dehydration and increase the effective concentration of other molecules in solution [89]. As expected, the ^{31}P NMR linewidth at temperatures ranging from 293 K to 343 K increased for phosphate solutions at both 10 mM and 100 mM concentrations with increasing PEG concentrations at 10 wt% and 18 wt%. In order to evaluate whether these observed trends are due to a contrast in solution viscosity, R_2 relaxation extracted from FWHM for two samples of 100 mM potassium phosphate, with and without 18 wt% PEG, was plotted as a function of solution viscosity (Fig. A22). The R_2 relaxation rates of the two samples are not superimposed, indicating that the observed increase in linewidth is not accounted for solely by changes in solution viscosity from the addition of PEG. This observation is consistent with the interpretation that PEG enhances dehydration of phosphates and facilitates phosphate clustering.

Dehydration can also be modulated by the addition of various salts according to the Hofmeister series [90]. This series is used in biological systems to induce salting-out (precipitation) or salting-in (dissolution) of proteins, with NH_4^+ on one salting-out end and Na^+ on the other salting-in end [91] of the series. While phosphate clusters under the here tested experimental conditions are not precipitated out of solution, the magnitude of dehydration, and thus the exchange with and/or formation of assemblies, should increase with salting-out salts and decrease with salting-in salts. To test our hypothesis of dehydration-driven phosphate clustering, we added a variety of cations that enhance the salting-out tendency in the order $NH_4^+ > K^+ > Na^+$. ^{31}P NMR linewidths were measured between 293 K and 343 K for orthophosphate solutions at 10 mM and 100 mM in the presence of added chlorine salt of three different cations at 100 mM and 1 M concentrations, as well as in the absence of added salts. The extracted linewidths show that the addition of NH_4^+ causes the greatest line broadening, followed by K^+ and

then Na^+, at all phosphate concentrations, salt concentrations, and temperatures (Fig. 2.5D). These results are in agreement with the predicted trend of the Hofmeister series when considering line broadening as a proxy for dehydration-induced clustering. While the R_1 results are more difficult to interpret, given the non-monotonic trend, we see that the salts clearly change the shape and magnitude of R_1 when phosphate and/or salt concentration is high enough (Fig. 2.5D). This finding is again in agreement with the hypothesis that the addition of salting-out salts impact the tendency of phosphates to form assemblies.

Molecular crowders and salting-out cations both serve to increase the total entropy of dehydration, further facilitated by elevated temperatures, consistent with the ^{31}P NMR results. While chemical exchange between phosphate species of different protonation states or scalar relaxation may potentially explain some of the observed anomalous ^{31}P NMR line broadening behavior with increasing temperature, these alternative hypotheses do not provide comprehensive explanations for the full range of results provided here. The proton exchange rate for a 100 mM phosphate sample is 10^7 Hz, many orders of magnitude larger than the strength of proton-phosphorus scalar couplings, indicating that scalar relaxation does not dominate. Similarly, a model of chemical exchange between differently protonated phosphate groups cannot explain the order of magnitude discrepancy between R_1 and R_2. This order of magnitude difference between R_1 and R_2 also indicates that paramagnetic impurities could not be causing the enhanced relaxation, as for phosphate and paramagnetic species tumbling freely in solution one would expect R_1 and R_2 to be close to identical. Additionally, these potential explanations fail to explain the other results shown, such as the broad CEST lines, the cryo-TEM images, or the multiple experiments indicating that phosphate dehydration plays a role in modulating ^{31}P NMR relaxation properties.

Chapter 3

Spin Counting of Calcium Phosphate Clusters and Crystalline Species

3.1   Permissions and Attributions

1. The content of chapter 3 and appendix B has been submitted to JPC Letters. It is reproduced here with the permission of The American Chemical Society: Nowotarski, et al. DNP Enhanced Multiple Quantum Solid State NMR Spin Counting of Molecular Assemblies in Vitrified Solutions. Submitted 2023 [35].

3.2   Introduction
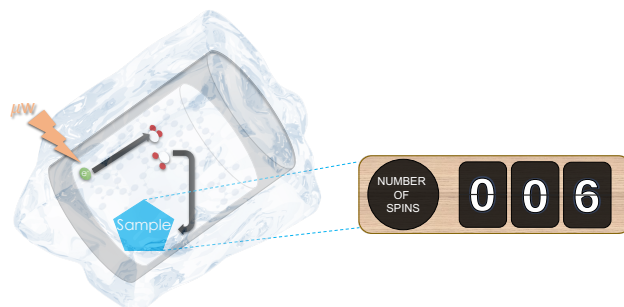
Crystallization pathways are essential to various industrial, geological, and biological processes. Classical nucleation theory (CNT), where a nucleus of critical size grows by the addition of the elemental species (atoms, ions or molecules), does not fully explain crystalization pathways that utilize amorphous or mesocrystalline intermediates. Nonclassical nucleation theory encompasses all known deviations from CNT such as the synthesis of proteins, the formation of calcium carbonates, the growth of mesocrystals, etc.[92], wherein prenucleation clusters form from a supersaturated solution, and subsequently aggregate into a potential glassy intermediate, which then transforms into a crystalline phase. The recruitment of prenucleation clusters (PNCs) is essential to many nonclassical nucleation pathways. For example, the nucleation pathway of calcium phosphate is not well understood and proposed to be nonclassical [93, 94]. Nonclassical growth pathways have significant potential for the development of materials with tunable functional complexity, such as modulating the density of intermediate states, due to additional states and more complex phase boundaries. To design such materials by nonclassical growth pathways, knowledge of the formation mechanism of PNCs is critical. However, PNCs remain mostly elusive to control due in significant part to the intrinsic difficulty of characterizing the highly dynamic structural evolution of prenucleation clus-

ters. Microscopic and X-Ray techniques have been shown to offer some insight into the structure and dynamics of PNCs [95]; however, due to PNCs time transient nature in solution, these techniques are not sufficient or applicable for the study of most PNCs.

Low temperature solid-state nuclear magnetic resonance (ssNMR) is uniquely suited to offer atomic-scale structural information of PNC samples prepared at various time points in nonclassical growth pathways by vitrification at 100 K. Sample vitrification for low temperature ssNMR experiments requires the use of a glassing agent, which assures the integrity of solution-like conditions at cryogenic temperatures with manual plunge freezing. Plunge freezing of a solution containing 60 volume % glycerol can more rapidly cool the sample compared to the equilibration of the sample in the current cryostat, preventing alteration in its composition during cooling. The reason why such high glycerol concentration is routinely used for DNP is that the glass quality of the sample is impervious to the cooling rate history and variation from sample to sample at 60 volume %, but interestingly already not at 50 volume % [96, 97]. The solution sample at specific time points along the growth pathway is preserved by vitrification, resulting in static snapshots of the nucleation process, which can be analyzed by performing ssNMR experiments under DNP conditions. Technology to achieve rapid freeze quench to vitrify solutions without glassing agents is not yet commercially available for ssNMR studies. The main challenge is due to the several tens of μL volume required for a typical ssNMR MAS sample that needs to be vitrified across a sapphire rotor with a 3.2 mm outer diameter (which is a commonly used rotor size). While one can spray their sample into chilled isopentane to decrease the vitrification time required and as such minimize use of cryoagents[98], this setup is not possible for commercial ssNMR Bruker sapphire rotors with capped bottoms as there is no feasible way to separate the isopentane solvent from sample (unless centrifugation at reduced temperature was possible). We did attempt this using a Cryo-EM ethane condenser and brass cup, with blotting excess isopentane

off before packing, however we were unsuccessful. Alternatively, both Tycko, Goldfarb, and Clore have shown that minimizing glassing agents is possible with home-built freeze quench setups[97, 99, 100], only requiring 20 % glycerol [97] and/or 0 % [100] depending. Rapid freeze quench without glassing agents is a solvable problem with future technological developments of spraying small sample streams onto a cold rotating plate or into cooled isopentane that can be squeezed out of an open ended sapphire rotor. With the increasing popularity of DNP-NMR and electron paramagnetic reconance (EPR) studies of vitrified samples, we believe such technology will become commercially available.

Phosphates are ubiquitous within the biologic and industrial materials fields, serving as essential energy storage vehicles and structural units [42, 43, 44, 45, 46]. Phosphates have also recently been shown to exhibit liquid-like clusters in solution, presenting additional complexity to understanding the growth of phosphate-containing structures [41]. The nonclassical nucleation of calcium phosphate clusters as the precursors to bone formation [101] has been observed within seconds at concentrations which are only accessible to NMR enhanced by dissolution DNP [55], resulting in inadequate time for structural analysis. Sample vitrification and MQCO extraction at various early stage time points would allow for monitoring PNCs and the evolution of calcium phosphate phase formation. The feasibility of MQ-SC in vitrified solutions under DNP conditions for ^{31}P species should be relevant to the many biological and chemical processes that use phosphate containing species as structural building blocks or energy sources. Our studies show the feasibility of DNP-enabled MQ-SC and can be expanded to any spin $\frac{1}{2}$ system in the future.

In the case of calcium phosphate, understanding the assembly and growth mechanism(s) of phosphate clusters is the first step in elucidating the structure and evolution of the various species formed. In this effort, the most rudimentary question is how many phosphorous atoms are correlated in the species formed along the phosphate nucleation

growth pathway? This question can be answered by counting the number of coupled
[31]P spins with multiple quantum NMR (MQ-NMR) spin counting (MQ-SC)[39]. In fact,
MQ-SC might be the only technique available to count the number of coupled nuclei
in soluble, small clusters of magnetically indistinct environments. Notably, while spin
counting has been utilized to characterize amorphous or crystalline solids, it has never
been applied to characterize the structure of soluble assemblies and clusters in solution
upon vitrification.

Spin counting is an experimental NMR technique where Multiple Quantum Coher-
ences (MQCOs) are created between dipolar or J-coupled nuclear spins. In such experi-
ments, a coherence is defined as a multiple spin transition (forbidden but made allowable
by spin-spin coupling) from different ground states to the same excited state at the same
time and with the same phase[102]. The number of neighboring nuclei, the distances
between them and the uniformity of their spatial arrangements determine the number
of MQCOs one can detect[103], along with the mode of MQCO excitation[104]. While
traditional MQ-NMR employs standard phase cycling to select each coherence order in a
separate experiment, MQ-SC experiments increment the phase of either the excitation or
reconversion block, allowing for different coherence evolution in a single experiment[39]
(Fig. B1). MQ-NMR spin counting still requires multiple experiments to extract the indi-
vidual frequencies of each coherence order, which is either done via a 2D experiment with
time-proportional phase incrementation, in which the excitation pulse phase increment is
proportional to the t_1 evolution or via a pseudo 2D experiment with the excitation pulse
phase incremented and directly detected in the t_2 dimension[39, 105]. MQ-SC has been
performed on crystals[106, 107, 108, 109, 110, 111, 112], liquid crystals[113, 114], minerals
[115, 116, 117, 118, 119], catalysts/zeolites [119, 120, 121, 122, 123, 124, 125, 126, 127],
glasses[128], molecules[129, 130, 131], amorphous semiconductors [113, 132, 133], hybrid
materials[134], thin films/polymers [135, 136, 137, 138], diamond surfaces[139], and pep-

tides/proteins [140, 141, 142, 143, 144], all under static or varying magic angle spinning (MAS) rates with various nuclear spins (S=1/2 and 3/2[145, 146]) and employing zero quantum, single quantum, double quantum (DQ), or triple quantum (TQ) propagators. The aforementioned extensive history of successful spin counting experiments demonstrates it as a reliable technique, however MQ-SC under DNP conditions of solution species vitrified in a frozen matrix has never been performed by any study reported to date to our knowledge. Our critical case study provides an avenue for future studies of solution intermediate states, showing the feasibility of quickly analyzing these otherwise indistinguishable spectroscopic signatures, even when suffering from low sensitivity.

Here, we present novel ^{31}P NMR spin counting studies of both powdered and vitrified phosphate-containing samples, for which we have extracted the minimum number of dipolar coupled spins via the creation of multiple even and odd quantum coherence orders [39] using the SR2$_8^1$ pulse sequence[108, 147] (see Fig. B1 and Supporting Information Listing 2 [35]), where the overall phase of the excitation block is incremented in a pseudo 2D mode to extract the MQCOs. The SR2$_8^1$ pulse sequence is an R-symmetry based double quantum recoupling sequence[148] which works with a low radio frequency power requirement equal to half the spinning frequency, hence permitting longer recoupling times. Longer recoupling times are required to generate the higher multiple quantum coherences.

3.3   Results and Discussion

3.3.1   Spin Counting of Powdered Phosphate Samples at Room Temperature and Vitrified Phosphate Solution Samples at 100 K

In this study, we present proof of concept applications of MQ-SC experiments on powdered and their respective vitrified solution species counterparts, along with a novel calcium phosphate time stabilized prenucleation system. We focus first on both discrete and extended ^{31}P dipolar coupled systems for spin counting studies, demonstrated respectively for molecular adenosine triphosphate (ATP), amorphous calcium phosphate (ACP) and crystalline hydroxyapatite (HAp) ($Ca_5(PO_4)3OH$), where ACP is an amorphous precursor to HAp in the crystallization pathway of calcium phosphate[149]. We then discuss experiments with a modified simulated body fluid (mSBF)[150, 151] shown to contain calcium phosphate prenucleation clusters [152], which spontaneously phase transform and aggregate to form ACP[31]. We have prepared our samples according to common dynamic nuclear polarization (DNP) sample preparation practices. DNP typically utilizes stable bi-radicals (in our study, AMUPol) by saturating the EPR resonance of a sub-population of the bi-radicals via microwave irradiation to transfer polarization to nuclear spins of the solvent, resulting in significant signal enhancements[153]. All three samples were prepared for vitrification in a solution of 6:3:1 parts by volume glycerol-d8, D_2O, and H_2O respectively with 10 mM (Fig. 3.1 and 3.2) / 6.67 mM (Fig. 3.3) AMUPol (referred to as DNP juice). Samples were first prepared in 100 % H_2O or 75/25 % D_2O/H_2O (see B.1 Materials Section and Fig. 3.2C for methodology), then the bi-radical AMUPol and glycerol-d8 were subsequently added.

For our study, we disregard the potential impact of the paramagnetic polarizing and

glassing agents on the reaction pathway, given that the chemical shift between powdered and vitrified samples closely align for HAp, ACP, and ATP samples (Fig. B5, B and C). The effect of glycerol on the non-classical growth pathway to form ACP from modified simulated body fluid (mSBF) samples containing PNCs cannot be verified given that there is no powder sample for comparison. We found that glycerol can increase the solubility of ACP at lower calcium and phosphate concentrations (verified by DLS, solution NMR, and ssNMR not shown in this paper), but the systematic and mechanistic study of the role of glycerol in modulating the equilibrium or kinetics of the non-classical growth pathway of ACP is outside the scope of this study[154]. Here, we only focus on the question whether DNP-enhanced NMR of manually plunge frozen mSBF samples, en route to ACP solids, can capture vitrified intermediate species in solution state and whether ^{31}P MQ-SC can identify one or more of these species to be PNC candidates.

MQ filtering efficiencies represent the ability for a pulse sequence to filter out all spin flip transitions other than the specific MQ transition. We find that the large chemical shift anisotropy (CSA) of ^{31}P nuclei in nonsymmetric molecular systems such as ATP (Fig. B7) [155] reduces the DQ filtering efficiency of the $SR2_8^1$, $R14_2^6$, and SPC-5 pulse sequences, with $SR2_8^1$ expected to be minimally sensitive to CSA and capable of delivering a theoretical maximum efficiency of around 50 %. Under our experimental conditions, the DQ filtering efficiencies for powdered ATP samples were found to be 3.12, 3.125, and 5.40 % when using the $SR2_8^1$, $R14_2^6$, and SPC-5, respectively. In contrast for powdered HAp, the experimentally measured DQ filtering efficiencies were found to be 45, 34.5, and 41.1 % when using the $SR2_8^1$, $R14_2^6$, and SPC-5, respectively. Based on these results, we decided to continue our experiments on each sample with $SR2_8^1$ to achieve DQ and TQ filtering efficiencies (Supporting Information Listing 1 [35]). We found an optimal excitation time of 1.6 ms (mixing time of 3.2 ms) at a MAS frequency of 10 kHz for each sample. Crystalline HAp exhibits an extended spin lattice network with a DQ/TQ

filtering efficiency of 45/6.56 % at room temperature and a DQ efficiency of 38 % at 100 K in DNP juice. Powdered ACP was found to have a slightly lower DQ filtering efficiency of 43 % at room temperature and a DQ/TQ filtering efficiency of 33.4/3.7 % at 100 K in DNP juice. At both room and vitrified temperatures, ATP suffered from low DQ and TQ filtering efficiencies of 3.12/0.28 % when powdered at room temperature and 1.3/0.4 % at 100 K (20 and 40 mM ATP in glycerol-d8 DNP juice). The mSBF sample suffered from low overall signal, thus not allowing for TQ filtering signal even after 1024 scans. However DQ filtering efficiency for the mSBF was determined to be 6.25 % at 100 K in DNP juice. Sodium monophosphate standard sample exhibited no DQ filtering signal as expected, even after 512 scans.

Depending on the sample and experimental conditions, both intramolecular and intermolecular coherent spins can be probed by MQ-SC. In simulations of MQ-SC experiments (Fig. B8), up to 6 coherence orders can be seen in a linear chain of ^{31}P spins separated at a distance of 2.5 Å in between. We optimized the excitation time at a MAS frequency of 10 kHz (Fig. B11) with the DQ filtering pulse sequence in order to maximize the extracted MQCOs, and found an excitation time of 8 ms to be optimal across all different powdered samples and their respective vitrified counterparts (Fig. 3.1 and 3.2). The mSBF sample, however, had an optimal excitation time of 4.8 ms for the middle CS environments which could only be determined by MQ-SC experiments due to low DQ filtering signal (Fig. 3.3C and B14). We ensured that the recycle delay and mixing time are set appropriately based on experimental relaxation parameters (See Fig. B11 and B12). We employed these optimal parameters for spin counting experiments utilizing the SR2$_8^1$ pulse sequence to count the even and odd coherence orders (Fig. B1). When examining a MQ-SC profile in order to determine the minimum number of clustered spins, any odd coherences shown for the even order MQ-SC profile (and vice versa) can be attributed to experimental noise and MQCO leakage caused by imperfect filtering of
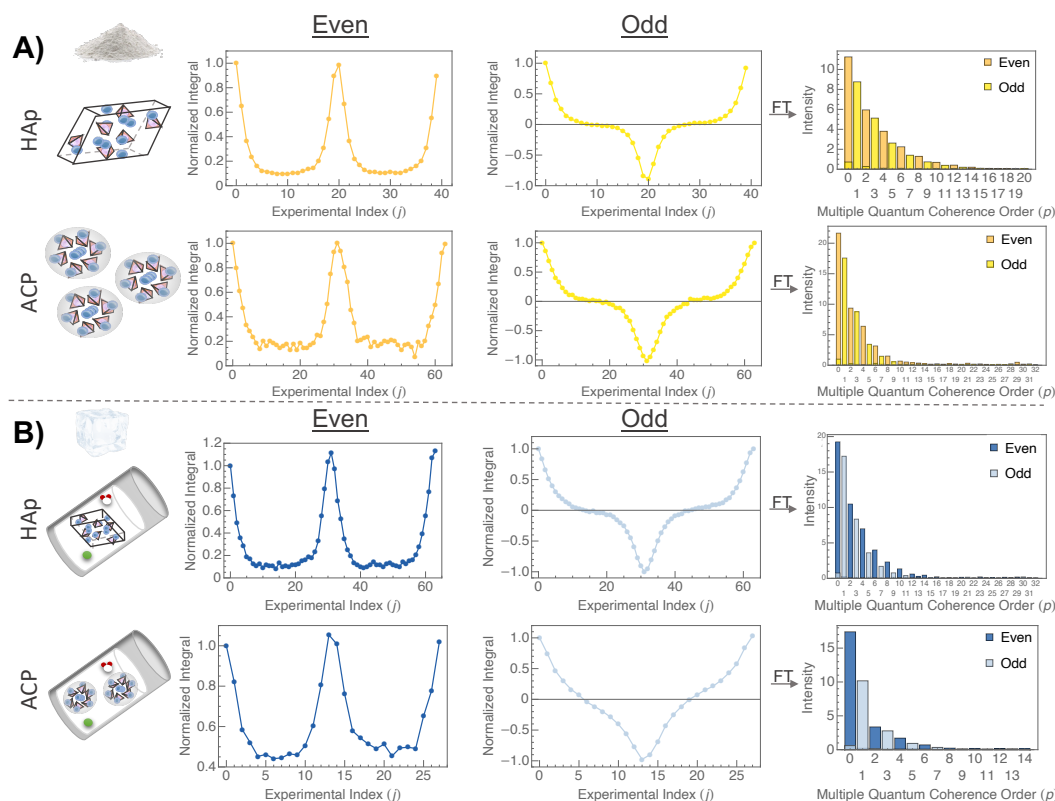
46

Figure 3.1: Even and odd spin counting profiles and subsequent Fourier transformed MQCO (p) profiles at 10 kHz MAS and 8 ms excitation time for HAp (unit cell coordinates from reference [37]) and ACP at A) Room Temperature B) 100 K Vitrified Conditions in DNP juice using $SR2_8^1$ modified pulse sequence (See Fig. B1) and a relaxation delay of 5 s. The x-axis of the spin counting profiles is represented as experimental index (j), where phase is incremented each index by $360°$/experimental index. All spin counting profiles' integrals were normalized to the integral of the first experiment ($j = 0$). The SC profiles represent the summation of all excited MQCO transition frequencies, which are extracted and discretized via Fourier transform into MQCO profiles.

the double quantum recoupling sequences (Fig. B8). The zero order coherence for even MQCO profiles is attributed to z-magnetization of the spins. In addition, we discovered that replacing intensity of each peak (as previously employed in MQ-SC studies) with the integral during analysis yielded more precise extracted MQCO values for higher noise data sets and the same MQCO values for low noise sets.

We show in Fig. 3.1 signal integral of each MQ-SC experiment as a function of the excitation block pulse phase and the resulting Fourier transformation of all experiments which yields the amplitude for the MQCO for each phosphate-containing species, in powder form at room temperature (A) and vitrified at 100 K in DNP juice (B). We find for HAp even and odd coherence orders up to 14 and 13, respectively, at room temperature (Fig. 3.1A). When samples are dissolved into DNP juice and characterized at 100 K, we find the measured coherences orders to be comparable at 14 and 11 for the same excitation time (Fig. 3.1B). Similarly, we find for ACP even and odd coherence orders up to 10 and 9 at room temperature, and 8 and 7, respectively when dissolved into DNP juice, vitrified and measured at 100 K for the same excitation time. The loss of coherence orders at 100 K can be attributed to a shorter T_2 relaxation time of the vitrified sample compared to room temperature. Shorter T_2 will result in shorter recoupling times and the inability to excite higher order MQCOs of species with partially averaged out dipolar couplings, thus limiting the overall shape of the MQCO profile and the total intensity achievable for each individual MQCO. In addition, decreasing the concentration of the sample in DNP juice leads to a smaller total number of excitable MQCOs, and an overall decrease in MQCO intensity. Even spin counting experiments on ATP yielded the expected coherence order of 2 (Fig. B9), and odd spin counting experiments on ATP yielded the expected coherence orders of 3 (requiring additional experimental procedures discussed later) for the alpha, beta, and gamma phosphorous chemical shift environments at room temperature (Fig. 3.2C). This observation is consistent with the selective buildup of intramolecular

coherence orders in ATP. To further validate that intermolecular coherence orders are not contributing to the MQCOs of ATP in solution, a sodium phosphate control sample and monophosphate breakdown species in ATP vitrified samples (Fig. B10) were examined. There was no signature of any coherence order exceeding 1, which is expected if intermolecular dipolar couplings do not contribute to the buildup of MQCOs. Due to a combination of factors, including high CSA (Fig. B13) and imperfection in the glassing matrix, the MQCO extraction from ATP under DNP conditions was more challenging than that from HAp and ACP. As a result, a MQCO of 3 could not be always extracted under all experimental conditions, as will be discussed in the following paragraph. We can currently conclude that as the number of intramolecular phosphate bonds and long range order increases, the extracted MQCOs increase, as seen with increasing MQCOs in the order of ATP, ACP, and HAp. We find that the process of vitrification does not drastically affect the extracted coherence orders and any loss of MQCO can be attributed to a decreased signal to noise ratio due to shortened T_2 relaxation at low temperature.

The extraction of a coherence order of 3 for ATP as a proxy for MQ-SC in disordered PNC systems in DNP juice at 100 K was challenging. To improve our understanding of solvent interactions, we explored the effect of different solvents and vitrifying methods to mitigate the MQCO dampening effects seen with MQ-SC of ATP. We first explored utilizing DMSO instead of glycerol as a glassing solvent in a 77:17:6 DMSO-d$_6$:D$_2$O:H$_2$O ratio [157], which prolonged the long T_2 component from 12.95 ms (in glycerol) to 13.56 ms (in DMSO) (Fig. B12). We observed a minimum of 5 MQCOs across the alpha, beta, and gamma chemical shift environments for ATP in DMSO (Fig. 3.2C), which we can attribute to intermolecular clustering of ATP, presumably via hydrophobic interactions. We returned to the glycerol:D$_2$O:H$_2$O mixture since DMSO appeared to induce clustering. When using the glycerol:D$_2$O:H$_2$O mixture, we tested the effects of order of dissolution of the solution constituents, ATP concentration, and vitrification procedure
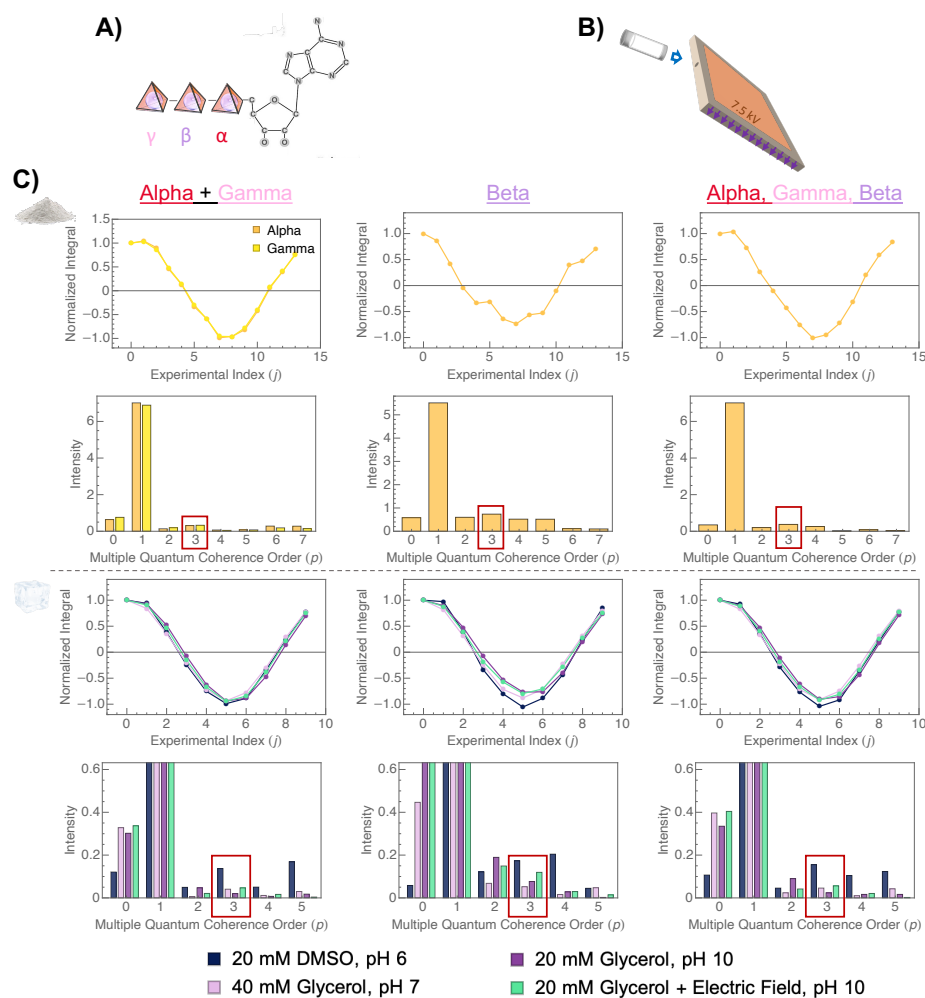
Figure 3.2: A) Labeled PO$_4$ sites γ, β, and α, equivalent to Q1, Q2, and Q1 respectively [156]. B) Rendering of electric field setup. 3D printed rotor holder with copper plates on both sides connected to a 7 kV source. Purple arrows indicate electric field direction. C) Odd spin counting profiles and extracted MQCO charts for room temperature powdered and 100 K vitrified ATP samples at 10 kHz MAS and 8 ms excitation time. 100 K MQCO charts were zoomed in for visual ease. Each chemical shift range assigned to individual PO$_4$ sites was chosen based upon ^{31}P spin connectivity determined in Fig. B5 and B6. 40 mM ATP (final concentration in DNP juice) was prepared by dissolving ATP first in H$_2$O and D$_2$O, then added to premeasured AMUPol, and lastly glycerol-d8 was inserted. 20 mM samples (final concentrations in DNP juice) were prepared in the dissolution order of AMUPol, H$_2$O,D$_2$O, glycerol-d$_8$/DMSO-d$_6$, ATP and lastly pH correction with 1M NaOH to 10 if applicable. All experiments were taken with a relaxation delay of 6 s. ATP in DMSO exhibited a final pH of 5.88. Monophosphate breakdown can be viewed in Fig. B10.

to minimize clustering and to push the equilibrium towards deprotonating the phosphate O-H bonds (Fig. 3.2C). These modifications resulted in an elongated T_2 from 8.32 ms to 17.92 ms. The longest T_2 relaxation was from a sample that was prepared by freeze-pump-thaw procedure (in order to increase glassing homogeneity) and Ar (g) was used as a final flush (to mitigate paramagnetic relaxation due to dissolved gasses), however this sample resulted in large even MQCO noise (not shown). The next longest T_2 was 12.95 ms for 20 mM ATP in glycerol, resulting in 3 weakly visible MQCOs. While successful, we attempted to push the limits of this technique to confidently distinguish the third MQCO from noise. We exposed 20 mM ATP in glycerol at room temperature to an electric field of 7 kV for 3.5 minutes (Fig. 3.2B), then immediately plunged the entire system with power on into liquid nitrogen for vitrification. This setup was inspired by a study from Tang et al.[158] to align the aromatic rings of ATP with an electric field. When exposed to an electric field, Tang, et al. found an increase in stacking probability due to the molecules becoming more planar, leading to an energetically preferred π-stacking configuration. An increase in stacking alignment would consequently decrease T_2 relaxation caused by CSA in our samples, which is one of the main limiting mechanisms to MQCO build up. It is additionally possible for the paramagnetic polarizing agent AMUPol to align similarly and cluster when exposed to an electric field, which would likely lead to a change in DNP enhancement mechanism, potentially from solid effect or cross effect to thermal mixing [159]. This change in DNP mechanism would be reflected in the efficiency of DNP buildup, however microwave efficiency was unaltered from electric field exposure. The experimental results show that the CSA increased for some phosphate environments and decreased for others in a nontrivial manner (Fig. B13) and T_2 relaxation decreased from 12.95 to 11.39 ms. Still, the third MQCO when compared to 20 mM Glycerol, pH 10 control sample became more visible in every CS environment after the exposure of the ATP solution in DNP juice to an electric field. While the third MQCO for all

molecular ATP samples still has lower intensity than ideal and sometimes does not exceed the even MQCO noise level, future applications of this method to PNCs that have greater symmetry and/or contain many more than three atoms will prove more fruitful. For example, an ongoing study in our group led by L. R. Potnuru on the assembly of phosphorylated proteins show that the minimal CSA of phosphate groups makes spin counting of a high MQCO of a complex vitrified sample such as a fibrilized Tau proteins out of solution feasible. In the next paragraph, we will showcase a first proof of principle study that achieves the detection of transiently formed phosphate prenucleation clusters upon vitrification in solution by DNP-enhanced MQ-SC.

In the pursuit of a system with a prenucleation cluster which would likely exhibit less CSA[7] than molecular ATP, we set out to arrest calcium phosphate prenucleation clusters which have been studied by Epasto, et al[152]. With a few slight adjustments in the sample preparation procedure (B.1 Methods), we were able to replicate their solution ^{31}P NMR experimental conditions (Fig. 3.3A), however with a faster transition timescale, where the splitting of the ^{31}P solution NMR lineshape offers evidence for the formation of approximately 2 nm size PNCs exchanging with free dissolved phosphate according to Kurzbach and coworkers[152]. We could not perform DLS on our mSBF recipe due to the presence of HEPES agent, which obscures other similar or smaller sized particles around 1 nm; we did remove HEPES buffer from this mSBF at some point and still saw ^{31}P solution NMR line splitting with time however the total signal intensity was lower and line broadness was increased. It is well known among groups that study these processes that PNC formation is a kinetic process that is highly sensitive to any experimental variation, including the choice of buffer, temperature, certainly the exact composition of the mSBF and even the order and method of salt mixing. Further complicating interpretation, the solution ^{31}P NMR chemical shift of monophosphate salt is dependent on the total ionic strength of the solution in a nonlinear relation (likely due
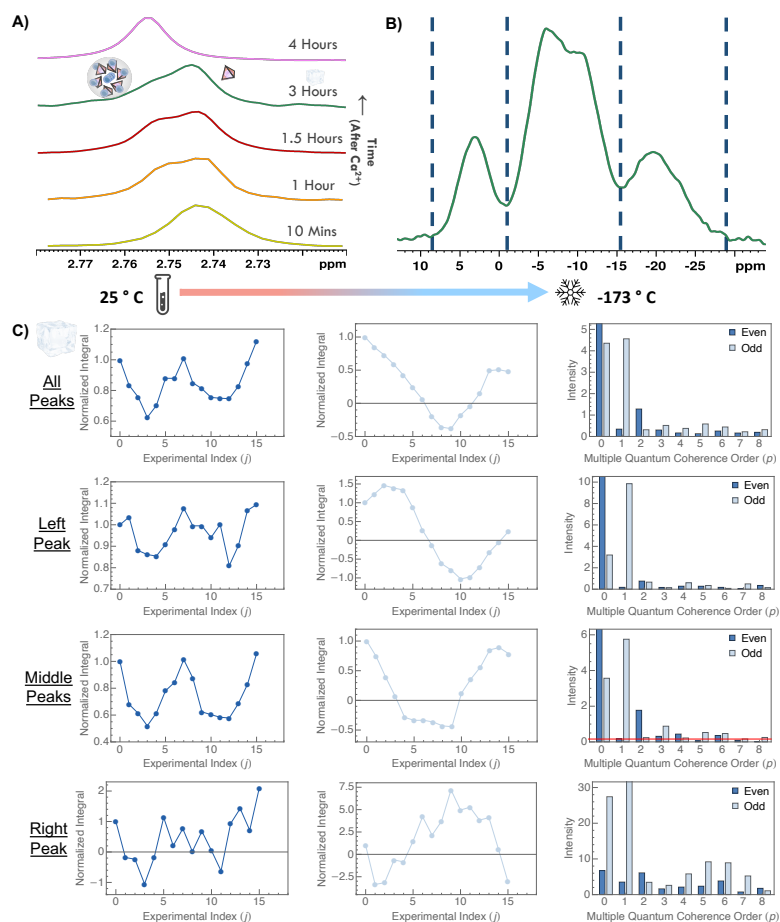
Figure 3.3: MSBF solution and vitrified sample. In A), direct ^{31}P solution NMR time evolution of mSBF solution in 90 % water and 10 % D$_2$O by volume, with total solution concentration of 1.32 mM and 0.6487 mM phosphate and calcium respectively (along with other salts mentioned in B.1 Materials). These spectra were all chemical shift corrected to a phosphoric acid coaxial insert based upon a sample taken a month prior. An aliquot was taken at the 3 hour mark after addition of calcium and taken for DNP juice preparation and vitrified, found in part B. When left to react over a time period of 24 hours or greater, the peak continues to shift left slightly and sharpens drastically, likely forming crystalline HAp. In B), the ^{1}H to ^{31}P cross polarization 1D Spectra of vitrified mSBF (referenced to phosphoric acid) in 60 % volume glycerol and final concentrations of 0.147 mM phosphate and 0.072 mM calcium (complete solution preparation in B.1 Materials. The ^{31}P T$_1$ relaxation was found to be greater than 100 s. The regions defined are those analyzed in part C), Spin counting of vitrified mSBF sample. The MQCO plots are zoomed in for viewing ease. The two middle peaks were merged into one chemical shift region for SC experiments. Even and odd SC experiments were taken with a D1 of 5 s and excitation time of 4.8 ms (optimal) at 10 kHz MAS. The right chemical shift environment suffered from low signal for even and odd SC, even at 256 and 512 scans respectively. The red horizontal line for the middle CS environment is the average odd MQCO noise for the even MQ-SC experiment.

to effects such as water hydration structure and extent of hydration), while conversely related to the pH and temperature[41] of the solution in a linear relation (Fig. B15). The elucidation of PNC formation pathways is beyond the scope of our study, but one that can be facilitated by MQ-SC under DNP conditions.

We were able to extract an approximate ^{31}P solution NMR T_2 relaxation for the splitting time point of 6.14 ms and a T_1 of 7.4 (monoexponential fit)/ 95% 7.94 s and 5% 0.47 s (biexponential fit) with an error of 0.5 s. We arrested the solution at three hours when there was explicit NMR splitting that had been stable across a formation time of a few hours, by adding AMUPol already dissolved in D_2O, then glycerol-d8, and lastly plunging the sample in liquid nitrogen. The resulting final vitrified sample consisted of 0.147 mM phosphate and 0.072 mM calcium total. A 1D ssNMR spectrum was acquired of this sample. Four distinct ^{31}P NMR chemical shifts appeared (Fig. 3.3B). We completed even and odd spin counting experiments on this sample and analyzed these chemical shift environments (Fig. 3.3C), where the middle peak two environments were combined into one due to their very closely overlapping chemical shifts. We extracted even ordered experimental minimum MQCO's of 2, 6, and 2 for the left, middle, and right peaks respectively. The odd spin counting experiments show MQCOs of 1, 5, and 1 for the left, middle, and right peaks respectively. Both odd and even spin counting experiments have different experimental noise levels due to acquiring disparate scans because of limited signal; noise levels for even and odd MQCO experiments should be extracted from the same experiment type. For an even MQ-SC experiment, one should examine the even experimental noise in dark blue for the odd coherence orders. We have added a red horizontal line as the average odd MQCO noise for the even MQ-SC experiments, where any even MQCOs above this line are above the average noise for that experiment. The left peak exhibits a very small MQCO of 2 for all excitation times (Fig. B14) and has significant overlap with the CS of monophosphate control sample, thus it is likely leakage

from the middle CS environment. The right peak environment was difficult to distinguish from noise during analysis and as evidenced by the even and odd SC profile showing no discernible cosinusoidal shape or meaningful Fourier transform, resulting in an extraction of 2 MQCOs. This might be due to the presence of a significant population of isolated phosphates present, not enough scans acquired, or due to a different optimal excitation time of 3.2 ms / mixing time of 6.4 ms (Fig. B14, MQCO of 2 is clearly extracted). This middle merged peak environment has a T_2 relaxation of 14.17 ms (which is more than the experimental mixing time of 9.6 ms) and exhibits a lower CSA than most environments for ATP in DNP juice, resulting in an extracted MQCO of a minimum of 6. Considering the MQ-SC results of model systems and fully formed HAP crystals and ACP solids, the observation of such a high and distinct MQCO of 6 is astonishing. The species giving rise to MQCO of 6 could be small ACP solids or likely a calcium phosphate prenucleation cluster (or both due to the presence of two overlapping peaks), potentially even including the Posner cluster which is proposed to be made of six phosphate atoms [24, 36, 7]. These exploratory results can be expanded upon with further structural analysis in the future. It is important to note that we did once attempt to run a mixed DNP sample of HAp dissolved powder and ATP, which resulted in a total extracted MQCO of 0; this is still puzzling and our best interpretation at the time was the presence of multiple states resulted in a total null result. If there are more total coherences in a system, the SC profile should widen to a U shape and the y-axis should deepen. We additionally tried to run DLS on the mSBF sample before vitrification to ensure the size of the solution NMR splitting time point species was not on the scale of ACP (10 - 300 nm), however we were not successful in initial attempts due to logistical issues. It should also be noted that we also tried native [43]Ca on this sample as well, and only saw background probe signal.

In summary, the successful counting of ^{31}P nuclei clustering in vitrified solutions pro-

vide a novel structural analysis approach to characterize nonclassical growth pathways that include pre-nucleation clusters as intermediate species. MQ-SC might be one of the few techniques that can identify the formation of clusters made of the same species, here phosphates, that do not have distinguishable spectroscopic signatures between the coupled species. For clusters that cannot be isolated and/or are too small or with too little contrast to be captured by electron microscopy or various light scattering techniques, MQ-SC might in fact be the only approach to identify the minimal number of coupled phosphates in the cluster. In future studies, performing spin counting experiments on prenucleation cluster species at lower concentrations than as found in this paper would require conducting more scans. In this study we showed that increasing the molecular order increased the measured MQCOs for both powdered and vitrified solutions. Asymmetric molecular systems may require additional sample preparation optimization under vitrified conditions in order to mitigate CSA relaxation effects, such as electric field exposure for aromatic systems as demonstrated here. We show that one can go down to sub milimolar concentrations for a proposed calcium phosphate prenucleation cluster and still extract an MQCO order of 6. MQ-SC opens the door for extracting quantitative information at newfound atomic-scales in dynamic systems. Spin counting experiments can be applied in the future to test various nonclassical growth models, such as further examination of the calcium phosphate nucleation pathway with simplification of our simulated body fluid recipe. Shedding light on calcium phosphate assembly will pave the path for future bone and biomimetic material technologies and potentially identify a source of mammalian information storage [25, 7].

3.3.2   Vitrification Methods & Design of Rapid Freeze Quench

A glass is an amorphous material which does not possess any long range crystalline order, similar to a liquid which exhibits random orientations due to translation and rotation. Many spectroscopic techniques require solid materials for analysis, therefore in order to analyze a liquid sample (or a species in a liquid sample which can not be dried down) in a solid state, many researchers attempt to instantaneously solidify the sample into a glassy structure by means of vitrification. This can be achieved by rapid cryogenic temperature transfer (135 K for pure water [160, 161]), where addition of glassing agents decreases the swiftness necessary. Glassing agents (or cryoprotectants) are used commonly for magnetic resonance techniques (EPR, NMR), electron transmission microscopy, and the storing of biologic tissues. In order to prevent ice formation, crystallization of the system of interest, and the potential subsequent dehydration of systems, cryoprotectant agents are utilized to mimic the natural state of a solution system at cryogenic temperatures by shifting the vitrification/glass transition temperature higher in order to allow for more robust glassing.

The most commonly used glassing agent is glycerol at 60 volume % for DNP-NMR, 30 volume % for EPR, and 15 % for cellular DNP-NMR [162, 163], while Cryo-EM samples usually use no cryoprotectants due to the small volume and large surface area of sample needed to vitrify. Glycerol has been shown to result in robust glassing independent of the rate of sample cooling at greater than or equal to 60 volume % [96, 164], and as little as 20 volume % glycerol with a rapid freeze quench setup (Fig. S3 [97], 10 volume % unreported). However, most do not consider the solubility effects of glycerol (a known hydrophilic molecule) on their system of interest. While there are alternate glassing agents such as DMSO (77 volume % [157]), ethylene glycol (EG), propylene glycol, sucrose, trehalose, neutral amino acids, and various polymers such as polyethylene

glycol (PEG) [165], they all pose unique solubility and cooling rate effects [166] as well on the system of interest (30 % EG, sucrose, and glycerol vary in EPR distance distributions by 10 Åas measured with EPR by Yann Fichou, not shown). We have seen via DLS in Fig. 3.4 that amorphous calcium phosphate around 200 nm (formed from a standing simple SBF sample) dissolves when varying volume %'s of glycerol are added to solution (increasing phosphate solubility), however smaller calcium phosphate species formed from a mSBF solution (along with ATP tested independently) cluster together when 60 volume % DMSO is added to the solution (decreasing phosphate solubility). When compared to the addition of 6 kDa PEG at 60 volume %, the aforementioned smaller calcium phosphate species appear minimally affected by PEG glassing agent (Fig. 3.4). We then decided to replicate these PEG results and further study if PEG was melting the calcium phosphate species of interest, which is obscured in DLS by the large scattering of PEG control solvent. We chose to add 10 kDa PEG (with an LCST above room temperature) to a simple SBF solution (5 mM $CaCl_2$, 2 mM $KHPO_4$, 250 mM KCl at pH 7, filtered for 15 minutes at 15 mL/minute rate through a 0.2 micron filter, known to exhibit a 1 nm calcium phosphate signature [34]) at room temperature for a final concentration of 40 volume % PEG. The DLS showed very slight growth when PEG was added via a small increase in ACF count rate, indicating a similar solution solubility to no glassing agent solution control (not shown). We then added in 10 mM AMUPol, vitrified this sample by plunge freezing in liquid nitrogen, and ran DQ and TQ filtering at 10 kHz MAS and 1.6 ms excitation time at 100 K. We achieved 3.7 and 1.6 % efficiencies, respectively. We verified this solution was indeed glassing via DSC, with only a very small crystallization peak (not shown). We attempted MQ-SC experiments, to no success, likely due to a mixture of phosphate states. Interestingly, the line broadness of this PEG SBF vitrified ssNMR sample (not shown) was similar to that of the dissolved sodium monophosphate vitrified control sample, slightly broader than the mSBF vitrified sample individual peaks, and

much broader than both ACP and HAp vitrified samples (all mentioned in the previous section). The current working explanation is the smaller the system of interest (phosphate molecule or network), the more ssNMR line broadness due to proximity to an electron radical.
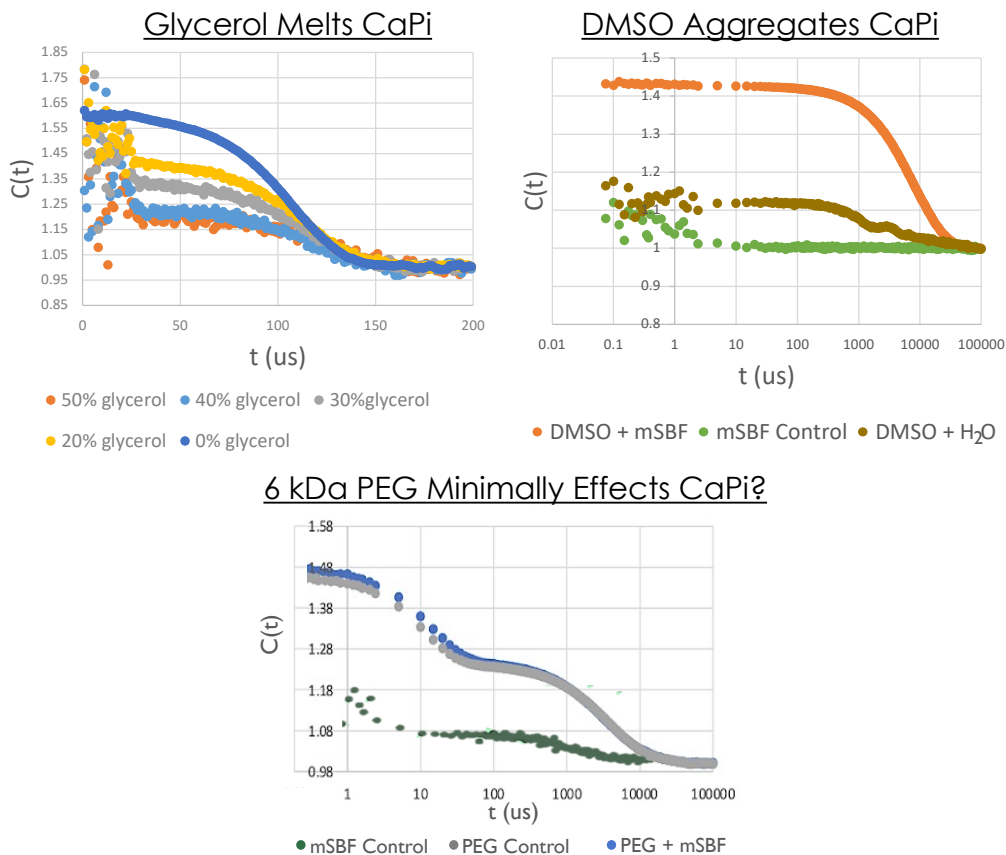

Figure 3.4: DLS ACFs of ACP formed from simple SBF protocol [34] (top left) and mSBF samples [35] (top right and bottom). mSBF control includes $CaCl_2$ addition and no glassing agent (top right and bottom). DMSO + water and PEG control are the solvent controls without any salts/calcium phosphate species. DMSO + mSBF and PEG + mSBF are the final solutions of interest where the glassing agent was added to the mSBF control solution. These ACFs are not viscosity corrected (viscosity shifts the x-axis to the right).

Plunge freezing quickly into a cryoagent such as liquid nitrogen or liquid isopentane cooled close to liquid nitrogen temperatures limits the time atoms can rearrange into a crystalline orientation or an alternate temperature-dependent energetically favorable

orientation, thus resulting in a more native representation of the state. Due to the Leidenfrost effect (which creates a vapor layer around the sample container once plunged into a cryoagent at a significantly lower temperature than the sample), the sample holder thermal conductivity, and the volume of sample, there is time for ssNMR and EPR samples to reorient themselves and/or partially crystallize as the cryogenic temperature penetrates to the core of the sample last. While for this dissertation, 3.2 mm sapphire rotors were utilized for all DNP ssNMR studies, other groups such as Tycko utilize 4 mm ZrO_2 rotors for DNP studies. Dr. Blake Wilson studied the time it took for the middle of a 4 mm ZrO_2 rotor to reach cryogenic temperatures once plunged into liquid nitrogen from room temperature by placing a Pt resistor inside the rotor filled with 40 volume % glycerol / water solution and monitoring the temperature by the resistance. The sample took approximately 22 s to reach liquid nitrogen temperatures and cooled at around 6 - 7 K/s in the 300 K to 170 K range. This is a significant amount of time for sample reorientation, which led us down the path of investigating alternate vitrification procedures. If one is interested in testing the vitrification time, alternate methods to a Pt resistor such as monitoring the temperature dependent bromine NMR chemical shift of KBr or optically timing a dyed droplet are feasible.

We previously discussed the various home-built rapid freeze quench (RFQ) systems for NMR samples in section 3.3.1. There is one commercialized system for EPR samples from BioLogic, however this system has huge temperature variations due to the length of the dewar holding cooled liquid isopentane. We decided to build our own homebuilt RFQ system that can be used for both NMR and EPR samples. We used a copper spinning plate due to the high thermal conductivity and high heat capacity/thermal mass; the conductivity was similar to aluminum, but the heat capacity is much higher. The plate can be lifted and lowered into the liquid nitrogen bath as needed for cooling and sample preservation. Peek tubing attached to a syringe (for sample loading) is mounted

at an approximate 45 degree angle to an Argon (g) line with a plastic pipette tip (not metal needle as it will freeze) for sample spraying of micro droplets. Separate threaded, counterbalanced copper attachments on the edge of the plate were made to hold two small centrifuge tubes (for EPR sample collection and separate packing) or two sapphire rotors for direct packing. For usage, the metal plate is first partially cooled with liquid nitrogen, then a makeshift glove box is placed on top of the setup and a nitrogen gas line is flowed into the box to bring humidity down to approximately 10 - 15 % for condensation minimization. Once the plate is cooled to a minimum of 135 K [160, 161] and humidity is low enough, the plate is raised so that the surface of the copper is just above the liquid nitrogen level and still below the vapor layer. A drill is then used to spin the plate from the outside of the glove box at the lowest, most steady spin setting, and the sample is sprayed using a syringe attached to the PEEK tubing; one must be cognisant not to spray over any previously vitrified sample. Once spraying has concluded, the plate and sample are dropped into the liquid nitrogen and the sample is then collected into the appropriate threaded copper attachment using a Teflon scraper. Both EPR and NMR samples must stay under liquid nitrogen the entire time after collection and must be transferred into the respective probe quickly [167]. The exact setup RQF can be seen in Fig. 3.5.

In order to test if a RFQ setup changes glass homogeneity when compared to simple liquid nitrogen plunging, one can use NMR and test the ^{1}H T1 / DNP buildup time (with preserved proton and exact radical concentrations), run EPR DEER distance measurements between two spin labels, and/or in the future analyze the ^{17}O NMR chemical shift. A better glass should exhibit more water matrix homogeneity due to minimal ice formation and less dissolved sample homogeneity due to reduced reorientation time into a more energetically favorable state, generally resulting in a longer NMR ^{1}H T1 and broader ^{31}P line. We plan to test the efficacy of this setup by running EPR DEER measurements in the future, however we were only able to run the control samples to date of
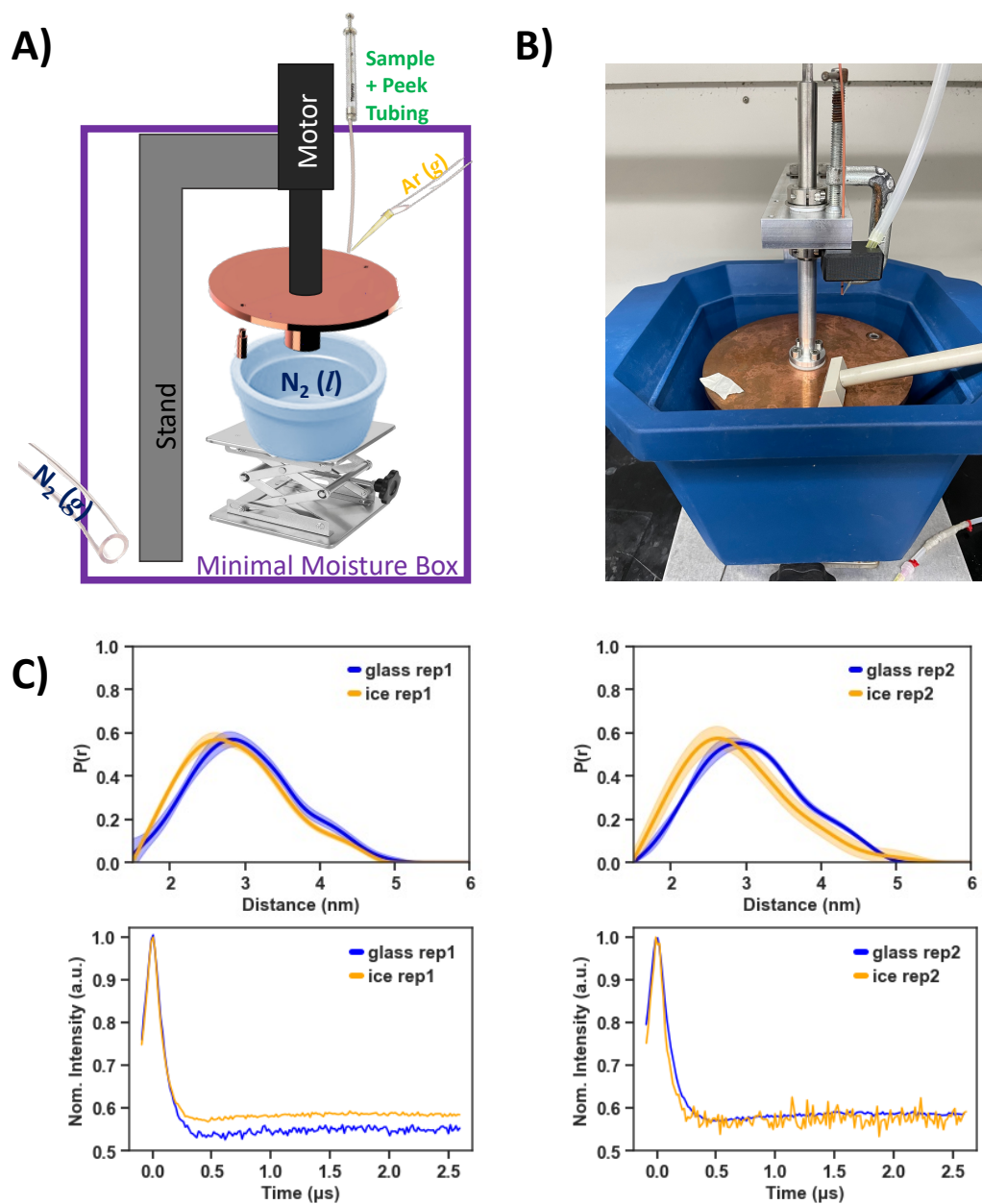
Figure 3.5: Rapid Freeze Quench (RFQ) Setup. A) Schematic of the RFQ. B) RFQ apparatus working prototype, glovebox not shown. C) EPR DEER Measurements on PY310 SLS2 monomer with 40 % glycerol by volume, two separate trials (left and right). The top plot is distance extraction and the bottom plot is the background corrected time domain data. Comparisons of the traditional glassing method (dipping EPR tube into liquid nitrogen) versus a frozen sample with visible ice crystals can be seen. RFQ apparatus design, testing, and EPR measurements big thanks to collaboration with Karen Tsay and Dr. Michael Vigers.

a plunge vitrified sample (labeled glass, visually clear/transparent) and a poorly glasses sample (labeled ice, visually white/opaque) with the help of Karen Tsay and Michael Vigers, as shown in Fig. 3.5. We ran these controls using a SLS2 pY310 tau monomer spin labeled at 300 and 314 in 40 volume % glycerol. While these results are preliminary, they show a clear trend that a poorly glassed sample (ice) can be differentiated from a satisfactorily glassed sample (glass), where the ice sample exhibits shorter distances between spin labels on the same protein. This provides supporting evidence that glassing procedure makes a significant difference on sample analysis which has previously been mostly overlooked and paves a path for further studies on glassing procedure.

Appendix A

Chapter 2 Appendix

A.1   Materials

Potassium phosphate monobasic (MW 136.09) and sodium phosphate monobasic (MW 119.98) were acquired from Fisher Scientific. Sodium phosphate tribasic (MW 163.94) was acquired from Acros Organics. Potassium pyrophosphate (MW 330.34) was acquired from Sigma-Aldrich. Adenosine 5'-diphosphate orthopotassium salt dihyrdate (MW 501.32) was acquired from Alfa Aesar. Adenosine 5'-triphosphate disodium salt hydrate (MW 551.14 anhydrous) was obtained from Sigma. Polyethylene glycol (MW 6K) was acquired from Fluka. Potassium chloride (MW 74.55), sodium chloride (MW 58.44), and ammonium chloride (MW 53.49) were acquired from Fisher Chemical. All samples prepared at room temperature. When not explicitly mentioned, the pH values were adjusted to 4.4 with HCl and NaOH to coincide with the native dissolved pH values found for monobasic orthophosphate. Every sample was dissolved in 600 to 700 uL of 90% Milli-Q water and 10% D_2O for locking purposes.

Adenosine 5'-diphosphate sodium salt (MW 427.20), sodium phosphate dibasic (MW 141.96), and coenzyme A sodium salt hydrate (MW 767.53) used for CEST were acquired

from Sigma-Aldrich. All samples prepared at room temperature. The pH values of the solutions were adjusted to 4.4 with HCl and NaOH in order to make them coincide with the native dissolved pH values found for orthophosphate. The real concentrations of the solutions were determined from the absolute integrations of the ^{31}P peaks in the 1D NMR spectra.

A.2   Instrumentation and Methods

Solution NMR relaxation experiments were performed on a Bruker Avance NEO 500 MHz spectrometer with a CryoProbe Prodigy BBO probe, using Wilmad-LabGlass 5 mm Thin Wall Precision NMR tubes. T_1 relaxation was measured with a standard inversion-recovery pulse sequence and T_2 relaxation was measured using a CPMG sequence. Delays varied depending on sample conditions (temperature, pH, and concentrations of salts and polyethlyene glycol (PEG)).

T_1 and T_2 delays were experimentally modulated such that the final two points for T_1 curves fully recovered and the final point for T_2 curves were less than 5% of the initial intensity. T_1 relaxation times were determined by employing the TopSpin 4.0.6 T1/T2 dynamics module. T_2 relaxation times were determined by MestReNova mono-exponential fitting. FWHM was determined by taking a 45ulse and employing TopSpin 4.0.6 PEAKW command. For each spectrum, a single scan was acquired with 40000 data points to cover a spectral window of 10000 Hz (49.4 ppm). An AU program was created to ensure temperature equalisation uniformity which included a ten minute temperature equilibration time and autoshimming was applied continuously before and throughout acquisition.

Diffusion ordered spectroscopy (DOSY) measurements were taken on a 300 MHz SWB Bruker spectrometer with a single gradient along the z-axis. DOSY is an exper-

imental that uses the Pulsed Field Gradient NMR (PFG-NMR) technique to extract diffusion coefficients for each NMR signal present in a sample. PFG-NMR measures particle diffusion by using a spin-echo pulse sequence in combination with a magnetic field gradient. As particles diffuse during the spin-echo sequence, they experience a slightly different field due to the gradient, and the spin-echo is unable to completely rephase the signal. This dephasing causes an attenuated signal intensity, which depend on the strength of the gradient, g, and the diffusion coefficient, D of the species as $\psi(g, D) = Exp(-Dg^2\gamma^2\delta^2(\Delta - \delta/3))$ where γ is the gyromagnetic ratio of the nucleus, δ is the width of the gradient pulse, and Δ is the time between gradient pulses [81]. By measuring this signal attenuation at several gradient strengths, one is able to fit the attenuation function to recover the diffusion coefficient of the associated species at each NMR line.

Measurements were taken at 293 K, 343 K, and again at 293 K after the sample had cooled. Capillaries were used at elevated temperatures to suppress convection. To confirm there were not convection effects, a convection-compensated pulse sequence was compared to the standard sequence for one sample at 293 K and 343 K. At 293 K, 32 scans with a 90ulse were acquired with 16384 data points to cover a spectral window of 6068 Hz (49.9 ppm) for gradient strength, and at 343 K, 64 scans with a 90ulse were acquired for each gradient strength with the same spectral conditions as above. At each temperature, data was taken using 16 linearly spaced gradient strengths such that the final spectrum had an intensity less than 5% of the first's. These decays were then fit in the TopSpin 4.0.6 T1/T2 relaxation module to extract a diffusion coefficient. The Stokes-Einstein relation was then used to convert this to a hydrodynamic diameter.

NMR chemical exchange saturation transfer (CEST) experiments were performed on a Bruker 500 MHz (11.7 T) NMR spectrometer equipped with a broadband observe (BBO) probe. The 90° pulse duration ranged from 10 to 12 us depending on ionic strength of the

solution. Saturation was performed by continuous wave (cw) irradiation of 5 s duration with field strengths of 1.16 μT to 8.69 μT (corresponding to nutation frequencies of 20 Hz to 150 Hz). The recycling delay was set to 5 s. Following cw irradiation, a 90° pulse is used for spectral readout. The temperature dependence of CEST measurements were taken with the irradiation power of 150 Hz at 298 K, 313 K, 323 K, 333 K, 343 K and 353 K, and the irradiation power dependence of CEST measurements were taken at 298 K with nutation frequencies of 20 Hz, 30 Hz, 50 Hz, 100Hz and 150 Hz. At each measurement, 8 scans with a 90ulse were acquired. The scanned frequency ranged from -4000 Hz to 4000 Hz with a step size of 200 Hz.

Control experiments were performed to rule out the influence of temperature gradients or convection on the results. Relaxation rates were found to be the same in samples containing capillaries (used to curb convection, if it exists), and chemical shift imaging was used to verify that the linewidths were the same in different z-positions in the sample.

For Cryo-TEM, phosphate solutions were prepared at room temperature and heated for at least 48 hours at 343 K before vitrification. Solutions were vitrified using an FEI Vitrobot Mark IV for vitrification in liquid ethane. 1.2 µL of sample was deposited on a lacey carbon support film on 200 mesh copper grid, blotted for one second, and immediately vitrified. The cryo-TEM was performed using Gatan 626 Cryo transfer holder with liquid nitrogen by ThermoFisher Talos G2 200X TEM/STEM at 200 kV with a Ceta II CMOS camera for bright field imaging.

Microscopy analysis was conducted in Fiji Version 1.0. Images were first processed with a FFT bandpass filter, in order to smooth long-length scale variations in intensity to to variations in camera pixel sensitivity, and to attenuate structures at small length scales that originate from pixel noise. Cutoffs for these filtering were varied, and found not to qualitatively affect the relative results. After filtering, pixels were autoscaled and saturated, before thresholding on the top 2-4 % of pixel intensity. The threshold was

varied in this range to provide error bars for histogram results. After thresholding, the Close function was used to fill small regions of white pixels fully surrounded by black pixels. The Analyze Particles function was then used to select particles with an area of $200 - 2000$ pixels^2 and a circularity criteria of $0.6 - 1$, where circularity is defined as $4\pi * \frac{area}{perimeter^2}$. Results were then extracted and converted into area in nanometers for comparison between samples.

MD simulation workflow and systems simulated: Systems are constructed using GRO-MACS 2016.1 [168, 169]. We perform the simulations using the OpenMM simulation engine [170]. Electrostatic interactions are computed using particle-mesh Ewald. Lennard-Jones nonbonded interactions are cut off at 10 Å. Hydrogen bonds are constrained with SHAKE [171] and water is kept rigid with SETTLE [172]. We use Langevin dynamics with an integration timestep of 2 fs and a friction coefficient of 0.1 ps^{-1}. We first perform a local energy minimization, followed by a 100-ps NVT equilibration. For the concentrated systems, we then perform a 25-ns NPT equilibration using a Monte Carlo (MC) barostat with 200 fs between MC moves and then perform a 175-ns NPT production, again using the MC barostat with the same conditions, saving configurations every 100 ps. For the dilute systems, we perform a 100-ps NPT equilibration using the MC barostat with the same conditions, followed by a 1000-ns NPT production, again using the MC barostat with the same conditions. The cluster size distributions, radial distribution functions, and coordination numbers are computed from the production simulations.

$N_{HPO_4^{2-}}$	$N_{H_2PO4^-}$	N_{Na^+}	N_{H_2O}	Temperatures simulated [K]
100	0	200	4759	293, 343
0	100	100	4852	293, 343
50	50	150	4801	293, 343
3	0	6	2149	293, 303, 313, 323, 333, 343
0	3	3	2148	293, 303, 313, 323, 333, 343

Table A.1: Systems simulated using molecular dynamics.
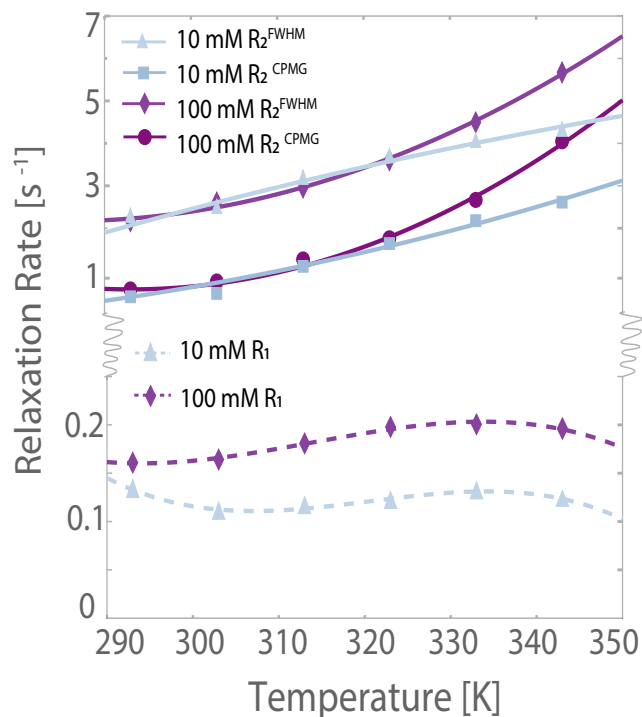
A.3   Figures

Figure A.1: R_2 as extracted from a CPMG pulse sequence and from FWHM for 10 mM and 100 mM potassium orthophosphate monobasic pH 4.5 as a function of temperature, showing monotonic increase in R_2 in each case. Solid lines are quadratic fits to data to guide the eye. R_1 for 10 mM, 100 mM, potassium orthophosphate monobasic pH 4.5 as a function of temperature showing the same curve shapes as a function of concentration. Solid lines are cubic fits to data to guide the eye.
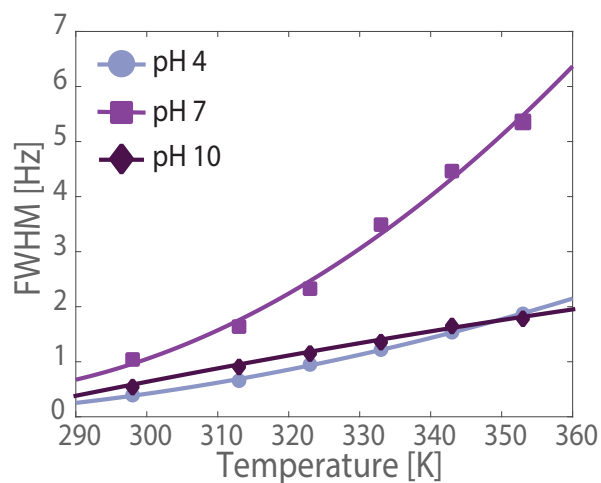
Figure A.2: FWHM of sodium phosphate dibasic solutions at pH 4, pH 7 and pH 10 showing line broadening. Solid lines are quadratic fits to data to guide the eye.
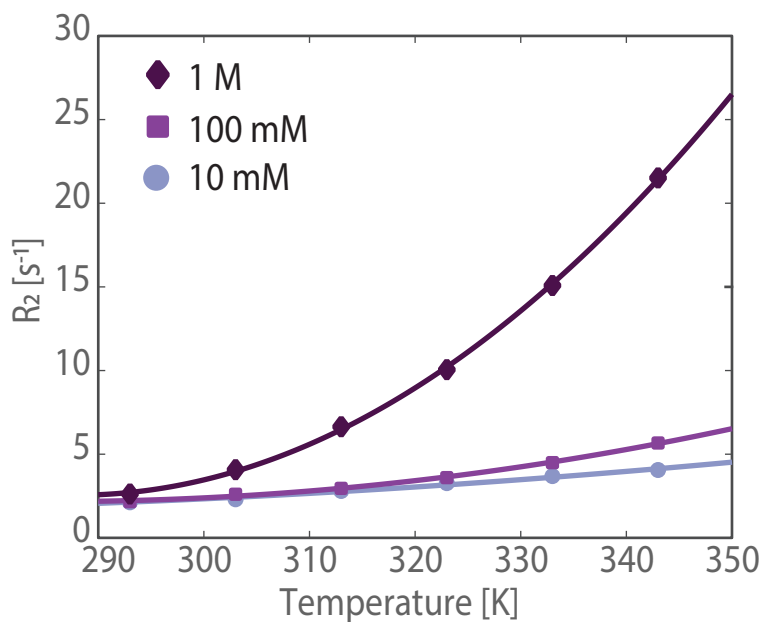
Figure A.3: R_2 rates calculated from FWHM for potassium phosphate solutions at pH 4.5 over a range of phosphate concentrations showing line broadening across a range of concentrations. Solid lines are quadratic fits to data to guide the eye.
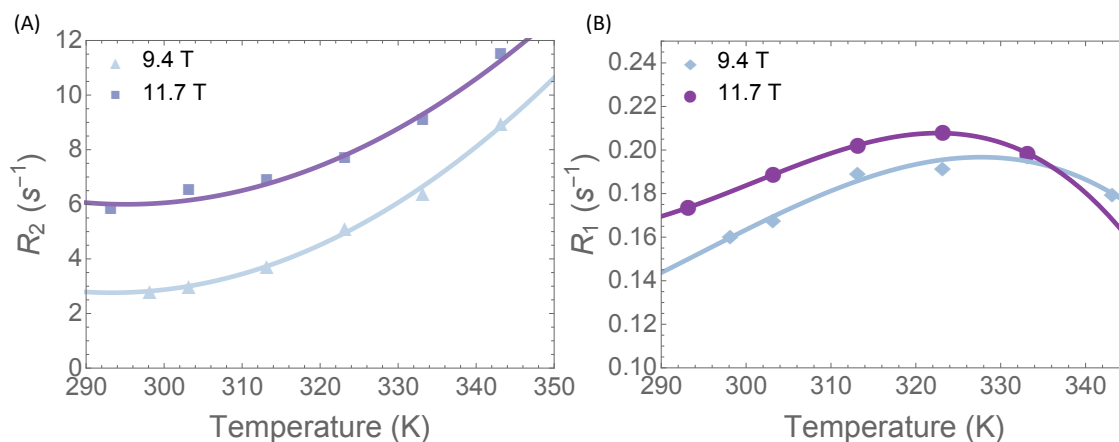
Figure A.4: Relaxation rates for 10 mM potassium phosphate at pH 4.5 from two different spectrometer strengths- 9.4 T ($\omega_0(^{31}P)$ =162 MHz) and 11.7 T ($\omega_0(^{31}P)$=202 MHz). (A) R_2 as calculated from FWHM shows increase with temperature at both spectrometer strengths.Solid lines are quadratic fits to data to guide the eye. (B) R_1 rate minimums shift to higher temperatures at greater field strength.Solid lines are third order polynomial fits to data to guide the eye.
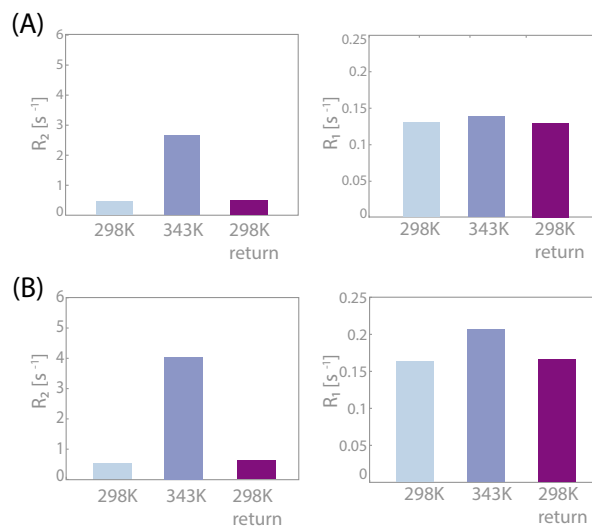

Figure A.5: Relaxation Rates for 10 mM and 100 mM sodium phosphate show reversibility after heating to 343K and cooling. (A) Relaxation rates for 10 mM sodium phosphate, (B) Relaxation rates for 100 mM dosium phosphate
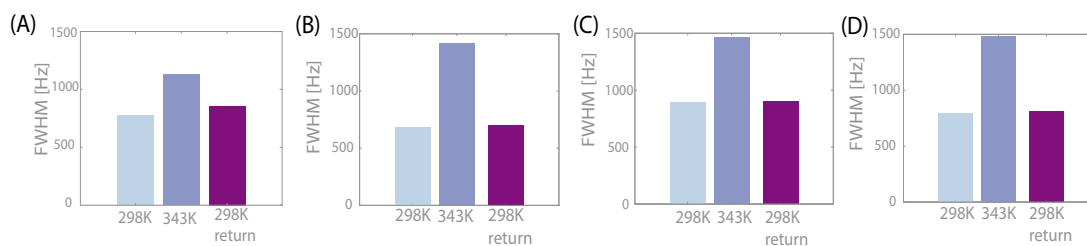
Figure A.6: ^{31}P CEST dip widths showing Reversibility at 298 K, 353 K and cooling back to 298 K. (A) 50 mM orthophosphate, (B) 100 mM orthophosphate, (C) 200 mM orthophosphate, (D) 300 mM orthophosphate.
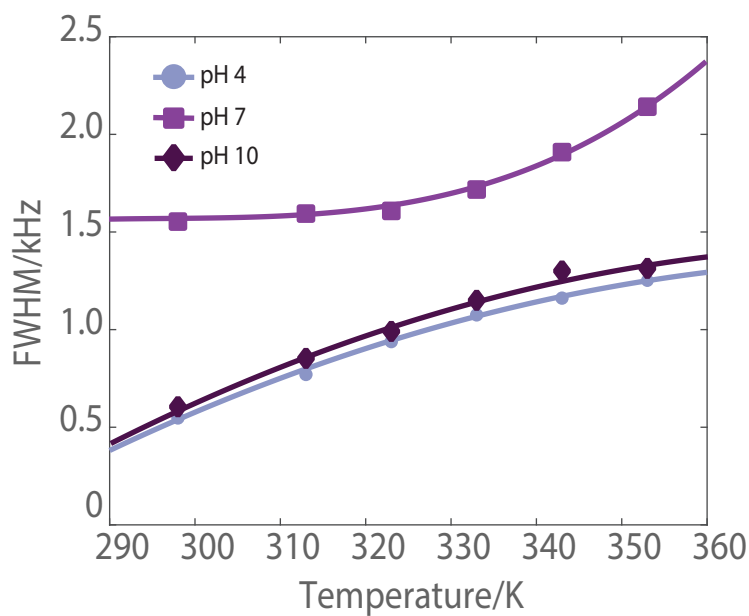

Figure A.7: ^{31}P CEST dip widths at half height of sodium phosphate dibasic solutions at pH 4, pH 7 and pH 10 showing line broadening as a function of temperature. Solid lines are quadratic fits to data to guide the eye.
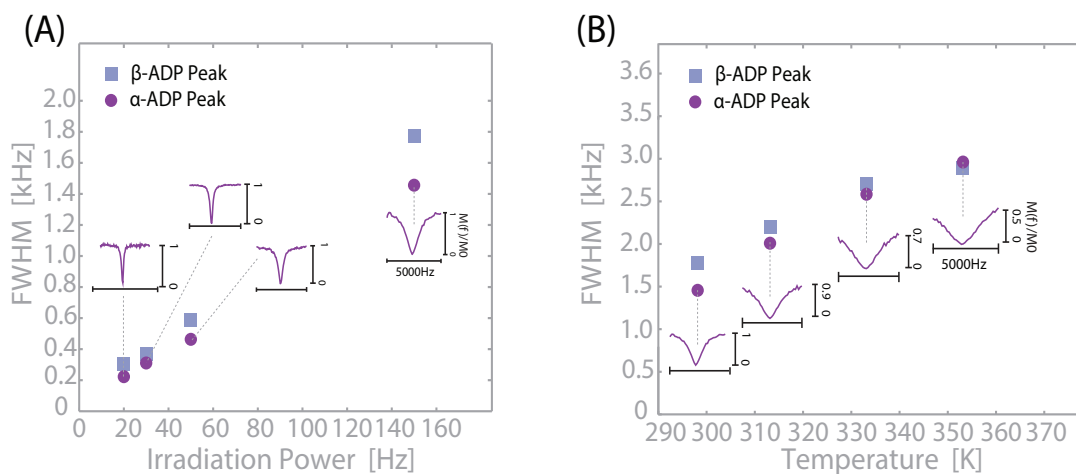
Figure A.8: ^{31}P CEST results for both phosphates in 100 mM ADP in D$_2$O at pH 3.9. (A) CEST dip width at half height as a function of CEST irradiation power of 20 Hz, 30 Hz, 50 Hz and 150 Hz at T=298.15 K, (B) CEST dip width at half height as a function of temperature of 298 K, 313 K, 333 K, 353 K.
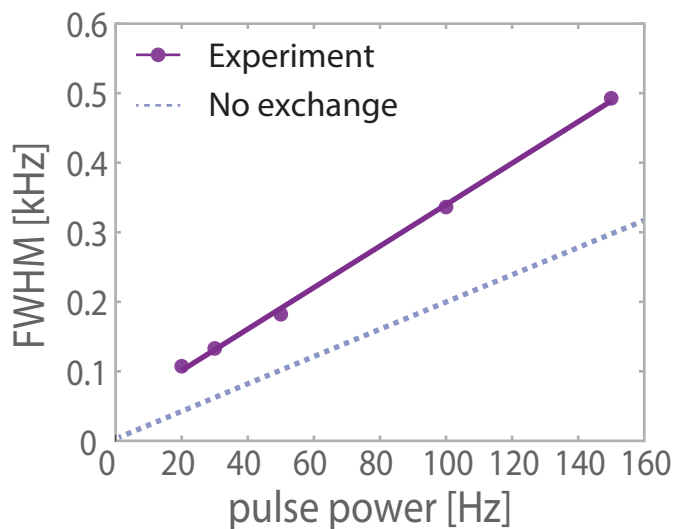

Figure A.9: ^{31}P CEST dip width at half height for 100 mM sodium phosphate as a function of CEST irradiation power of 20 Hz, 30Hz, 50 Hz, 100 Hz, and 150 Hz measured at 298 K. In the absence of exchange, one expects the width of the dip in the CEST spectrum to be approximately a factor two larger than the rf saturation power (expressed in Hz). However, the dip width ranging from 100 Hz to 500 Hz under exchange is over a factor three larger than the rf saturation power (expressed in Hz). The Solid lines are linear fits to guide the eye
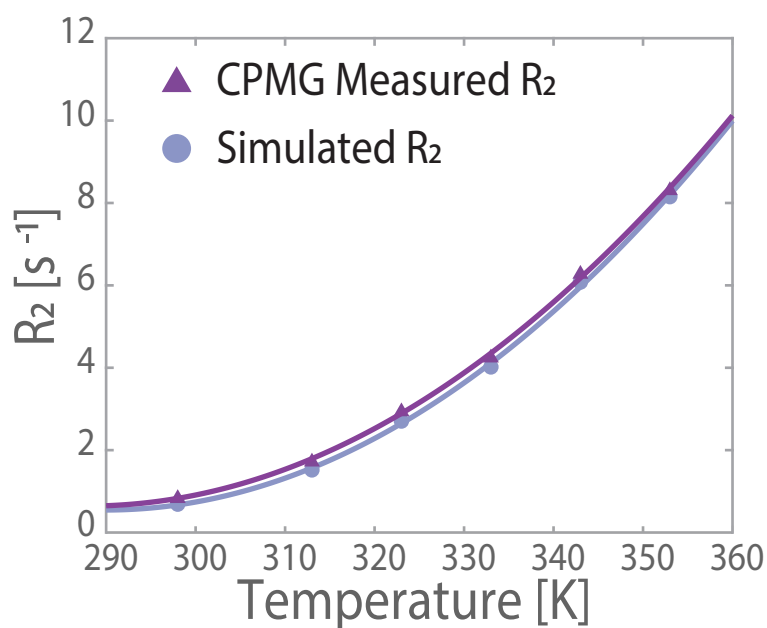
73

Figure A.10: The experimental and simulated ^{31}P R_2 rates for the 100 mM orthophosphate sample shown in Fig. 2.2B&C. Parameters used for this simulation were the same as used for the CEST simulations in Fig. 2.2B. Additional information on the modeling and physical interpretation is below.
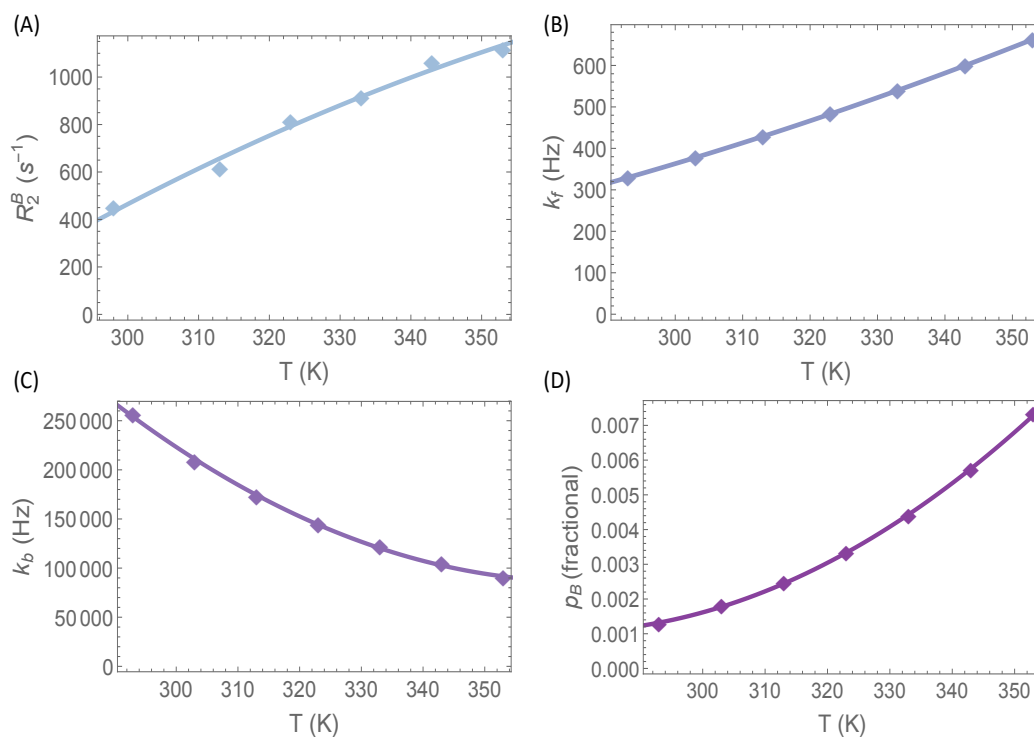
Figure A.11: Temperature dependence of R_2^B, kinetic parameters, and assembly population used for the simulated R_2 and CEST data shown in Fig. A10 and 2.2B, respectively. Solid lines are quadratic fits to data to guide the eye. (A) The assembly relaxation rate R_2^B increases from 450 Hz to 1100 Hz between 298 K and 353 K. (B) The phosphate monomer to assembly rate (k_f) increases from 350 Hz to 600 Hz between 293 and 353 K. (C) The assembly to monomer rate (k_b) decreases from 250,000 Hz to 100,000 Hz between 293 and 353 K. (D) The fractional assembly population (p_B) increases from 0.0013 to 0.0073 between 293 K and 353 K.

75

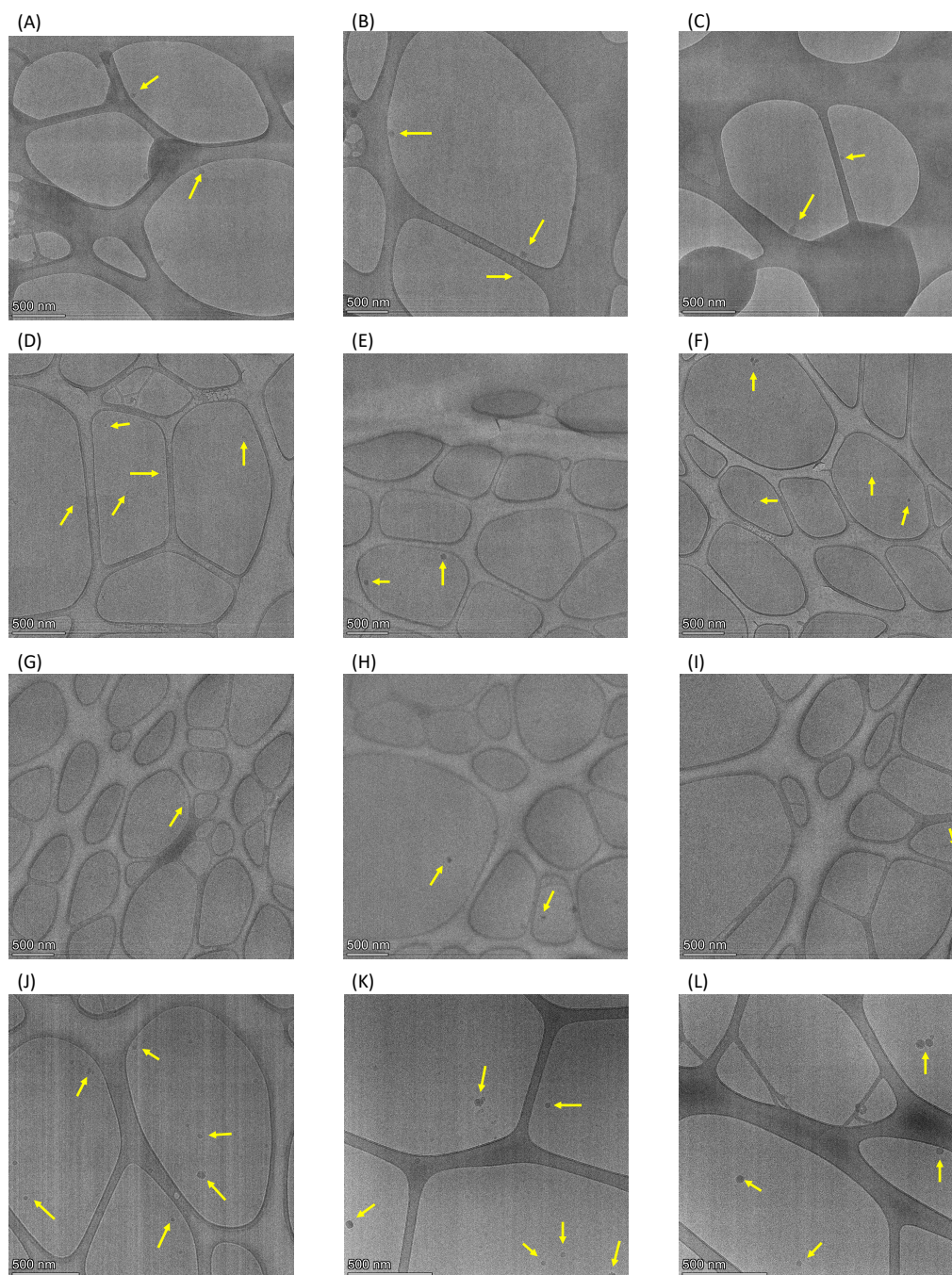Figure A.12: Cryo-TEM micrographs from (A)-(C) 100 mM sodium ADP sample unheated, (D)-(F) 100 mM sodium ADP heated to 343 K, (G)-(I) 500 mM KCl heated to 343 K, and (J)-(L) 100 mM potassium ADP heated to 343 K. Yellow arrows indicate features in the size range of assemblies, although ice artifacts can appear at similar sizes. Samples in (A)-(I) are the samples used for the quantitative particle analysis.
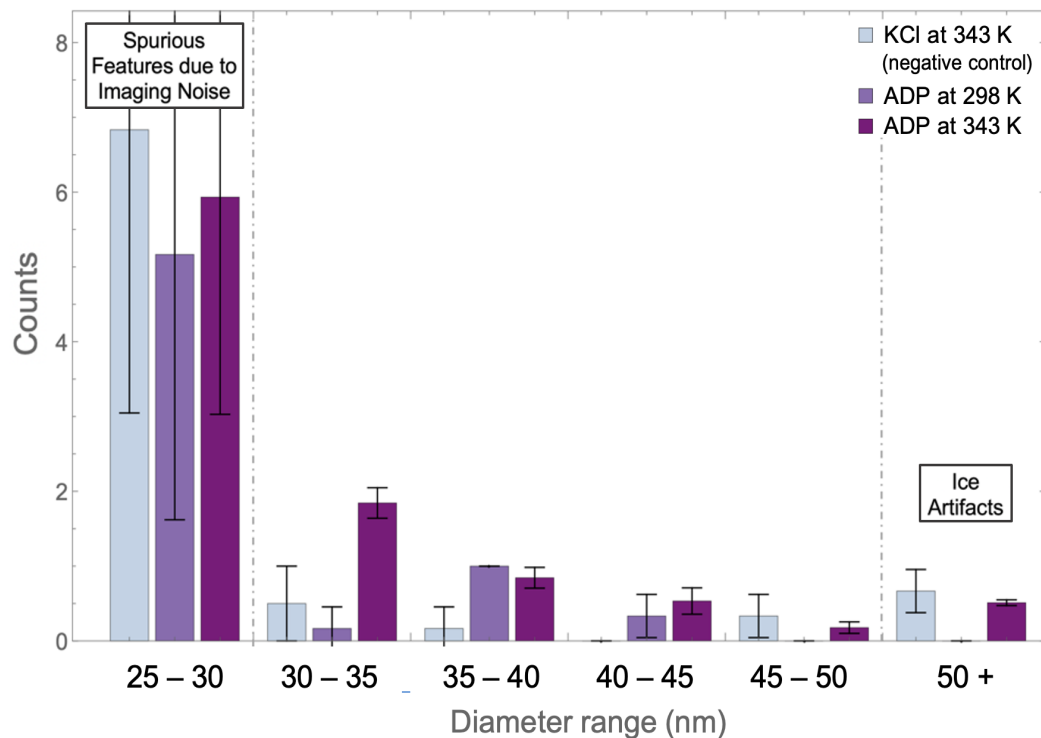
Figure A.13: Histogram of diameters for features detected per micrograph in selection of representative micrographs for sodium ADP at 298 K, sodium ADP heated at 343 K, and potassium chloride heated at 343 K. Only micrographs taken at the same magnification were compared, since the micrograph noise is primarily on pixel level. There were two, nine, and two micrographs, respectively, thus analyzed in the workflow described in Appendix A. These results show a larger population of species in the two ADP samples, with the most in the heated ADP samples, except at the smallest and largest sizes, which can thus be attributed to erroneous features from the processing of the image analysis and ice artifacts, respectively, given that these are the only populations seen in the potassium chloride samples.
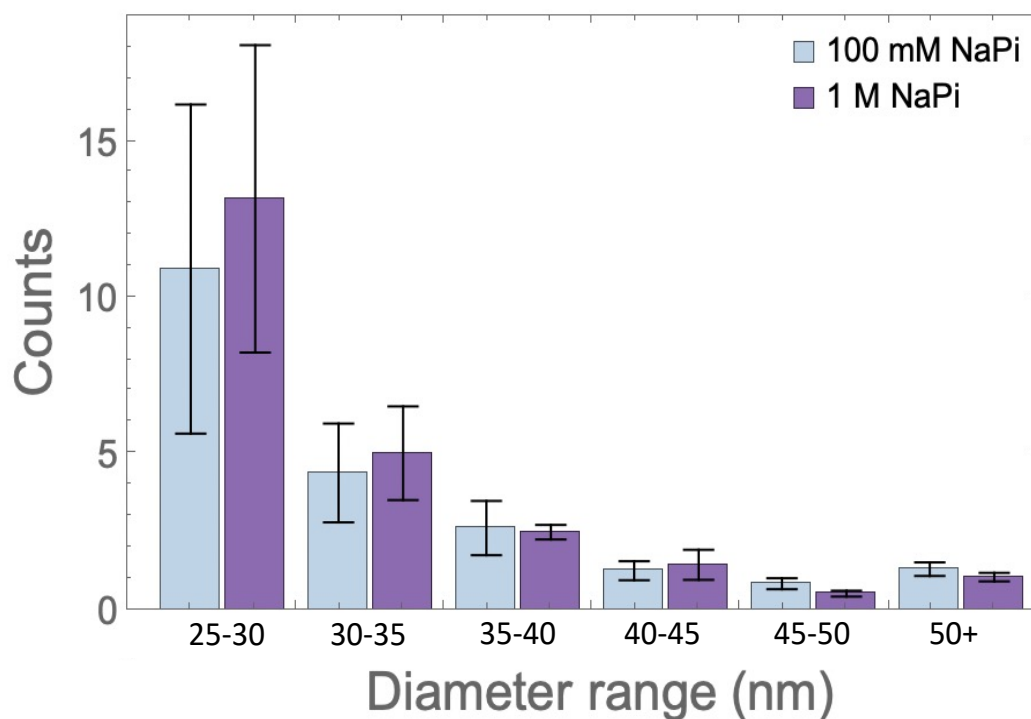
Figure A.14: Histogram of diameters for features detected per micrograph in selection of representative micrographs for sodium monophosphate at 100 mM and 1 M heated to 343 K before vitrification. Only micrographs taken at the same magnification were compared, since the micrograph noise is primarily on pixel level. Each sample incorporates data from 20 micrographs analyzed with the workflow described in Appendix A. These results show that the size distribution of features is similar at both concentrations, which is consistent with equilibrium structures.

Figure A.15: Radial distribution functions (RDFs) and coordination numbers for water around phosphate ions, phosphate ions with each other, and Na^+ around phosphate ions. RDFs (A, B, D, E, G, H) are computed to a maximum distance of 20 Å with a bin size of 0.2 Å. The distances r are between (A, B) water oxygen 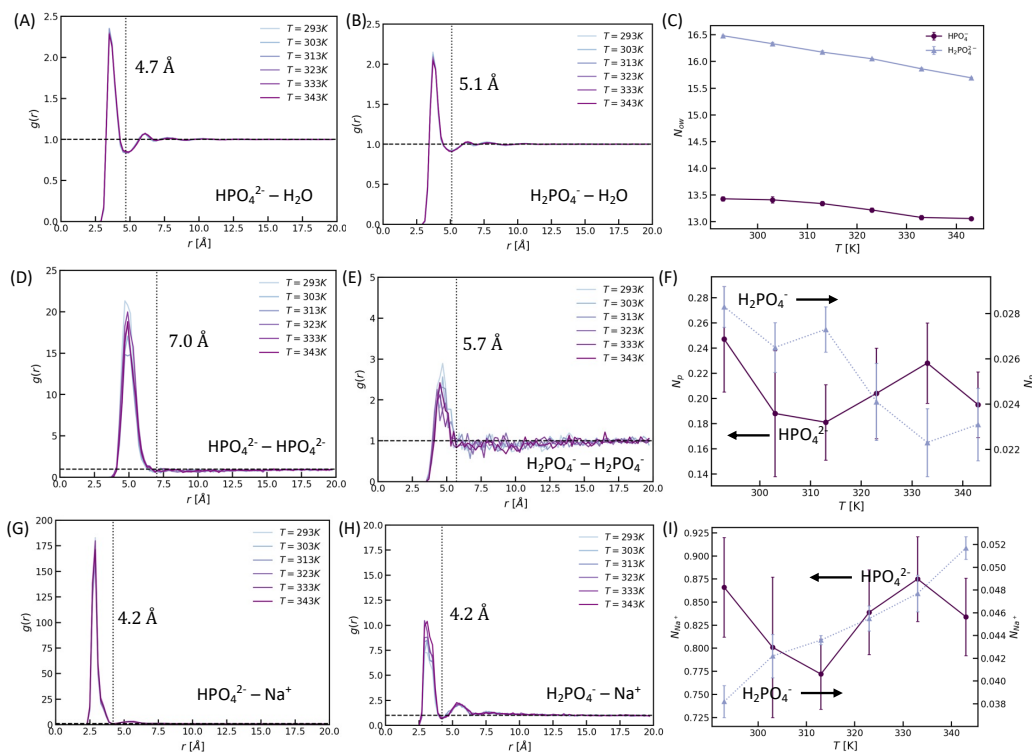atoms and phosphate phosphorous atoms, (D, E) phosphate phosphorous atoms with each other, and (G, H) sodium atoms and phosphate phosphorous atoms. The water-phosphate coordination number (C) is the average number of water oxygen atoms within 4.7 Å (HPO_4^{2-}) or 5.1 Å ($H_2PO_4^-$) of a phosphate phosphorous atom. The phosphate-phosphate coordination number (F) is the average number of phosphorous atoms within 7.0 Å (HPO_4^{2-}) or 5.7 Å ($H_2PO_4^-$) of a phosphorous atom. The sodium-phosphate coordination number (I) is the average number of sodium atoms within 4.2 Å of a phosphate phosphorous atom. The coordination number cutoffs are determined from the approximate location of the first minimum of the corresponding RDF (dotted lines, labeled with the exact cutoff). Error bars in (C), (F), and (I) are twice the standard error of the coordination numbers computed for each 200-ns block in the 1000-ns production simulation.
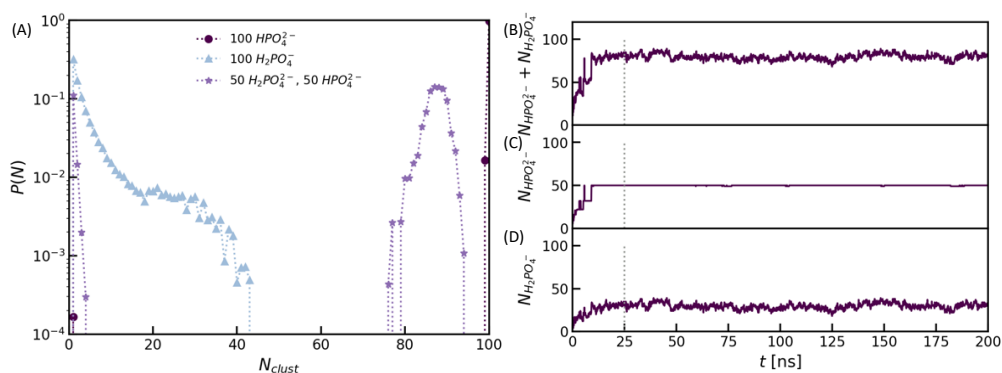
Figure A.16: (A) Cluster size distributions for the same systems as in Fig. 2.4C of the main text, but at 293 K. (B) Trajectory of the combined number of phosphate ions, both HPO_4^{2-} and $H_2PO_4^-$, in the largest cluster of the simulation of the mixed system at 343 K during the NPT equilibration and NPT production (separated by the dotted line). (C) Trajectory of the number of HPO_4^{2-} ions in that largest cluster. This trajectory is virtually constant at $N = 50$, the total number of HPO_4^{2-} ions in the box, during the entire production run, indicating that all HPO_4^{2-} ions in the box are in this large cluster. (D) Trajectory of the number of $H_2PO_4^-$ ions in that same cluster. Two phosphate ions are considered clustered if their phosphorous atoms are within 7.0 Å of each other. The 7.0 Å cutoff is chosen from the approximate location of the first minimum in the phosphate-phosphate RDF (Fig. B13C).
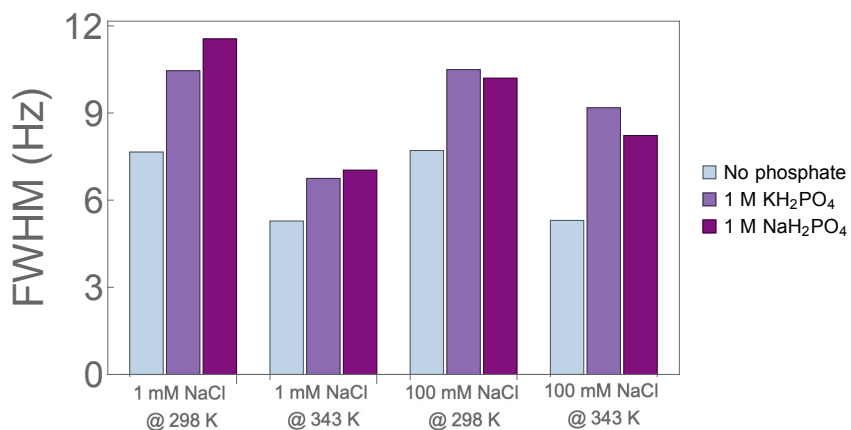
Figure A.17: Experimental ^{23}Na linewidth data for 1 mM and 100 mM NaCl in the absence of phosphates, and with 1 M KH_2PO_4 and 1 M NaH_2PO_4 at 298 K and 343 K. All solutions were adjusted to pH 4.1 with HCl. ^{23}Na linewidths are broader in the presence of phosphates at both temperatures and concentrations, indicating that sodium is incorporated into the assemblies.
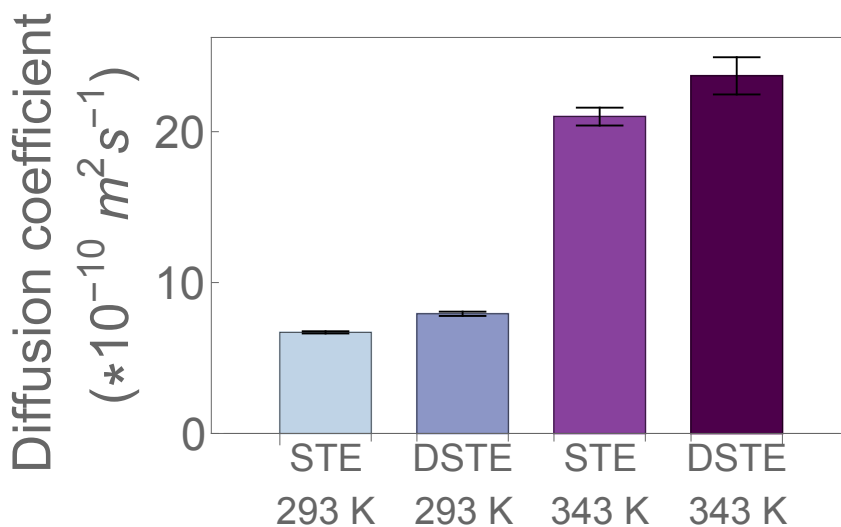
Figure A.18: Diffusion coefficients extracted from ^{31}P DOSY experiments for 1 M potassium phosphate at pH 4.2 using a stimulated echo (STE) and convection-compensated double stimulated echo (DSTE) sequence. Diffusion coefficients were found to be comparible at both 293 K and 343 K, indicating that the observed increased in diffusion coefficient with temperature is not a convection-based effect.
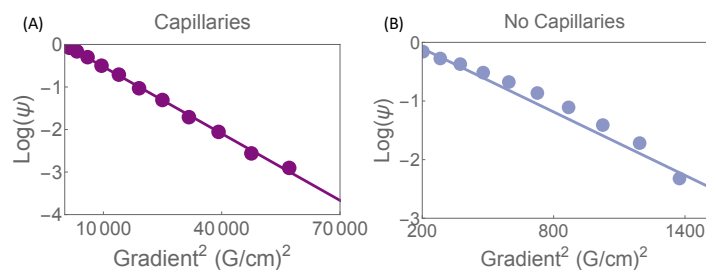
Figure A.19: ^{31}P DOSY fits of Log(ψ) vs gradient strength squared for a 1 M potassium phosphate sample in the presence (A) and absence (B) of capillaries at 343 K, where ψ is signal attenuation. Note that in the absence of capillaries, the relationship between Log(ψ) and gradient squared is non-linear due to convection-based dephasing effects, and that the gradient values are much lower because of the increased rate of particle motion. Capillaries were thus used for all high temperature samples.
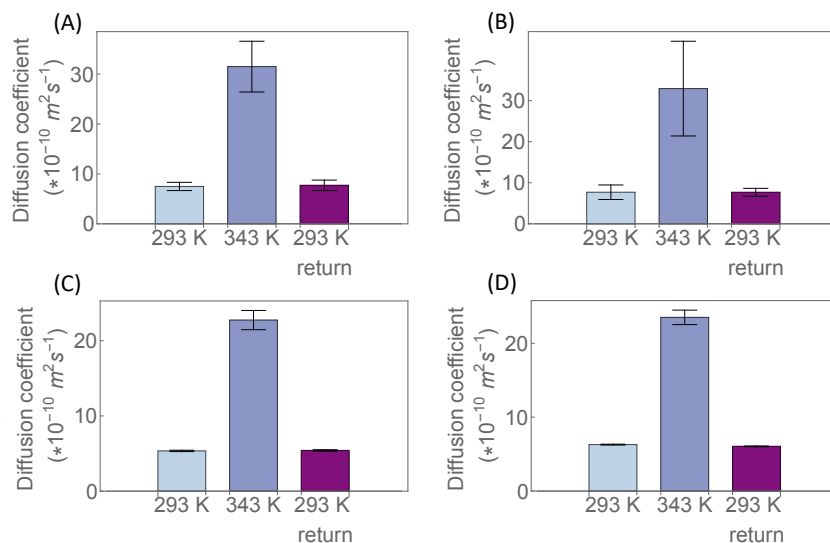
Figure A.20: Diffusion coefficients extracted from ^{31}P DOSY experiments. (A) 100 mM sodium phosphate at pH 4.2, (B) 100 mM potassium phosphate at pH 4.0, (C) 1 M sodium phosphate at pH 4.2, (d) 1 M potassium phosphate at pH 4.1.
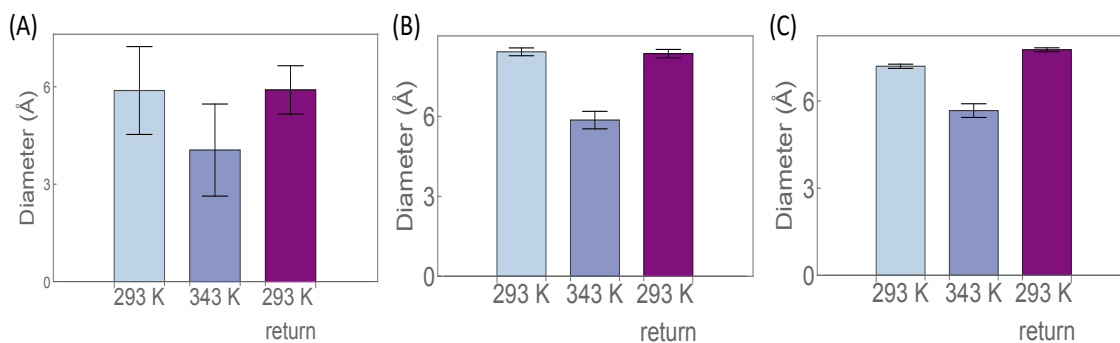
Figure A.21: Hydrodynamic diameters found by the Stokes-Einstein relaxation from diffusion coefficients in S5. (A) 100 mM potassium phosphate, (B) 1 M sodium phosphate, (C) 1 M potassium phosphate.
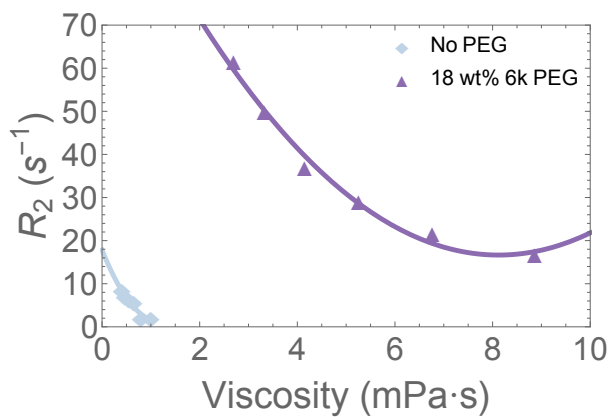
Figure A.22: R_2 relaxation rate as extracted from FWHM for 100 mM potassium phosphate at pH 4.5 in the absence of PEG and for a 18 wt% PEG solution as a function of viscosity [173], showing that viscosity alone cannot explain the effect of PEG on relaxation rates. Solid lines are quadratic fits to data to guide the eye.

Appendix B

Chapter 3 Appendix

B.1 Materials

Crystalline hydroxyapatite $HCa_5O_{13}P_3$ nanopowder < 200 nm particle size (677418; MW 502.31 g/mol) was commercially obtained from Sigma Aldrich and used without further processing. Amorphous calcium phosphate was synthesized by preparing a 500 mL final volume solution and subsequent lyophilization, with similar synthetic procedures to literature[174]. A 475 mL solution of 2.1 mM $NaPO_4$ (prepared by mixing 100 mM Na_3PO_4 (Acros Organics 389810010; MW 163.94 g/mol) and 100 mM H_3PO_4 (Fisher 85 % o-Phosphoric Acid A242; FW 97.99 g/mol) for a final concentration of 100 mM and pH 7.7) and 263 mM KCl (from dry Sigma-Aldrich salt, P3911; MW 74.55 g/mol) was prepared with pH adjusted to 7.6 by adding 0.2 M NaOH (EMD, SX0590; FW 40.0 g/mol). 25 mL of 100 mM $CaCl_2$ dihydrate (Fisher Scientific $CaCl_2$*$2H_2O$, C79; FW 147.01 g/mol) was subsequently added and the sample was vortex mixed for a final volume of 500 mL (5 mM $CaCl_2$, 2 mM $NaPO_4$, and 250 mM KCl). The solution was left for 5 minutes to allow for prenucleation cluster formation and initiation of initial binding events. 15 mL of 0.2 M NaOH was then added to increase pH of solution and

crash out ACP. A Buchner funnel under vacuum with filter paper was used to capture precipitate and washed with milliQ water. The resulting ACP paste was removed from the filter paper and lyophilized for 72 hours to form dried powder and stored at -4 °C. HAp and ACP powder were analyzed by X-Ray diffraction to ensure phase identification in Fig. B2. Adenosine 5'-triphosphate disodium salt hydrate (A2382; Anhydrous Basis FW 551.14 g/mol) was commercially obtained from Sigma-Aldrich and used without further processing (see Fig. B4 for crystallinity). Various ATP powders were analyzed by solid state NMR to ensure phase identification in Fig. B4. All powder room temperature samples were finely ground and packed into a 3.2 mm thin walled ZrO_2 rotor.

For vitrification, all samples utilizing glycerol glassing agent (Aldrich, 447498) were prepared with 6:3:1 volume parts glycerol-d8, D_2O, H_2O with a final concentration of 10 mM (or 6.67 mM for mSBF) AMUPol (Cortechnet, C010P005) (DNP juice). HAp was prepared by first dissolving the aforementioned purchased powder in D_2O and H_2O, correcting the pH to 7.13 with 1 M HCl, and aggressive stirring and sonication for one hour. AMUPol was then dissolved (sample added to pre-measured AMUPoL), glycerol-d8 was added, and the sample was vitrified with liquid nitrogen (LN_2) for a final approximate concentration of 40 mM HAp in DNP juice. Amorphous calcium phosphate was prepared for vitrification by immediate synthesis via mixing stocks for an interim solution concentration of 20 mM NaH_2PO_4, 250 mM KCl, and 50 mM $CaCl_2$ (same suppliers used to purify powdered ACP) in D_2O and H_2O at pH 7. AMUPol was then immediately dissolved (sample added to pre-measured AMUPoL), glycerol-d8 added, and LN_2 vitrified as quickly as possible (on the scale of minutes). We must note that ACP formed at lower calcium and phosphate concentrations (5 and 2 mM respectively in interim solution mixture) is partially dissolved by glycerol, verified by DLS, solution NMR, and ssNMR not shown in this paper. ATP preparation is described in the main paper Fig. $3.3C$ caption. DMSO-d6 stock was purchased from Cambridge Isotope Laboratories, Inc., DLM-10.

We must note that DMSO samples must be vitrified immediately otherwise there is a high affinity for phase separation and ATP aggregation, verified by DLS (not shown). Monophosphate control sample was prepared from the same phosphate stock preparation procedure as that used for ACP synthesis, with an interim solution concentration of 100 mM NaH_2PO_4 pH 7 in H_2O. This interim stock was then diluted with 3 parts D_2O to one part H_2O, for a concentration of 25 mM. AMUPoL was then dissolved via vortex mixing (sample added to pre-measured AMUPoL), and 6 parts by volume glycerol-d8 was added, for a final concentration of 2 mM NaH_2PO_4 in DNP juice. Solution NMR and dynamic light scattering were preformed on these dissolved/suspended samples before the addition of AMUPol and glycerol-d8 to confirm size and phase state (Fig. B3). All vitrified samples were packed in a 3.2 mm regular walled sapphire rotor using a Teflon or silicon plug to prevent leakage and plunged in liquid nitrogen.

Studies completed by Epasto, et al.[152], inspired by Oyane et al.[150, 151] were replicated and modified for our procedure. The modified simulated body fluid (mSBF) sample was prepared by weighing each salt onto a piece of weigh paper before being transferred into a 10 mL vial, all at room temperature. The salts were each measured into this single shared container (including HEPES), with all salt weights listed in Table SS1 below, however $CaCl_2$ was weighed last and stored separately for subsequent timed addition. Prior to adding the calcium, 3.95 mL of H_2O, 500 μL of 0.2 M NaOH, and 500 μL of D_2O were added, in that order. The solution was vortex mixed for approximately 10 seconds after adding each aforementioned solutions. $CaCl_2$ was then added to the mSBF (increasing the pH), and the solution was vortex mixed again. The solution was pH corrected with approximately 200-300 μL of 1 M NaOH to pH 7.41, and was typically corrected from an initial pH of 7.2-7.3. Milli-Q H_2O was added to correct the complete solution volume to 5 mL, and the sample was vortex mixed a final time. Finally, 500 μL of mSBF was transferred to a labeled and washed NMR tube, and placed into the

	UCSB (g)	Manufacturer	Mol. Wt. (g/mol)
NaCl	0.027	Sigma	58.44
$NaHCO_3$	0.00252	Sigma	84.01
Na_2CO_3	0.00213	Fisher	105.99
KCl	0.001125	Fisher	74.55
K_2HPO_4	0.00115	Fisher	174.18
$MgCl_2{\times}6H_2O$	0.001555	Fisher	203.3
HEPES	0.08946	Sigma	238.3
Na_2SO_4	0.00176	EMD	110.99
Milli-Q H_2O (liquid)	4 mL		
0.2 M NaOH (liquid)	0.5 mL	Fisher	39.997
D_2O (liquid)	0.5 mL		
$CaCl_2$	0.00036	Fisher	110.98

Table S1: The respective amounts of material by mass (if dry) or by volume (if stock solution) for each component of mSBF in the order they were added starting from the top. The rightmost columns provide the manufacturer information for each chemical.

solution NMR spectrometer at 25° C, with an interim solution total concentration of 1.32 mM and 0.6487 mM phosphate and calcium respectively. After four hours once the solution ^{31}P signal was sufficiently and stably splitting into two peaks, we took 20 μL of this mSBF stock solution (in 90 % H_2O and 10 D_2O % by volume) and added it to premeasured 23.08 mM AMUPol (6.67 mM final concentration) already dissolved in 52 μL of D_2O. 108 μL of glycerol-d8 was then added and the sample was vortex mixed, packed into a 3.2 mm sapphire rotor, and plunged in liquid nitrogen for ssNMR analysis. The final concentrations in this vitrified sample were 0.147 mM phosphate and 0.072 mM calcium. A 1D ^1H to ^{31}P CP solid state spectra was taken the day of, and then the sample was stored in a -80° C freezer for two years until analyzed again and spin counting experiments were performed.

B.2   Instrumentation and Methods

NMR Experiments

Solid state NMR experiments were performed on a Bruker ASCEND DNP-NMR spectrometer (9.4T T) equipped with a 25 W gyrotron microwave source (operating at 263 GHz microwave frequency) and employing a 3.2 mm MAS DNP-NMR triple resonance broadband X/Y/H probe (Bruker) with a 50 ohm resistor on Y channel to complete the circuit. Fig. B1 on the following pages summarizes the experimental design for spin counting experiments. T_2 values were measured by the Carr-Purcell-Meibom-Gill (CPMG) sequence while employing continuous ^{1}H decoupling. Under DNP conditions, all experiments were completed using cross polarization from ^{1}H to ^{31}P with sufficient contact time. At room temperature, both direct ^{31}P and cross polarization rendered the same results for all powdered samples.

Solution NMR relaxation experiments were performed on a Bruker Avance NEO 500 MHz spectrometer with a CryoProbe Prodigy BBO probe, using Wilmad-LabGlass 5 mm Thin Wall Precision NMR tubes. 1D experiments were completed with 64 scans, a relaxation delay of 5 s, a 45° ^{31}P pulse of 6 us at 40 W, and an acquisition time of 1-2 s. T_2 values were measured by CPMG and T_1 by inversion recovery, with a relaxation delay of 10 s and 90° ^{31}P pulse of 12 us at 40 W, and an acquisition time of 1 s..

Data Processing

All NMR integrals taken for T_2 and spin counting analysis were processed using a custom Python Jupyter Notebook code. Leftshift, line broadening, baseline correction, and custom integrals were applied for all FID's of a given data set. MQCO profiles were very susceptible to phasing and leftshift accuracy. Each FID was analyzed separately to

ensure data was cohesive.

Scattering Experiments

X-ray scattering experiments were completed on a comercial Panalytical Empyrean Powder Diffractometer. Dynamic light scattering was conducted with a BI-200SM Goniometer System with a TurboCorr correlator (Brookhaven Instruments) and a Cobolt Samba 500 mW laser at 532 nm (HÜBNER Photonics). DLS measurements were carried out at a 90° scattering angle with 200 correlation channels ranging from 100 ns to 100 ms and sampling rates of 100 ns, 5 ms, and 50 ms, depending on the channel delay. All samples were filtered through a 0.2 μm pore size filter to remove dust contaminants.

EPR

DEER signal was collected for 12-24 hours until an optimal SNR was achieved. All DEER time traces were transformed into distance distributions using DeerLab software package for Python. The time traces were phase corrected and truncated by 300 ns to remove possible "2+1"-artifact. One-step analysis was done using the DeerLab fit function with the following models: ex-4deer model with t1, t2, and pulse length set to experiment parameters, bg strexp model with the stretch parameter freeze to 3 (for soluble protein) and bg homfractal model with the fractal dimensionality set to fit between 1 to 3 (for fibril samples), and dipolar model using Tikhonov regularization. The uncertainty analysis was done using bootstrapping method with 100 samples. The time domain fitting results are presented both as fitting to the primary data and the distance distribution fits are presented with 95 % confidence intervals. Samples were corrected using spectra collected of the singly labeled species (SLS1/2-314C) to account for the shift in geometrical dimensions. The DEER experiments were performed with a pulsed

Q-band Bruker E580 Elexsys spectrometer, equipped with a Bruker QT-II resonator and a 300 W TWT amplifier with an output power of 20 mW for the recorded data (Applied Systems Engineering, Model 177 Ka). The temperature of the cavity was maintained at 65 K using a Bruker/ColdEdge FlexLine Cryostat (Model ER 4118HV-CF100). The bridge is equipped with an Arbitrary Wave Generator to create shaped pulses for increased sensitivity. The samples were made in D_2O buffers with 40 % (v/v) deuterated glycerol (used as the cryoprotectant). To perform an experiment, approximately 40 μ L of sample is added to a 3 mm OD, 2 mm ID quartz capillary and flash frozen in liquid nitrogen to preserve sample conformations. The following 4-pulsed DEER sequence was applied to all samples: πobs/2 – τ1 – πobs – (t- πpump) – (τ2-t) – πobs – τ2 – echo. V(t) is recorded as the integral of the refocused echo as a function of time delay, t, between the Hahn echo and pump pulse. Rectangular observe pulses and chirp pump pulse were used with the following pulse durations: π obs/2= 20 ns, π obs= 40 ns, π pump= 100 ns. The chirp pump pulse was applied with a frequency width of 60 MHz to excite a distinct spin population, referred to as B spins, while the observe pulse was set 33 G up field from the center of the pump frequency range to probe another distinct spin population, A spins. τ1 was set to 180 ns and τ2 was set according to the SNR profile of the dipolar signal. The data was acquired with resolution of 16 ns, 16-step phase cycling, and signal averaged until desirable SNR.

B.3 Figures

Figure B.1: $R2_8^1$ pulse sequence. In A) ii), ^{1}H to ^{31}P cross polarization (CP) and subsequent excitation and reconversion experimental blocks can be seen. The most sensitive parameter to optimization is the power level for the $R2_8^1$ recoupling block (plw11 in Supporting Information Listing 1 and 2 [35]). The experimental index must be set sufficiently large to encompass all MQCOs present. In green, additional 90 degree pulses are added to shift from even to odd quantum coherences [39]. Exact phases and pulse lengths can be seen in ii) and the relationship between signal intensity and phase increment can be seen simplified in Hughes and extended in Boutis [39][175]. Time evolution of MQCOs can be seen in B). It should be noted that the sample T_2 relaxation should be equal to or longer than the mixing time (where mixing time is double the excitation time reported). For our experiments, we additionally added presaturation on both channels to mitigate long D1 issues.
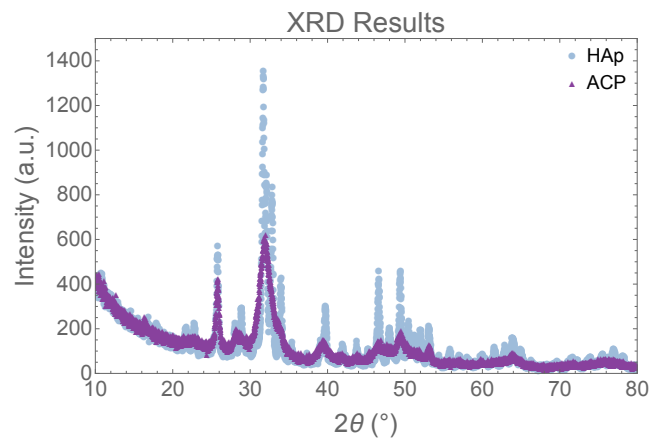
Figure B.2: X-Ray Diffraction results for HAp and ACP powdered samples. HAp fitting was matched to HighScore database with 98% accuracy. ACP was found to be consistent with literature [176] and found to be broader than HAp, as is expected for a glassy amorphous sample.
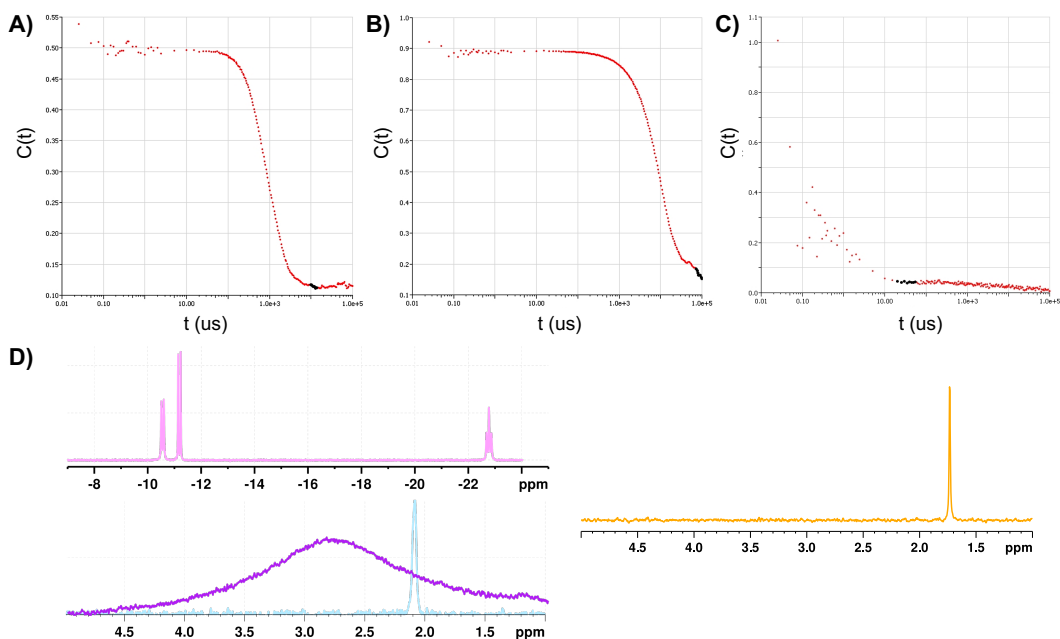
Figure B.3: Autocorelation function using dynamic light scattering (DLS) at 532.00 nm to check the size of suspended HAp and ACP and dissolved monophosphate in D_2O and H_2O and solution NMR 1D ^{31}P spectra before addition of AMUPol and glycerol-d8 for vitrification. Size and polydispersity were found by using the method of cumulants for DLS measurements. All ^{31}P solution NMR chemical shifts are innate (not chemical shift corrected). In A), HAp was found to be 595.40 nm in diameter with a polydispersity of 0.111 after a 10x dilution. In B), ACP was found to be 5472.72 nm in diameter with a polydispersity of 0.188 after a 200x dilution. DLS is sensitive to the largest species in solution and ACP is known to occupy a large range of sizes, so the polydispersity here is only a measure of the polydispersity of the micron sized ACP, not the full populations. In C), 1M monophosphate pH 7 control sample was found to be approximately 0 nm in diameter, however the high noise level makes it difficult to extract an accurate size and polydispersity. Different concentrations, experimental parameters, and amount of time collecting has been studied by Joshua Straub (in progress), which shows maximum size of 0.5 nm for monophosphate in water when there is less noise. In D), 1D solution spectra of ATP (pink), ACP (blue), HAp colloidal dispersion (purple), and 2 mM monophosphate control pH 7 (orange) are seen, dissolved in 90 % water and 10 % D_2O. HAp sample shown here in purple is arrested at 20-50 nm in size via colloidal dispersion (Thermo Scientific, J66691AC), as our HAp sample used elsewhere in this study is too large to be seen in traditional solution NMR idly. The broadness of ACP can be attributed to their well studied large polydispersity. All spectra exhibit arbitrary scaling for viewing ease as we are only interested in confirming phosphate state by relative line-broadening, which follows the expected trends.

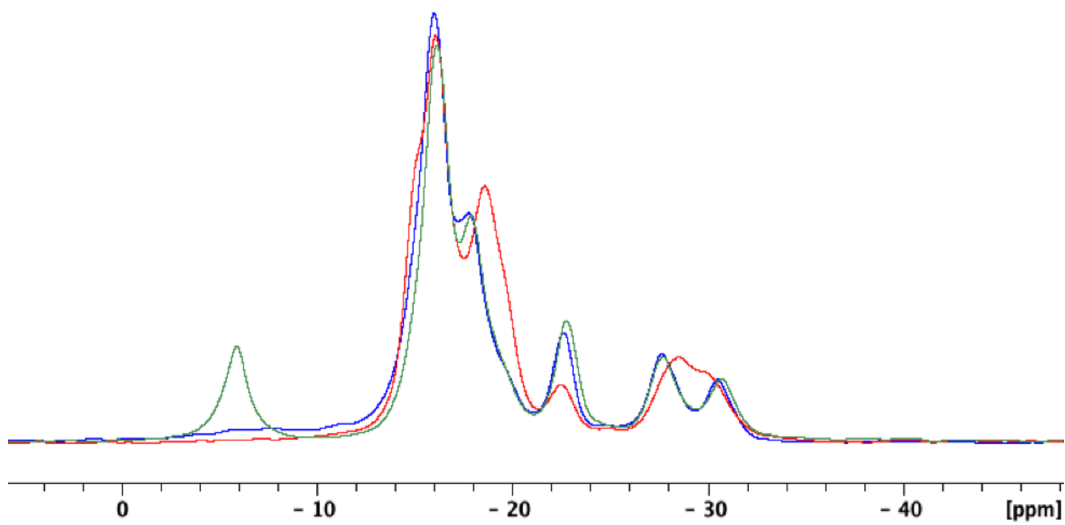Figure B.4: ATP Crystallinity Comparisons in solid state NMR (Raw chemical shifts). Blue = Normal (used in experiments, Sigma A2382) ATP of unknown crystallinity. Red = random sourced ATP of unknown crystallinity (Sigma-Aldrich A7699). Green = crystalline ATP (Sigma-Aldrich A3377). It can be seen that the blue signal which was used for spin counting experiments is comparatively sharp with the known crystalline green signal.

A)

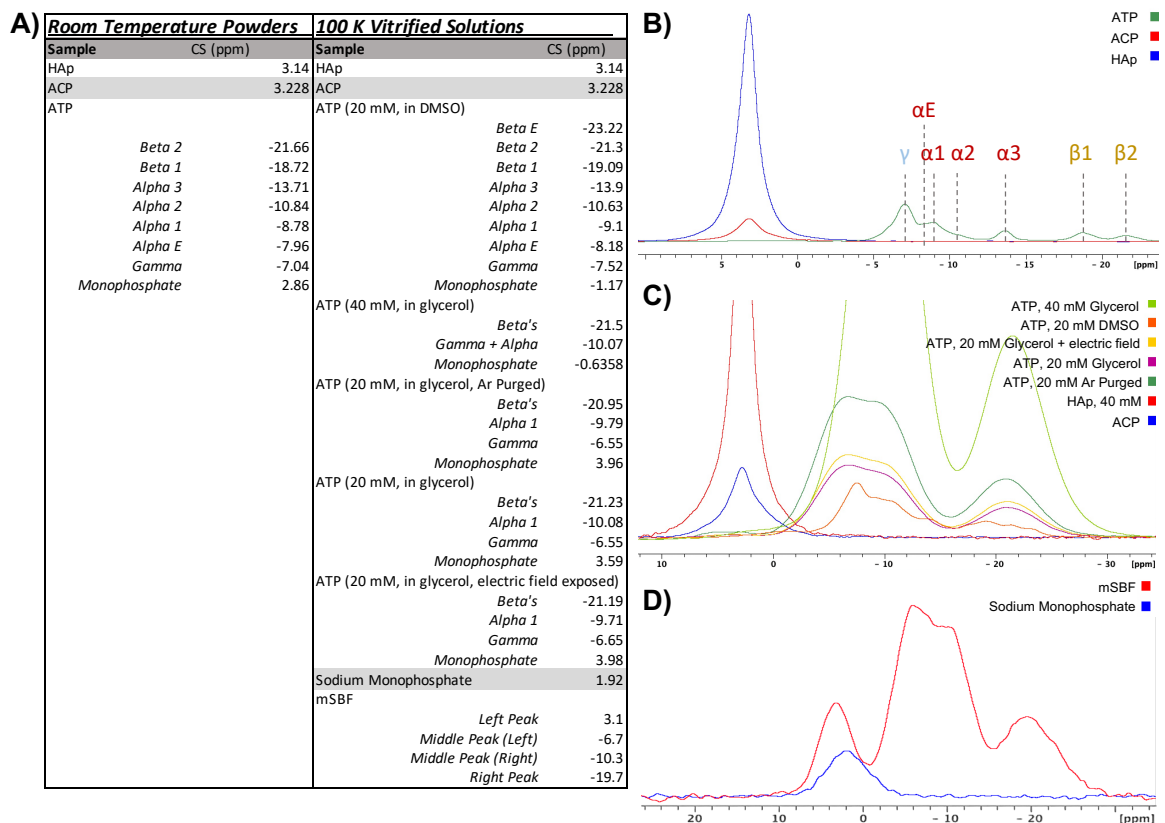| Room Temperature Powders		100 K Vitrified Solutions	
Sample	**CS (ppm)**	**Sample**	**CS (ppm)**
HAp	3.14	HAp	3.14
ACP	3.228	ACP	3.228
ATP		ATP (20 mM, in DMSO)	
		Beta E	-23.22
Beta 2	-21.66	Beta 2	-21.3
Beta 1	-18.72	Beta 1	-19.09
Alpha 3	-13.71	Alpha 3	-13.9
Alpha 2	-10.84	Alpha 2	-10.63
Alpha 1	-8.78	Alpha 1	-9.1
Alpha E	-7.96	Alpha E	-8.18
Gamma	-7.04	Gamma	-7.52
Monophosphate	2.86	Monophosphate	-1.17
		ATP (40 mM, in glycerol)	
		Beta's	-21.5
		Gamma + Alpha	-10.07
		Monophosphate	-0.6358
		ATP (20 mM, in glycerol, Ar Purged)	
		Beta's	-20.95
		Alpha 1	-9.79
		Gamma	-6.55
		Monophosphate	3.96
		ATP (20 mM, in glycerol)	
		Beta's	-21.23
		Alpha 1	-10.08
		Gamma	-6.55
		Monophosphate	3.59
		ATP (20 mM, in glycerol, electric field exposed)	
		Beta's	-21.19
		Alpha 1	-9.71
		Gamma	-6.65
		Monophosphate	3.98
		Sodium Monophosphate	1.92
		mSBF	
		Left Peak	3.1
		Middle Peak (Left)	-6.7
		Middle Peak (Right)	-10.3
		Right Peak	-19.7

Figure B.5: Solid state NMR chemical shifts (CS) of powdered and vitrified samples. All CS's were corrected to a standard phosphoric acid direct ^{31}P NMR chemical shift, however samples were analyzed over the course of 1.5 years with magnetic field drift that can not be fully accounted for; the average drift was -0.044 ppm per month based on powdered HAp and therefore CS error is approximately 0.79 ppm. All spectra shown are with innate scaling and similar line broadening of 50 or 100 Hz, however they were collected with varying dwell times (DW). In part A, each individual phosphorous environment is identified per sample in ppm. In part B, an overlay of all powdered samples (Fig. 3.1 and 3.2) at 16 scans can be shown with identification of ATP environments (See S6). In C, an overlay of all vitrified solutions (Fig. 3.1 and 3.2) at 16 scans can be seen. In D, an overlay of sodium monophosphate in DNP juice at 64 scans and DW of 2 μs (Fig. B10, II) with mSBF in DNP juice at 1024 scans and DW of 5 μs (Fig. 3.3) can be seen with the same line broadening of 100 Hz. These two spectra were taken within a month of each other for relative CS comparison.
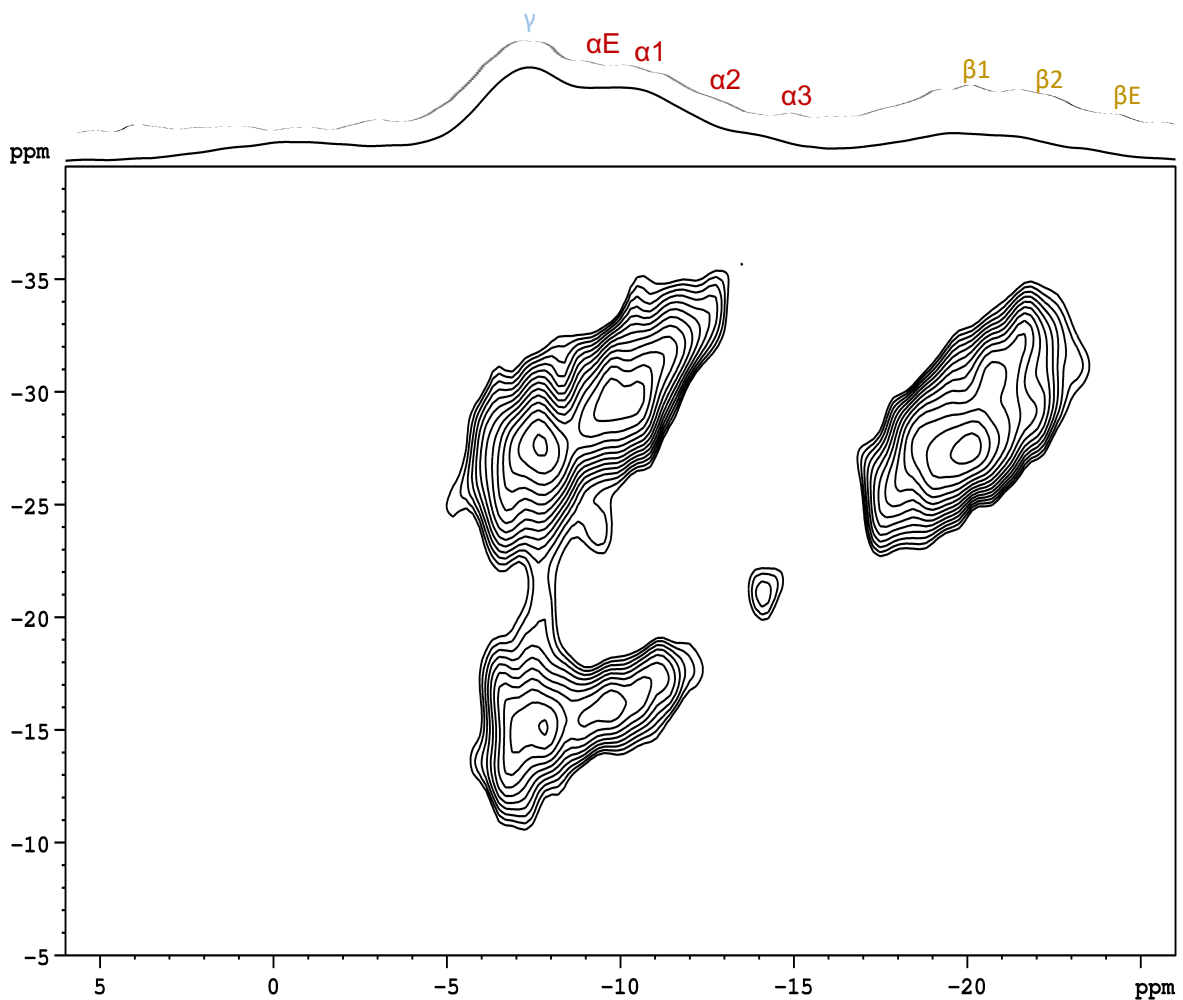
Figure B.6: SPC-5 DQ-SQ 2D NMR spectra of ATP at 100 K dissolved in DNP juice with DMSO glassing agent, referenced to phosphoric acid. 30 composite SPC-5 cycles (12 rotor periods) were used for excitation and reconversion. DQ-SQ signal is shown in light profile and 1D CP spectra is shown in dark solid line. Phosphate sites are identified and labeled based on connectivity and agree with literature[177], most similar to ATP dihydrate. The left ATP peak, identified as monophosphate (Fig. B10) shows no self correlations; this is in agreement with Q1 sites (no P-O-X bonds) being more downfield (leftshifted)[156].
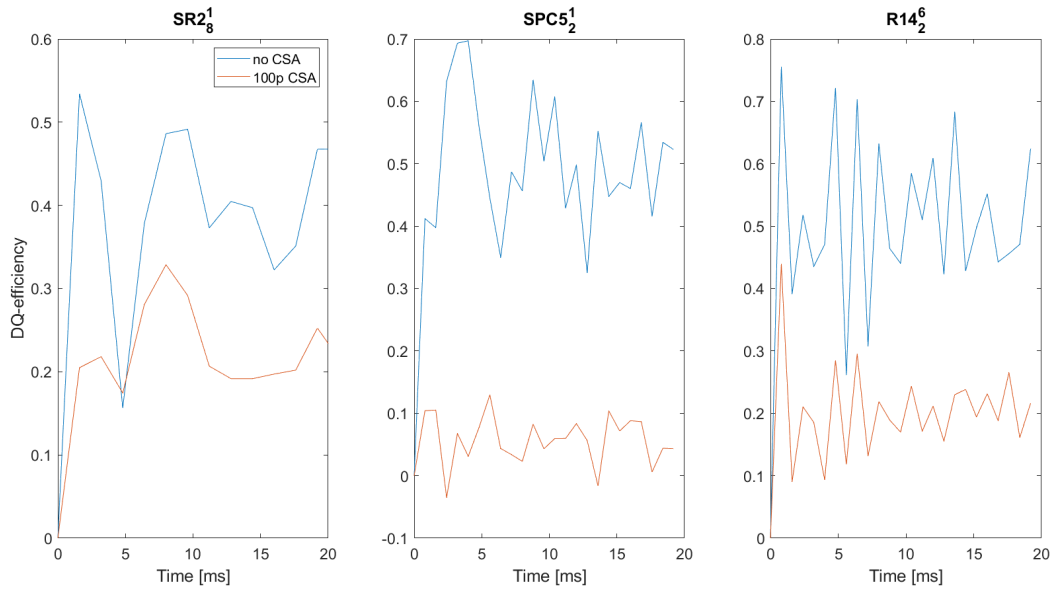
Figure B.7: DQ Efficiency Simulations varying CSA. These simulations were carried out with SIMPSON for a single spin pair of two ^{31}P nuclei with a distance of 2.5 Å (1500 Hz) of dipolar coupling strength. MAS frequency of 10 kHz was used.

Figure B.8: Distance Simulations. Six spin simulations by SIMPSON program carried out to generate the even spin counting profile and MQCOs. A linear arrangement of six ^{31}P spins with a distance of 2.5 Å and 10 kHz MAS was considered. No CSA was included.

Figure B.9: ATP Even SC Room Temperature. Integral area was defined over all ATP peaks (alpha, gamma, and beta).
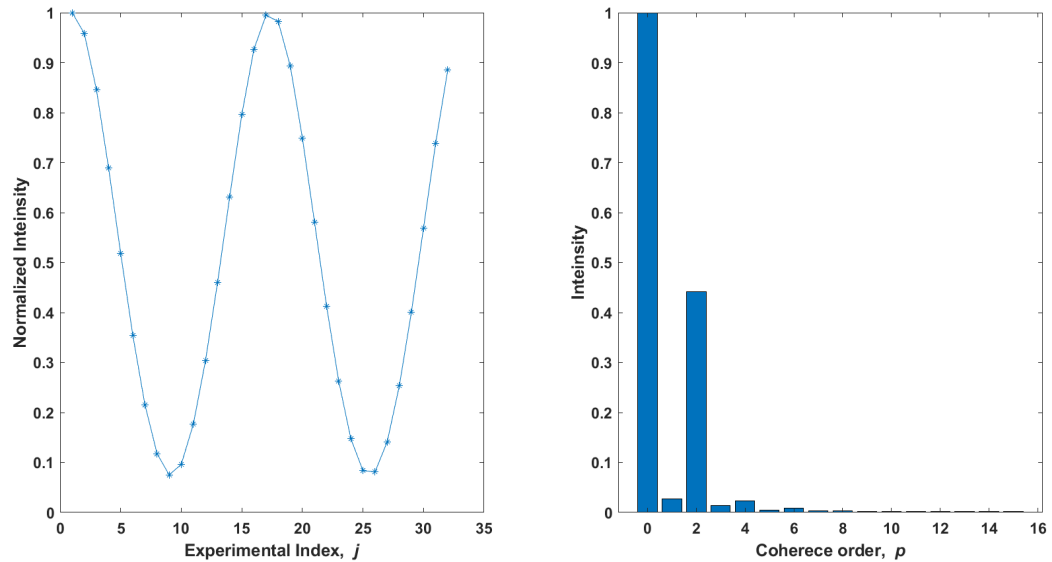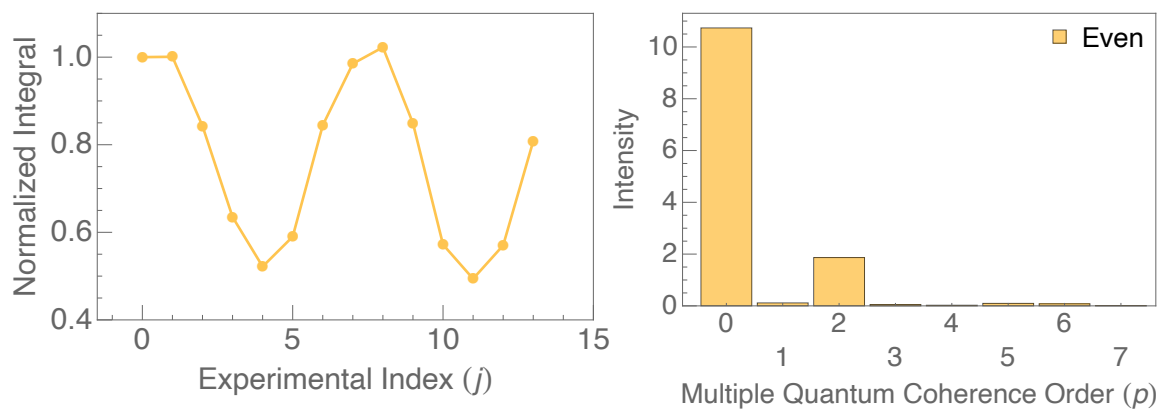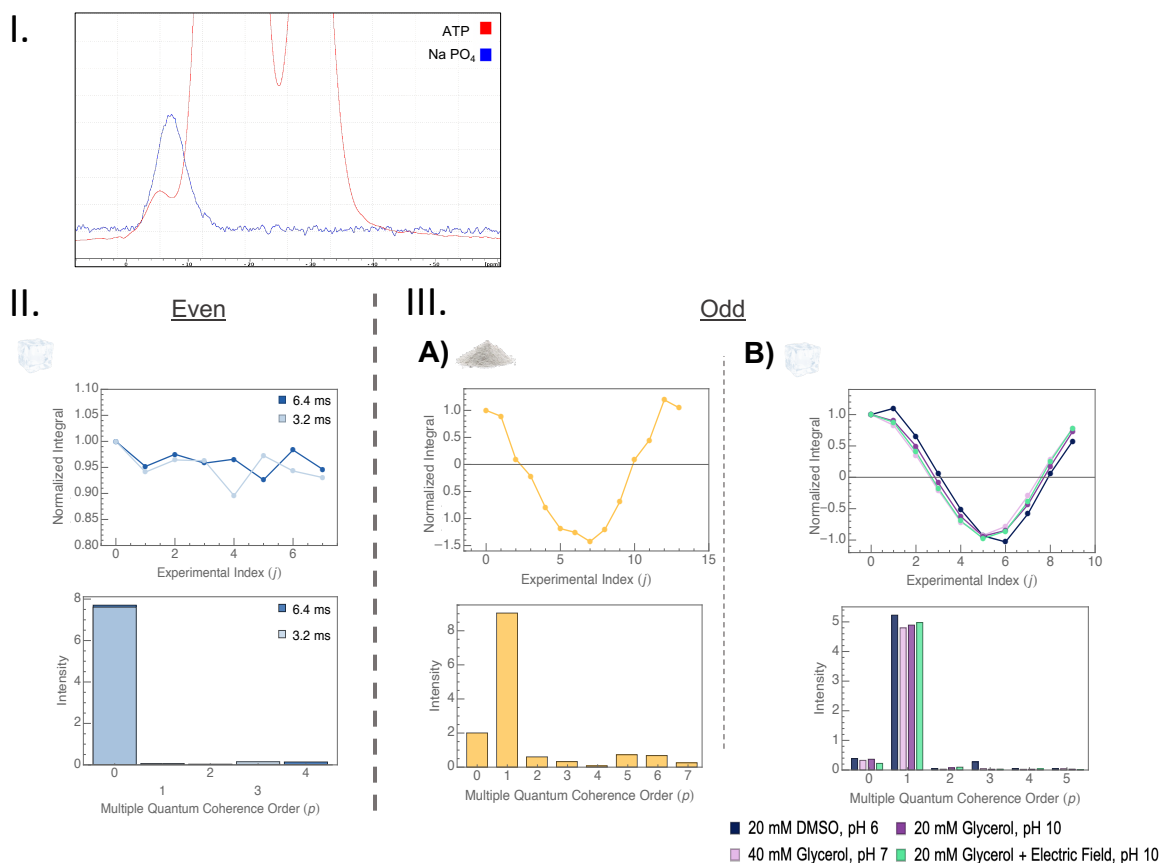
Figure B.10: Monophosphate Even and Odd SC. I) Overlap of vitrified 2 mM sodium monophosphate in glycerol, pH 7 control sample with vitrified 20 mM ATP in glycerol, pH 10 1D ^{31}P solid state NMR spectra. II) 2 mM (final concentration) sodium monophosphate pH 7 standard sample even SC under vitrified conditions for two different excitation times and a relaxation delay of 5 s. III) ATP monophosphate breakdown (left peak from part I, same as 20 mM in glycerol pH 10 sample in main paper Fig. 3.2C) odd SC at (a) powdered room temperature and (b) vitrified conditions. The observed profile shape is likely leakage from the overlapping gamma environment chemical shift. The T_2 relaxation time for this sample (Fig. B12) is sufficiently long as to not cause premature MQCO decay (longer than the 8 ms excitation time / 16 ms mixing time). DMSO is still expected to be clustering monophosphate as observed due to hydrophobic interactions, however no strong 2D connectivity is seen in Fig. B6.
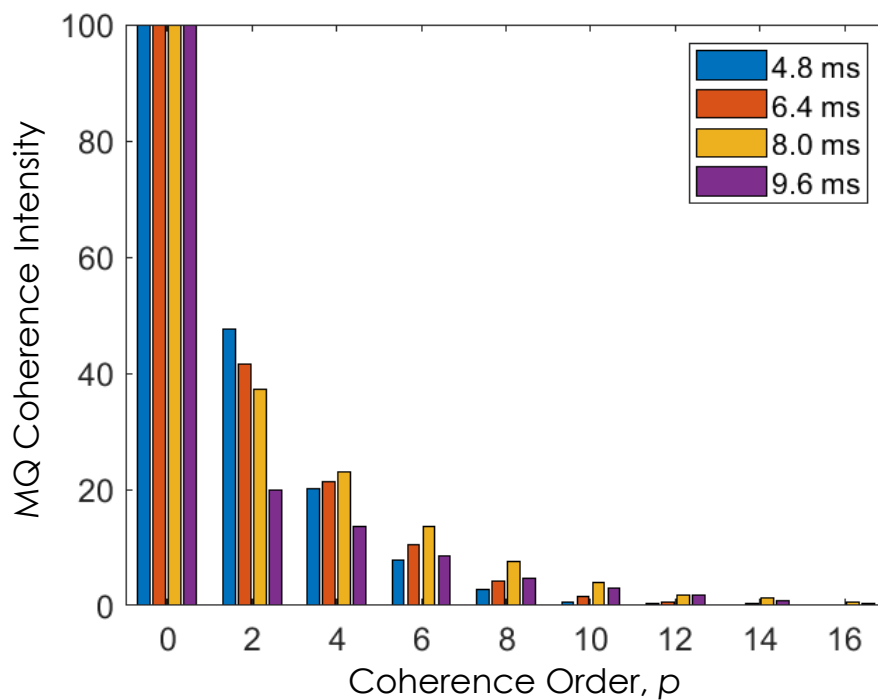
Figure B.11: Different excitation times for $SR2_8^1$ pulse sequence for HAp powdered sample at room temperature 10 kHz MAS. All taken with an experimental index of 32. Odd order coherences were removed for visual ease. The lower signal at shorter MQCOs as you increase excitation time can be attributed to distribution of spins over more spin states. The decay of higher MQCOs at longer excitation times is due to relaxation effects.

Room Temperature Powders					
Sample	**Exponential Fitting**	**T$_2$ (ms)**	**Population (%)**	**T$_2$ Error (ms)**	**Final Point (ms)**
HAp	Monoexponential	27.53	100	4.46	50
ACP	Monoexponential	16.22	100	2.1	50
	Biexponential	88.03	76.31	2.22	200
		4.34	23.69	0.44	200
ATP	Monoexponential	4	100	0.45	16
100 K Vitrified Solutions					
Sample	**Exponential Fitting**	**T$_2$ (ms)**	**Population (%)**	**T$_2$ Error (ms)**	**Final Point (ms)**
HAp	Monoexponential	7.94	100	0.85	50
ACP	Monoexponential	11.83	100	1.18	50
	Biexponential	2.35	26.42	0.17	50
		20.42	73.58	0.83	50
ATP (20 mM, in DMSO)	Biexponential	0.93	48.87	0.07	50
		13.56	51.12	0.94	50
ATP (40 mM, in glycerol)	Biexponential	8.32	49.36	0.41	50
		0.89	50.64	0.07	50
ATP (20 mM, in glycerol, Ar Purged)	Biexponential	17.92	58.3	1.56	50
		1.12	41.7	0.12	50
ATP (20 mM, in glycerol)	Biexponential	12.95	62.58	0.75	50
		0.9	37.42	0.1	50
ATP (20 mM, in glycerol, electric field)	Biexponential	0.82	38.77	0.15	50
		11.39	61.23	1.05	50
Monophosphate (ATP 20 mM, in glycerol)	Monoexponential	9.45	100	1.05	50
Sodium Monophosphate Control	Biexponential	1.85	71.63	0.23	50
		14.31	28.37	4.9	50
mSBF (All Peaks)	Biexponential	1.29	49.4	0.2	50
		14.67	50.6	1.36	50
mSBF (Middle Two Peaks)	Biexponential	1.17	53.14	0.23	50
		14.17	46.86	1.85	50

Figure B.12: T$_2$ relaxation times for powdered and vitrified solution samples with continuous ^{1}H decoupling extracted by a custom python processing program. T$_2$ shown for ATP was taken for all peaks except for monophosphate (shown separately). T$_2$ shown for mSBF was taken for all peaks, in addition to taken for only the middle two peak environments (shown separately). When a sample exhibits two distinct T$_2$ components; we only consider the larger component that changes between sample preparation in the main paper. It should be noted that T$_2$ had to be cut off at 50 ms due to continuous ^{1}H decoupling in order not to burn the NMR probe. We accidentally ran ACP at room temperature for 200 and 50 ms, where one can see that 50 ms can result in an artificially shorted extracted T$_2$ relaxation time. In addition, we processed the same data set of ACP in DNP juice with both a monoexponential and biexponential fit, to showcase the difference in extracted values for a similarly agreeable visual fit.

Room Temperature Powders

Sample	CSA (δ) (ppm)	CSA (η)	δ Error (%)	η Error
HAp	-22.9775	0.1	2.3	0.02
ACP	-25	0.05	4.5	0.02
ATP				
Beta 2	-130	0.4	0.5	0.02
Beta 1	-130	0.4	0.3	0.01
Alpha 3	-120	0.5	2.5	0.01
Alpha 2	-100	0.4	0.7	0.05
Alpha 1	-110	0.5	0.7	0.01
Gamma	-115	0.3	6	0.005
Monophosphate	-10	0.3	5	0.1

100 K Vitrified Solutions

Sample	CSA (δ) (ppm)	CSA (η)	δ Error (%)	η Error
HAp	-20.837	0.1	2.3	0.02
ACP	40	0.5	1.4	0.06
ATP (20 mM, in DMSO)				
Beta E	-118.483	0.72345	1.6	0.05
Beta 2	-112.485	0.33966	0.4	0.02
Beta 1	-128.717	0.51415	0.2	0.01
Alpha 3	-111.423	0.74275	0.5	0.01
Alpha 2	-112.003	0.70362	0.2	0.01
Alpha 1	-109.89	0.55649	0.5	0.02
Gamma	-108.012	0.60745	1	0.04
Monophosphate	-50.1691	0.42425	8	0.1
ATP (40 mM, in glycerol)				
Beta's	-129.742	0.42192	0.1	0.01
Gamma + Alpha	-107.559	0.64086	0.5	0.01
Monophosphate	100	0.4	8	0.1
ATP (20 mM, in glycerol, Ar Purged)				
Beta's	-120.076	0.49968	1	0.01
Alpha 1	-116.992	0.50018	1	0.01
Gamma	86.0083	0.39783	1	0.01
Monophosphate	-4.8	0.8	4	0.1
ATP (20 mM, in glycerol)				
Beta's	-125.068	0.42996	0.1	0.04
Alpha 1	-109.916	0.63404	0.1	0.03
Gamma	90.3015	0.40189	0.1	0.05
Monophosphate	49.4287	0.47531	5	0.1
ATP (20 mM, in glycerol, electric field exposed)				
Beta's	-120.044	0.4996	1	0.03
Alpha 1	-115	0.50049	0.1	0.03
Gamma	90	0.39915	0.1	0.06
Monophosphate	-2.4	0.17	6	0.1
Sodium Monophosphate	-68.4	0.1	1.5	0.01
mSBF				
Left Peak	-60	0.3	2	0.07
Middle Peak (Left)	80	0.77	1	0.02
Middle Peak (Right)	-110	0.8	1	0.01
Middle Peak (Left + Right)	-92	0.84	1	0.01
Right Peak	-110	0.6	1	0.01

Figure B.13: CSA extraction using DMfit software program. CSA-MAS model is used for extracting the CSA parameters such as CSA (δ) (chemical shift aniosotropy), CSA(η) is the asymmetry parameter of the CSA.

Figure B.14: MQ-SC of mSBF at varying excitation times. Number of scans, relaxation delay, and number of points acquired varied per experiment, however all other parameters were kept consistent.
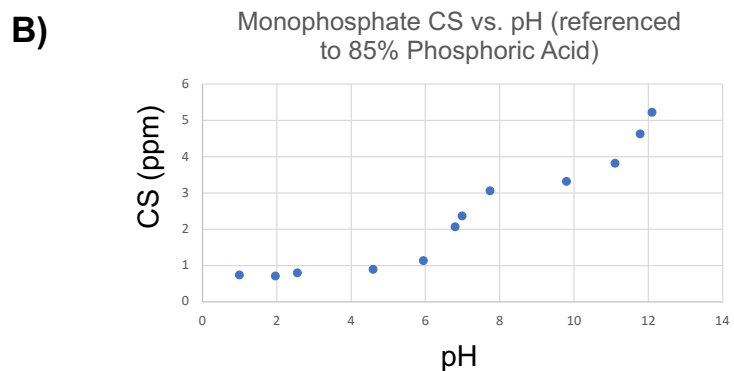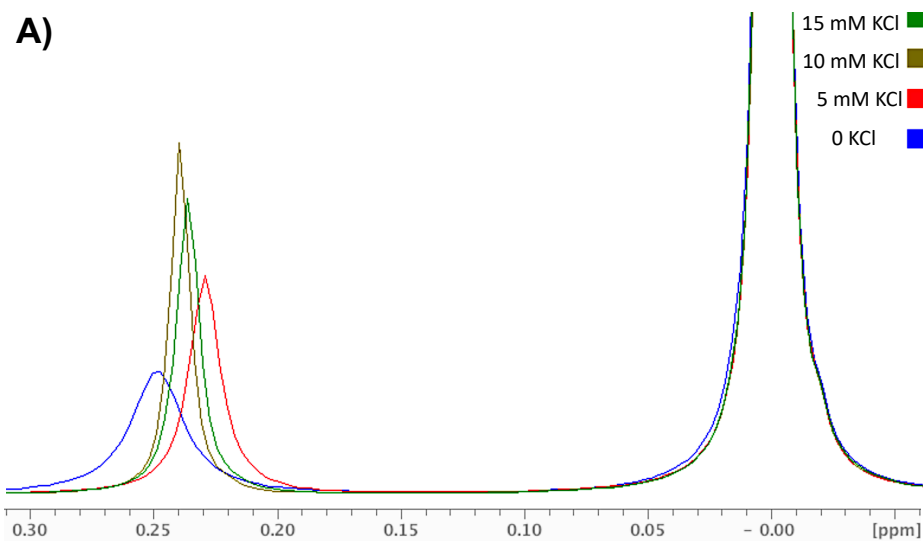
Figure B.15: A) Solution ^{31}P NMR of 30 mM KH$_2$PO$_4$ with varying concentrations of KCl in order to vary solution ionic strength. All samples were taken on the 500 MHz Bruker spectrometer, corrected to a pH of 5.2, and a phosphoric acid coaxial insert internal standard was utilized to normalize chemical shifts across samples, as seen by the right peak. B) Solution ^{31}P NMR of 100 mM KH$_2$PO$_4$ at varying pH values. All samples were taken on a 400 MHz Varian spectrometer and corrected to a phosphoric acid external standard to normalize chemical shifts across samples. Addition of a second phosphate P-O-P bond (pyrophosphate) shifts chemical shift by approximately -10 ppm.

Bibliography

[1] N.-A. L.F. and G.-G. J., *Brain computer interfaces, a review.*, *Sensors (Basel)* **12** (2012), no. 2 1211–1279. `https://doi.org/10.3390/s120201211`.

[2] M. ming Poo, M. Pignatelli, T. J. Ryan, S. Tonegawa, T. Bonhoeffer, K. C. Martin, A. Rudenko, L.-H. Tsai, R. W. Tsien, G. Fishell, C. Mullins, J. T. Gonçalves, M. Shtrahman, S. T. Johnston, F. H. Gage, Y. Dan, J. Long, G. Buzsáki, and C. Stevens, *What is memory? the present state of the engram.*, *BMC Biology* **14** (2016), no. 40 1–18. `https://doi.org/10.1186/s12915-016-0261-6`.

[3] M. B. Kennedy, *Synaptic signaling in learning and memory*, *Cold Spring Harbor Perspectives in Biology* **8** (2016), no. 2 1–16.

[4] M. A. Nielsen and I. L. Chuang, *Quantum computation and quantum information: 10th anniversary edition.*, *Cambridge University Press* (2011).

[5] J. Mcfadden and J. Al-Khalili, *The origins of quantum biology*, *Proc Math Phys Eng Sci.* **474** (2018) 1–13.

[6] S. Hameroff, *Quantum computation in brain microtubules? the penrose-hameroff 'orch or' model of consciousness*, *Phil. Trans. R. Soc. Lond.* **356** (1998) 1869–1896. `https://doi.org/10.1098/rsta.1998.0254`.

[7] M. P. Fisher, *Quantum cognition: The possibility of processing with nuclear spins in the brain*, *Annals of Physics* **362** (2015), no. 1 593–602. `https://doi.org/10.1016/j.aop.2015.08.020`.

[8] M. Vignais, A. Caicedo, J. Brondello, and C. Jorgensen, *Cell connections by tunneling nanotubes: Effects of mitochondrial trafficking on target cell metabolism, homeostasis, and response to therapy.*, *Stem Cells Int* (2017) 1–15.

[9] C. P. Weingarten, P. M. Doraiswamy, and M. P. A. Fisher, *A new spin on neural processing: Quantum cognition*, *Front. Hum. Neurosci.* **10** (2016). `https://doi.org/10.3389/fnhum.2016.00541`.

[10] A. Hagenston and H. Bading, *Calcium signaling in synapse-to-nucleus communication.*, *Cold Spring Harb Perspect Biol.* **3** (2011), no. 11 1–31.

[11] P. B. Mitchell and D. Hadzi-Pavlovic, *Lithium treatment for bipolar disorder*, *Bulletin of the World Health Organization* **78** (2000), no. 4 515–517. PMID: 10885179, PMCID: PMC2560742.

[12] J. A. Sechzer, K. W. Lieberman, G. J. Alexander, D. Weidman, and P. E. Stokes, *Aberrant parenting and delayed offspring development in rats exposed to lithium*, *Biol Psychiatry* **21** (1986), no. 13 1258–66.
https://doi.org/10.1016/0006-3223(86)90308-2.

[13] Z. Liew, Q. Meng, Q. Yan, J. Schullehner, B. Hansen, S. M. Kristiansen, D. D. Voutchkova, J. Olsen, A. K. Ersbøll, M. Ketzel, O. Raaschou-Nielsen, and B. R. Ritz, *Association between estimated geocoded residential maternal exposure to lithium in drinking water and risk for autism spectrum disorder in offspring in denmark*, *JAMA Pediatr.* **177** (2023), no. 6 617–624.
https://doi.org/10.1001/jamapediatrics.2023.0346.

[14] D. C. Bellinger, *Lithium in drinking water—a novel environmental risk factor for autism spectrum disorder?*, *JAMA Pediatr.* **177** (2023), no. 6 563–564.
https://doi.org/10.1001/jamapediatrics.2023.0330.

[15] MEDSAFE, *Lithium and pregnancy*, *Prescriber Update: New Zealand Medicines and Medical Devices Safety Authority* (2019). https://medsafe.govt.nz/profs/PUArticles/March2019/Lithium%20and%20pregnancy.htm.

[16] V. Blüml, M. D. Regier, G. Hlavin, I. R. H. Rockett, F. König, B. Vyssoki, T. Bschor, and N. D. Kapusta, *Lithium in the public water supply and suicide mortality in texas*, *Journal of Psychiatric Research* **47** (2013), no. 3 407–11.
https://doi.org/10.1016/j.jpsychires.2012.12.002.

[17] S. N, Y.-F. N, I. N, I. N, and T. T., *Lithium in tap water and suicide mortality in japan*, *Int J Environ Res Public Health.* **10** (2013), no. 11 6044–8.
https://doi.org/10.3390/ijerph10116044.

[18] L. V, M. N, R. N, N. R, and S. L., *Lithium levels in the public drinking water supply and risk of suicide: A pilot study*, *J Trace Elem Med Biol.* **43** (2017) 197–201. https://doi.org/10.1016/j.jtemb.2017.03.009.

[19] K. LV, G. TA, K. NN, J. LF, K. SM, V. D, E. V, S. J, H. B, A. PK, and E. AK., *Association of lithium in drinking water with the incidence of dementia*, *JAMA Psychiatry* **74** (2017), no. 10 1005–1010.
https://doi.org/10.1001/jamapsychiatry.2017.2362.

[20] N. MA, S. NM, M.-S. KC, B.-T. T, S. SI, B. J, A. MS, C. AL, V. TA, and B. HS., *Chronic microdose lithium treatment prevented memory loss and neurohistopathological changes in a transgenic mouse model of alzheimer's disease*, *PLoS One* **10** (2015), no. 11. https://doi.org/10.1371/journal.pone.0142267.

[21] M. Eng, *Is lithium deficiency real? health effects of low lithium*, *SelfDecode* (2021). https://supplements.selfdecode.com/blog/lithium-deficiency/.

[22] E. Shorter, *The history of lithium therapy*, *Bipolar Disord.* **11** (2009) 4–9. https://doi.org/10.1111/j.1399-5618.2009.00706.x.

[23] J. S. Straub, M. Patel, M. S. Nowotarski, L. R. Potnuru, M. Fisher, and M. Helgeson, *A differential lithium isotope effect on the in vitro formation of calcium phosphate*, *In Preparation* (2023).

[24] A. S. Posner and F. Betts, *Synthetic amorphous calcium phosphate and its relation to bone mineral structure*, *Acc. Chem. Res.* **8** (1975), no. 8 273–281. https://doi.org/10.1021/ar50092a003.

[25] V. Campana, G. Milano, E. Pagano, M. Barba, C. Cicione, G. Salonna, W. Lattanzi, and G. Logroscino, *Bone substitutes in orthopaedic surgery: from basic science to clinical practice*, *J Mater Sci Mater Med.* **25** (2014), no. 10 2445–61. https://doi.org/10.1007/s10856-014-5240-2.

[26] K. Onuma and A. Ito, *Cluster growth model for hydroxyapatite*, *Chem. Mater.* **10** (1998), no. 11 3346–3351. https://doi.org/10.1021/cm980062c.

[27] W. P. Rothwell, J. S. Waugh, and J. P. Yesinowski, *High-resolution variable-temperature 31p nmr of solid calcium phosphates*, *J. Am. Chem. Soc.* **102** (1980), no. 8 2637–2643. https://doi.org/10.1021/ja00528a020.

[28] M. Bohner, J. LeMaître, A. P. LeGrand, J.-B. D. de la Caillerie, and P. Belgrand, *Synthesis, x-ray diffraction and solid-state 31p magic angle spinning nmr study of -tricalcium orthophosphate*, *Journal of Materials Science: Materials in Medicine* **7** (1996) 457–463. https://doi.org/10.1007/BF00122016.

[29] J. F. MacDonald, *Multinuclear solid state nmr studies of -tricalcium phosphate and silicon substituted -tricalcium phosphate*, *PhD Thesis, University of Warwick* (2012).

[30] M. W. Swift, C. G. Van De Walle, and M. P. A. Fisher, *Posner molecules: From atomic structure to nuclear spins.*, *Physical Chemistry Chemical Physics* **20** (2018) 12373–12380. https://doi.org/10.1039/C7CP07720C.

[31] A. Dey, P. H. H. Bomans, F. A. Müller, J. Will, P. M. Frederik, G. de With, and N. A. J. M. Sommerdijk, *The role of prenucleation clusters in surface-induced calcium phosphate crystallization*, Nature Materials **9** (2010), no. 1 1010–1014. `https://doi.org/10.1038/nmat2900`.

[32] Q. Zhang, Y. Jiang, B.-D. Gou, J. Huang, Y.-X. Gao, J.-T. Zhao, L. Zheng, Y.-D. Zhao, T.-L. Zhang, and K. Wang, *In situ detection of calcium phosphate clusters in solution and wet amorphous phase by synchrotron x-ray absorption near-edge spectroscopy at calcium k-edge*, Cryst. Growth Des. **15** (2015), no. 5 2204–2210. `https://doi.org/10.1021/cg5018505`.

[33] N. Kanzaki, K. Onuma, A. Ito, K. Teraoka, T. Tateishi, and S. Tsutsumi, *Direct growth rate measurement of hydroxyapatite single crystal by moire phase shift interferometry*, J. Phys. Chem. B **102** (1998), no. 34 6471–6476. `https://doi.org/10.1021/jp981512r`.

[34] J. S. Straub, M. Patel, M. S. Nowotarski, M. Fisher, and M. E. Helgeson, *Direct evidence for free calcium phosphate prenucleation species in solution.*, In Preparation. (2023).

[35] M. S. Nowotarski, L. R. Potnuru, J. S. Straub, R. Chaklashiya, T. Shimasaki, B. Pahari, H. Coffaro, S. Jain, and S. Han, *Dnp enhanced multiple quantum solid state nmr spin counting of molecular assemblies in vitrified solutions.*, JPC Letters (Submitted, 2023).

[36] A. S. Posner, F. Betts, and N. C. Blumenthal, *Formation and structure of synthetic and bone hydroxyapatites*, Progress in Crystal Growth and Characterization **3** (1980), no. 1 49–64. `https://doi.org/10.1016/0146-3535(80)90011-8`.

[37] M. E. Zilm, L. Chen, V. Sharma, A. McDannald, M. Jain, R. Ramprasada, and M. Wei, *Hydroxyapatite substituted by transition metals: experiment and theory*, Physical Chemistry Chemical Physics **18** (2016), no. 24 16457–16465. `https://doi.org/10.1039/c6cp00474a`.

[38] S. J. DeVience, R. L. Walsworth, and M. S. Rosen, *Preparation of nuclear spin singlet states using spin-lock induced crossing*, Phys. Rev. Lett. **111** (2013), no. 17. `https://doi.org/10.1103/PhysRevLett.111.173002`.

[39] C. E. Hughes, *Spin counting*, Progress in Nuclear Magnetic Resonance Spectroscopy **45** (2004), no. 3-4 301–313. `https://doi.org/10.1016/j.pnmrs.2004.08.002`.

[40] P. Singhal, A. Luk, and J. Butany, *Bioprosthetic heart valves: Impact of implantation on biomaterials*, ISRN Biomaterials (2013). `https://doi.org/10.5402/2013/728791`.

[41] J. S. Straub, M. S. Nowotarski, J. Lu, T. Sheth, S. Jiao, M. P. Fisher, M. S. Shell, M. E. Helgeson, A. Jerschow, and S. Han, *Phosphates form spectroscopically dark state assemblies in common aqueous solutions*, *PNAS* **120** (2022), no. 1 1–10. `https://doi.org/10.1073/pnas.2206765120,`.

[42] J. R. Knowles, *Enzyme-catalyzed phosphoryl transfer reactions*, *Annual Review of Biochemistry* **49** (1980), no. 1 877–919. `https://doi.org/10.1146/annurev.bi.49.070180.004305.`

[43] P. P. Dzeja and A. Terzic, *Phosphotransfer networks and cellular energetics*, *Journal of Experimental Biology* **206** (06, 2003) 2039–2047. `https://doi.org/10.1242/jeb.00426.`

[44] N. Blumenthal and A. Posner, *Hydroxyapatite: Mechanism of formation and properties*, *Cal. Tis Res.* **13** (1973) 235–243. `https://doi.org/10.1007/BF02015413.`

[45] H. Schröder, L. Kurz, W. Müller, and B. Lorenz, *Polyphosphate in bone*, *Biochemistry (Moscow)* **65** (2000), no. 3 296–303. PMID:10739471.

[46] L. Wang and G. H. Nancollas, *Calcium orthophosphates: Crystallization and dissolution*, *Chemical Reviews* **108** (2008), no. 11 4628–4669. `https://doi.org/10.1021/cr0782574.`

[47] A. McLaughlin, P. Cullis, M. Hemminga, D. Hoult, G. Radda, G. Ritchie, P. Seeley, and R. Richards, *Application of ^{31}P NMR to model and biological membrane systems*, *FEBS Letters* **57** (1975), no. 2 213–218. `https://doi.org/10.1016/0014-5793(75)80719-8.`

[48] E. Burnell, P. Cullis, and B. de Kruijff, *Effects of tumbling and lateral diffusion on phosphatidylcholine model membrane ^{31}P-NMR lineshapes*, *Biochimica et Biophysica Acta (BBA) - Biomembranes* **603** (1980), no. 1 63–69. `https://doi.org/10.1016/0005-2736(80)90391-0.`

[49] Y. Su, W. F. DeGrado, and M. Hong, *Orientation, dynamics, and lipid interaction of an antimicrobial arylamide investigated by ^{19}F and ^{31}P solid-state NMR spectroscopy*, *Journal of the American Chemical Society* **132** (2010), no. 26 9197–9205. `https://doi.org/10.1021/ja103658h.`

[50] C. Ho, J. A. Magnuson, J. B. Wilson, N. S. Magnuson, and R. J. Kurland, *Phosphorus nuclear magnetic resonance studies of phosphoproteins and phosphorylated molecules. II. Chemical nature of phosphorus atoms in α_8-casein B and phosvitin*, *Biochemistry* **8** (1969), no. 5 2074–2082. `https://doi.org/10.1021/bi00833a044.`

[51] M. H. J. Seifert, C. B. Breitenlechner, D. Bossemeyer, R. Huber, T. A. Holak, and R. A. Engh, *Phosphorylation and flexibility of cyclic-AMP-dependent protein kinase (PKA) using ^{31}P NMR spectroscopy*, Biochemistry **41** (2002), no. 19 5968–5977. `https://doi.org/10.1021/bi025509g`.

[52] J. Ren, B. Yang, A. Sherry, and C. Malloy, *Exchange kinetics by inversion transfer: integrated analysis of the phosphorus metabolite kinetic exchanges in resting human skeletal muscle at 7 T*, Magnetic resonance in medicine **73** (2015), no. 4 1359–1369. `https://doi.org/10.1002/mrm.25256`.

[53] M. Hupfer, R. Gtichter, and R. R. Ruegger, *Polyphosphate in lake sediments: ^{31}P NMR spectroscopy as a tool for its identification*, Limnology and Oceanography **40** (1995), no. 3 610–617.

[54] L. B. Staal, A. B. Petersen, C. A. JÃžrgensen, U. G. Nielsen, P. H. Nielsen, and K. Reitzel, *Extraction and quantification of polyphosphates in activated sludge from waste water treatment plants by ^{31}P NMR spectroscopy*, Water Research **157** (2019) 346–355. `https://doi.org/10.1016/j.watres.2019.03.065`.

[55] E. M. M. Weber, T. Kress, D. Abergel, S. Sewsurn, T. Azaïs, and D. Kurzbach, *Assessing the onset of calcium phosphate nucleation by hyperpolarized real-time nmr*, Anal Chem. **92** (2020), no. 11 7666–7673. `https://doi.org/10.1021/acs.analchem.0c00516`.

[56] M. A. Swartz, P. J. Tubergen, C. D. Tatko, and R. A. Baker, *Experimental determination of pKa values and metal binding for biomolecular compounds using ^{31}P NMR spectroscopy*, Journal of Chemical Education **95** (2018), no. 1 182–185. `https://doi.org/10.1021/acs.jchemed.7b00508`.

[57] Z. Szabó, *Multinuclear NMR studies of the interaction of metal ions with adenine-nucleotides*, Coordination Chemistry Reviews **252** (2008), no. 21 2362–2380. `https://doi.org/10.1016/j.ccr.2008.03.002`.

[58] R. K. Brow, C. C. Phifer, G. L. Turner, and R. J. Kirkpatrick, *Cation effects on ^{31}P MAS NMR chemical shifts of metaphosphate glasses*, Journal of the American Ceramic Society **74** (1991), no. 6 1287–1290. `https://doi.org/10.1111/j.1151-2916.1991.tb04099.x`.

[59] J. Iwahara, Y.-S. Jung, and G. M. Clore, *Heteronuclear nmr spectroscopy for lysine NH₃ groups in proteins: Unique effect of water exchange on ^{15}N transverse relaxation*, Journal of the American Chemical Society **129** (2007), no. 10 2971–2980. `https://doi.org/10.1021/ja0683436`.

[60] Z. Luz and S. Meiboom, *Rate and mechanism of proton exchange in aqueous solutions of phosphate buffer*, Journal of the American Chemical Society **86** (1964), no. 22 4764–4766. `https://doi.org/10.1021/ja01076a006`.

[61] H. Y. Carr and E. M. Purcell, *Effects of diffusion on free precession in nuclear magnetic resonance experiments*, *Phys. Rev.* **94** (May, 1954) 630–638. https://doi.org/10.1103/PhysRev.94.630.

[62] S. Meiboom and D. Gill, *Modified spin-echo method for measuring nuclear relaxation times*, *Review of Scientific Instruments* **29** (Aug., 1958) 688–691. https://doi.org/10.1063/1.1716296.

[63] N. Bloembergen, E. M. Purcell, and R. V. Pound, *Relaxation effects in nuclear magnetic resonance absorption*, *Phys. Rev.* **73** (Apr, 1948) 679–712. https://doi.org/10.1103/PhysRev.73.679.

[64] J. Fraústo da Silva and R. Williams, *The Biological Chemistry of the Elements: The Inorganic Chemistry of Life*. Oxford University Press, Oxford, 1997.

[65] J. P. Yesinowski, R. J. Sunberg, and J. J. Benedict, *pH control and rapid mixing in spinning NMR samples*, *Journal of Magnetic Resonance (1969)* **47** (1982), no. 1 85–90. https://doi.org/10.1016/0022-2364(82)90323-7.

[66] T. R. Krawietz, P. Lin, K. E. Lotterhos, P. D. Torres, D. H. Barich, A. Clearfield, and J. F. Haw, *Solid phosphoric acid catalyst: A multinuclear NMR and theoretical study*, *Journal of the American Chemical Society* **120** (1998), no. 33 8502–8511. https://doi.org/10.1021/ja9813461.

[67] N. J. Anthis and G. M. Clore, *Visualizing transient dark states by nmr spectroscopy*, *Quarterly Reviews of Biophysics* **48** (2015), no. 1 35–116.

[68] J. M. Edwards, J. E. Bramham, A. Podmore, S. M. Bishop, C. F. van der Walle, and A. P. Golovanov, ^{19}F *dark-state exchange saturation transfer NMR reveals reversible formation of protein-specific large clusters in high-concentration protein mixtures*, *Analytical Chemistry* **91** (2019), no. 7 4702–4708. https://doi.org/10.1021/acs.analchem.9b00143.

[69] P. Vallurupalli, G. Bouvignies, and L. E. Kay, *Studying invisible excited protein states in slow exchange with a major state conformation*, *Journal of the American Chemical Society* **134** (2012), no. 19 8148–8161. https://doi.org/10.1021/ja3001419.

[70] I. A. L. Lim, X. Li, C. K. Jones, J. A. Farrell, D. S. Vikram, and P. C. van Zijl, *Quantitative magnetic susceptibility mapping without phase unwrapping using WASSR*, *NeuroImage* **86** (2014) 265–279. https://doi.org/10.1016/j.neuroimage.2013.09.072.

[71] H. Hogben, M. Krzystyniak, G. Charnock, P. Hore, and I. Kuprov, *Spinach–a software library for simulation of spin dynamics in large spin systems*, *J Magn Reson* **208** (2011), no. 2 179–194.

[72] A. G. Palmer III, *Chemical exchange in biomacromolecules: past, present, and future*, J Magn Reson **241** (2014) 3–17.

[73] J. Zhou and P. C. van Zijl, *Chemical exchange saturation transfer imaging and spectroscopy*, Prog Nucl Magn Reson Spectrosc **48** (2006), no. 2-3 109–136.

[74] P. C. Van Zijl and N. N. Yadav, *Chemical exchange saturation transfer (CEST): what is in a name and what isn't?*, Magn Reson Med **65** (2011), no. 4 927–948.

[75] N. D. Burrows and R. L. Penn, *Cryogenic transmission electron microscopy: Aqueous suspensions of nanoscale objects*, Microscopy and Microanalysis **19** (2013), no. 6 1542–1553.

[76] H. Cui, T. K. Hodgdon, E. W. Kaler, L. Abezgauz, D. Danino, M. Lubovsky, Y. Talmon, and D. J. Pochan, *Elucidating the assembled structure of amphiphiles in solution via cryogenic transmission electron microscopy*, Soft Matter **3** (2007) 945–955.

[77] W. Humphrey, A. Dalke, and K. Schulten, *VMD: Visual molecular dynamics*, Journal of Molecular Graphics **14** (1996), no. 1 33–38. https://doi.org/10.1016/0263-7855(96)00018-5.

[78] M. Golda-Cepa, K. Riedlová, W. Kulig, L. Cwiklik, and A. Kotarba, *Functionalization of the parylene c surface enhances the nucleation of calcium phosphate: Combined experimental and molecular dynamics simulations approach*, ACS Appl. Mater. Interfaces **12** (2020), no. 11 12426–12435. https://doi.org/10.1021/acsami.9b20877.

[79] W. L. Jorgensen, J. Chandrasekhar, J. D. Madura, R. W. Impey, and M. L. Klein, *Comparison of simple potential functions for simulating liquid water*, The Journal of Chemical Physics **79** (1983), no. 2 926–935. https://doi.org/10.1063/1.445869.

[80] I. Chubak, L. Alon, E. V. Silletta, G. Madelin, A. Jerschow, and B. Rotenberg, *Quadrupolar relaxation of $^{23}Na^+$ in solution beyond rotational models: Revealing a link with ultrafast collective dynamics by experiments and simulations*, . https://doi.org/10.48550/ARXIV.2206.05986.

[81] C. Johnson, *Diffusion ordered nuclear magnetic resonance spectroscopy: principles and applications*, Progress in Nuclear Magnetic Resonance Spectroscopy **34** (1999) 203–256.

[82] A. Jerschow and N. MÃŒller, *Suppression of convection artifacts in stimulated-echo diffusion experiments. double-stimulated-echo experiments*, Journal of Magnetic Resonance **125** (1997), no. 2 372–375. https://doi.org/10.1006/jmre.1997.1123.

[83] A. Eiberweiser, A. Nazet, G. Hefter, and R. Buchner, *Ion hydration and association in aqueous potassium phosphate solutions*, *The Journal of Physical Chemistry B* **119** (2015), no. 16 5270–5281.
`https://doi.org/10.1021/acs.jpcb.5b01417`.

[84] M. Gerstein and C. Chothia, *Packing at the protein-water interface*, *Proceedings of the National Academy of Sciences* **93** (1996), no. 19 10167–10172.
`https://doi.org/10.1073/pnas.93.19.10167`.

[85] M. D'Agostino, R. Bougault, F. Gulminelli, M. Bruno, F. Cannata, P. Chomaz, F. Gramegna, I. Iori, N. L. Neindre, G. Margagliotti, A. Moroni, and G. Vannini, *On the reliability of negative heat capacity measurements*, *Nuclear Physics A* **699** (2002), no. 3 795–818. `https://doi.org/10.1016/S0375-9474(01)01287-8`.

[86] D. Marenduzzo, K. Finan, and P. R. Cook, *The depletion attraction: an underappreciated force driving cellular organization*, *Journal of Cellular Biology* **175** (2016), no. 5 681–686. `https://doi.org/10.1083/jcb.200609066`.

[87] A. Bondi, *van der waals volumes and radii*, *The Journal of Physical Chemistry* **68** (1964), no. 3 441–451. `https://doi.org/10.1021/j100785a001`.

[88] S. Park, R. Barnes, Y. Lin, B. Jeon, S. Najafi, K. Delaney, G. Fredrickson, J. Shea, D. Hwang, and S. Han, *Dehydration entropy drives liquid-liquid phase separation by molecular crowding*, *Communications Chemistry* **3** (2020), no. 1 83. `https://doi.org/10.1038/s42004-020-0328-8`.

[89] S. Großhans, G. Wang, and J. Hubbuch, *Water on hydrophobic surfaces: mechanistic modeling of polyethylene glycol-indcued protein precipitation*, *Bioprocess and Biosystems Engineering* **42** (2019), no. 4 513–520. `https://doi.org/10.1007/s00449-018-2054-5`.

[90] Y. Zhang and P. S. Cremer, *Interactions between macromolecules and ions: the hofmeister series*, *Current Opinion in Chemical Biology* **10** (2006), no. 6 658–663. `https://doi.org/10.1016/j.cbpa.2006.09.020`.

[91] H. I. Okur, J. Hladílková, K. B. Rembert, Y. Cho, J. Heyda, J. Dzubiella, P. S. Cremer, and P. Jungwirth, *Beyond the hofmeister series: Ion-specific effects on proteins and their biological functions*, *The Journal of Physical Chemistry B* **121** (2017), no. 9 1997–2014. `https://doi.org/10.1021/acs.jpcb.6b10797`.

[92] H. Cölfen, *Nonclassical nucleation and crystallization*, *Crystals* **10** (2020), no. 2 61. `https://doi.org/10.3390/cryst10020061`.

[93] X. Yang, M. Wang, Y. Yang, B. Cui, Z. Xu, and X. Yang, *Physical origin underlying the prenucleation-cluster-mediated nonclassical nucleation pathways for*

calcium phosphate, Physical Chemistry Chemical Physics **21** (2019), no. 27
14530–14540. `https://doi.org/10.1039/C9CP00919A`.

[94] K. Jiao, L.-N. Niu, C.-F. Ma, X.-Q. Huang, D.-D. Pei, T. Luo, Q. Huang, J.-H. Chen, and F. R. Tay, *Complementarity and uncertainty in intrafibrillar mineralization of collagen*, Adv. Funct. Mater. **26** (2016), no. 38 6858–6875. `https://doi.org/10.1002/adfm.201602207`.

[95] D. Gebauer and S. E. Wolf, *Designing solid materials from their solute state: A shift in paradigms toward a holistic approach in functional materials chemistry*, J. Am. Chem. Soc. **141** (2019), no. 11 4490–4504. `https://doi.org/10.1021/jacs.8b13231`.

[96] A. Leavesley, C. B. Wilson, M. Sherwin, and S. Han, *Effect of water/glycerol polymorphism on dynamic nuclear polarization*, Phys. Chem. Chem. Phys. **20** (2018) 9897–9903. `https://doi.org/10.1039/C8CP00358K,`.

[97] J. Jeon, K. R. Thurber, R. Ghirlando, W.-M. Yau, and R. Tycko, *Application of millisecond time-resolved solid state nmr to the kinetics and mechanism of melittin self-assembly*, PNAS **116** (2019), no. 32 16717–16722. `https://doi.org/10.1073/pnas.1908006116,`.

[98] C. B. Wilson and R. Tycko, *Millisecond time-resolved solid-state nmr initiated by rapid inverse temperature jumps*, J. Am. Chem. Soc. **144** (2022), no. 22 9920–9925. `https://doi.org/10.1021/jacs.2c02704,`.

[99] R. Kaufmann, I. Yadid, and D. Goldfarb, *A novel microfluidic rapid freeze-quench device for trapping reactions intermediates for high field epr analysis*, Journal of Magnetic Resonance **230** (2013), no. 1 220–226. `https://doi.org/10.1016/j.jmr.2013.01.016`.

[100] T. Schmidt, J. Jeon, Y. Okuno, S. C. Chiliveri, and G. M. Clore, *Submillisecond freezing permits cryoprotectant-free epr double electron-electron resonance spectroscopy*, Chem Phys Chem **21** (2020), no. 12. `https://doi.org/10.1002/cphc.202000312`.

[101] Q. D, H. Z, L. P, and Z. S., *Liquid-liquid phase separation in nucleation process of biomineralization*, Front Chem. (2022). `https://doi.org/10.3389/fchem.2022.834503`.

[102] C. M. Sánchez, H. M. Pastawski, and P. R. Levstein, *Time evolution of multiple quantum coherences in nmr*, Physica B: Condensed Matter **398** (2007), no. 2 472–475. `https://doi.org/10.1016/j.physb.2007.04.092`.

[103] Y.-S. Yen and A. Pines, *Multiple-quantum nmr in solids*, J. Chem. Phys. **78** (1983), no. 1 3579. `https://doi.org/10.1063/1.445185`.

[104] D. Suter, S. B. Liu, J. Baum, and A. Pines, *Multiple quantum nmr excitation with a one-quantum hamiltonian*, *Chemical Physics* **114** (1987), no. 1 103–109. https://doi.org/10.1016/0301-0104(87)80023-X.

[105] D. Shykind, J. Baum, S.-B. Liu, A. Pines, and A. Garroway, *Phase-incremented multiple-quantum nmr experiments*, *Journal of Magnetic Resonance* **76** (1988), no. 1 149–154. https://doi.org/10.1016/0022-2364(88)90209-0.

[106] M. Tomaselli, S. Hediger, D. Suter, and R. R. Ernst, *Nuclear magnetic resonance polarization and coherence echoes in static and rotating solids*, *J. Chem. Phys* **105** (1996), no. 24 10672–10681. https://doi.org/10.1063/1.472875.

[107] Y. Ba and W. S. Veeman, *Multiple-quantum nuclear magnetic resonance spectroscopy of coupled 1/2 spins in solids. combination with cross-polarization and magic-angle spinning*, *Solid State Nucl. Magn. Reson.* **3** (1994), no. 5 249–269. https://doi.org/10.1016/0926-2040(94)90002-7.

[108] G. Teymoori, B. Pahari, E. Viswanathan, and M. Edén, *Multiple-quantum spin counting in magic-angle-spinning nmr via low-power symmetry-based dipolar recoupling*, *J. of Magn. Reson.* **236** (2013), no. 1 31–40. https://doi.org/10.1016/j.jmr.2013.08.005.

[109] O. N. Antzutkin and R. Tycko, *High-order multiple quantum excitation in 13 c nuclear magnetic resonance spectroscopy of organic solids*, *J. Chem. Phys.* **110** (1999), no. 6 2749–2752. https://doi.org/10.1063/1.477876.

[110] D. H. Levy and K. K. Gleason, *Multiple quantum nuclear magnetic resonance as a probe for the dimensionality of hydrogen in polycrystalline powders and diamond films*, *J. Phys. Chem.* **96** (1992), no. 20 8125–8131. https://doi.org/10.1021/j100199a056.

[111] B. E. Scruggs and K. K. Gleason, *Multiple-quantum nmr coherence growth in polycrystalline salts containing 19f*, *Journal of Magnetic Resonance* **99** (1992), no. 1 149– 160. https://doi.org/10.1016/0022-2364(92)90161-Y.

[112] P. Bertani, J. Raya, and J. Hirschinger, *19f/29si distance determination and heteronuclear spin counting under fast magic-angle spinning in fluoride-containing octadecasil*, *Comptes Rendus Chimie* **7** (2004), no. 3-4 363–369. https://doi.org/10.1016/j.crci.2003.09.011.

[113] J. Baum and A. Pines, *Nmr studies of clustering in solids*, *J. Am. Chem. Soc.* **108** (1986), no. 24 7447–7454. https://doi.org/10.1021/ja00284a001.

[114] W. V. Gerasimowicz, A. N. Garroway, and J. B. Miller, *Multiple-quantum nmr in a mixture of liquid crystals: differential coherence development*, *J. Am. Chem. Soc.* **112** (1990), no. 10 3726–3730. https://doi.org/10.1021/ja00166a002.

[115] M. Deschamps, F. Fayon, J. Hiet, G. Ferru, M. Derieppe, N. Pellerina, and D. Massiot, *Spin-counting nmr experiments for the spectral editing of structural motifs in solids*, Phys. Chem. Chem. Phys. **9** (2008), no. 10 1298–1303. `https://doi.org/10.1039/B716319C`.

[116] G. Cho and J. P. Yesinowski, *H and 19f multiple-quantum nmr dynamics in quasi-one-dimensional spin clusters in apatites*, J. Phys. Chem. **100** (1996), no. 39 15716–15725. `https://doi.org/10.1021/jp9614815`.

[117] Y. Mogami, S. Yamazaki, S. Matsuno, K. Matsui, Y. Noda, and K. Takegoshi, *Hydrogen cluster/network in tobermorite as studied by multiple-quantum spin counting 1h nmr*, Cement and Concrete Research **66** (2014), no. 1 115–120. `https://doi.org/10.1016/j.cemconres.2014.07.023`.

[118] G. Cho and J. P.Yesinowski, *Multiple-quantum nmr dynamics in the quasi-one-dimensional distribution of protons in hydroxyapatite*, Chemical Physics Letters **205** (1993), no. 1 1–5. `https://doi.org/10.1016/0009-2614(93)85157-J`.

[119] B. C. Gerstein, M. Pruski, and S.-J. Hwang, *Determination of proton densities on silica gel catalyst supports by n-quantum coherence in nmr*, Analytica Chimica Acta **283** (1993), no. 3 1059–1079. `https://doi.org/10.1016/0003-2670(93)80266-N`.

[120] S.-J. Hwang, D. O. Uner, T. S. King, M. Pruski, and B. C. Gerstein, *Characterization of silica catalyst supports by single and multiple quantum proton nmr spectroscopy*, J. Phys. Chem. **99** (1995), no. 11 3697–3703. `https://doi.org/10.1021/j100011a042`.

[121] B. F. Chmelka, J. G. Pearson, S. B. Liu, R. Ryoo, L. C. D. Menorval, and A. Pines, *Nmr study of the distribution of aromatic molecules in nay zeolite*, J. Phys. Chem. **95** (1991), no. 1 303–310. `https://doi.org/10.1021/j100154a056`.

[122] S. J. Hwang, T. S. King, and B. C. Gerstein, *Probing intermediates in the reaction of ethylene over supported ru; use and limitations of multiple quantum spin counting*, Catalysis Letters **8** (1991), no. 1 367–373. `https://doi.org/10.1007/BF00764198`.

[123] R. Ryoo, S. B. Liu, L. C. D. Menorval, K. Takegoshi, B. Chmelka, M. Trecoske, and A. Pines, *Distribution of hexamethylbenzene in a zeolite studied by xenon-129 and multiple-quantum nmr*, J. Phys. Chem. **91** (1987), no. 27 6575–6577. `https://doi.org/10.1021/j100311a003`.

[124] S. B. Hong, H. M. Cho, and M. E. Davis, *Distribution and motion of organic guest molecules in zeolites*, J. Phys. Chem. **97** (1993), no. 8 1622–1628. `https://doi.org/10.1021/j100110a025`.

[125] S. B. Hong, H. M. Cho, and M. E. Davis, *Location and molecular motion of hexamethylbenzene in zeolite nay*, J. Phys. Chem. **97** (1993), no. 8 1629–1633. `https://doi.org/10.1021/j100110a026`.

[126] J. G. Pearson, B. F. Chmelka, D. N. Shykind, and A. Pines, *Multiple-quantum nmr study of the distribution of benzene in nay zeolite*, J. Phys. Chem. **96** (1992), no. 21 8517–8522. `https://doi.org/10.1021/j100200a057`.

[127] J. He, Y. Ba, C. I. Ratcliffe, J. A. Ripmeester, D. D. Klug, J. S. Tse, and K. F. Preston, *Encapsulation of silicon nanoclusters in zeolite y*, J. Am. Chem. Soc. **120** (1998), no. 41 10697–10705. `https://doi.org/10.1021/ja9816133`.

[128] F. Fayon, C. Duée, T. Poumeyrol, M. Allix, and D. Massiot, *Evidence of nanometric-sized phosphate clusters in bioactive glasses as revealed by solid-state 31p nmr*, J. Phys. Chem. **117** (2013), no. 5 2283–2288. `https://doi.org/10.1021/jp312263j`.

[129] H. Geen, R. Graf, A. S. D. Heindrichs, B. S. Hickman, I. Schnell, H. W. Spiess, and J. J. Titman, *Spin counting with fast mas*, J. Magn. Reson. **138** (1999), no. 1 167–172. `https://doi.org/10.1006/jmre.1999.1711`.

[130] K. Saalwächter and H. W. Spiess, *Heteronuclear 1h–13c multiple-spin correlation in solid-state nuclear magnetic resonance: Combining rotational-echo double-resonance recoupling and multiple-quantum spectroscopy*, J. Chem. Phys. **114** (2001), no. 13 5707–5728. `https://doi.org/10.1063/1.1352618`.

[131] J. Baum, M. Munowitz, A. N. Garroway, and A. Pines, *Multiplequantum dynamics in solid state nmr*, J. Chem. Phys. **83** (1985), no. 1 2015–2025. `https://doi.org/10.1063/1.449344`.

[132] M. A. Petrich, K. K. Gleason, and J. A. Reimer, *Structure and properties of amorphous hydrogenated silicon carbide*, Physical Review B **36** (1987), no. 18 9722–9731. `https://doi.org/10.1103/PhysRevB.36.9722`.

[133] K. K. Gleason, M. A. Petrich, and J. A. Reimer, *Hydrogen microstructure in amorphous hydrogenated silicon*, Physical Review B **36** (1987), no. 6 3259–3267. `https://doi.org/10.1103/PhysRevB.36.3259`.

[134] S. W. Boettcher, M. H. Bartl, J. G. Hu, and G. D. Stucky, *Structural analysis of hybrid titania-based mesostructured composites*, J. Am. Chem. Soc. **127** (2005), no. 9721–9730 27. `https://doi.org/10.1021/ja050753r`.

[135] J. Baum, K. K. Gleason, A. Pines, A. N. Garroway, and J. A. Reimer, *Multiple-quantum nmr study of clustering in hydrogenated amorphous silicon*, Physical Review Letters **56** (1986), no. 13 1377–1380. `https://doi.org/10.1103/PhysRevLett.56.1377`.

[136] K. Saalwächter, P. Ziegler, O. Spyckerelle, B. Haidar, A. Vidal, and J.-U. Sommer, *1h multiple-quantum nuclear magnetic resonance investigations of molecular order distributions in polydimethylsiloxane networks: Evidence for a linear mixing law in bimodal systems*, J. Chem. Phys. **119** (2003), no. 6 3468–3482. https://doi.org/10.1063/1.1589000.

[137] W. V. Gerasimowicz, A. N. Garroway, J. B. Miller, and L. C. Sander, *Multiple-quantum nmr studies of monomeric bonded silica phases*, J. Phys. Chem. **96** (1992), no. 3658–3661 9. https://doi.org/10.1021/j100188a020.

[138] S. J. Limb, B. E. Scruggs, and K. K. Gleason, *Distribution and motion of trifluoromethanesulfonate anions in poly(p-hydroxystyrene) and polystyrene films studied by multiple-quantum nmr*, Macromolecules **26** (1993), no. 15 3750–3757. https://doi.org/10.1021/ma00067a005.

[139] B. E. Scruggs and K. K. Gleason, *Analysis of fluorocarbon plasma-treated diamond powders by solid-state fluorine-19 nuclear magnetic resonance*, J. Phys. Chem. **97** (1993), no. 36 9187–9195. https://doi.org/10.1021/j100138a020.

[140] R. Tycko, *Selection rules for multiple quantum nmr excitation in solids: Derivation from time-reversal symmetry and comparison with simulations and 13c nmr experiments*, Journal of Magnetic Resonance **139** (1999), no. 2 302–307. https://doi.org/10.1006/jmre.1999.1776.

[141] J. J. Balbach, Y. Ishii, O. N. Antzutkin, R. D. Leapman, N. W. Rizzo, F. Dyda, J. Reed, and R. Tycko, *Amyloid fibril formation by a16-22, a seven-residue fragment of the alzheimer's -amyloid peptide, and structural characterization by solid state nmr*, Biochemistry **39** (2000), no. 45 13748–13759. https://doi.org/10.1021/bi0011330.

[142] R. Tycko, *Insights into the amyloid folding problem from solid-state nmr*, Biochemistry **42** (2003), no. 11 3151–3159. https://doi.org/10.1021/bi027378p.

[143] N. A. Oyler and R. Tycko, *Multiple quantum 13c nmr spectroscopy in solids under high-speed magic-angle spinning*, J. Phys. Chem. B **106** (2002), no. 33 8382–8389. https://doi.org/10.1021/jp020906m.

[144] O. N. Antzutkin, J. J. Balbach, R. D. Leapman, N. W. Rizzo, J. Reed, and R. Tycko, *Multiple quantum solid-state nmr indicates a parallel, not antiparallel, organization of -sheets in alzheimer's -amyloid fibrils*, PNAS **97** (2000), no. 24 13045–13050. https://doi.org/10.1073/pnas.230315097.

[145] A. J. Dodd and E. R. H. van Eck, *Multiple quantum spin counting techniques with quadrupolar nuclei*, Solid State Nucl. Magn. Reson. **26** (2004), no. 3-4 121–131. https://doi.org/10.1016/j.ssnmr.2004.04.002.

[146] M. Tomaselli, B. H. Meier, M. Riccò, T. Shiroka, and A. Sartori, *A multiple-quantum nuclear magnetic resonance study of interstitial li clusters in lixc60*, J. Chem. Phys. **115** (2001), no. 1 472–476. `https://doi.org/10.1063/1.1377014`.

[147] G. Teymoori, B. Pahari, B. Stevensson, and M. Edén, *Low-power broadband homonuclear dipolar recoupling without decoupling: Double-quantum 13c nmr correlations at very fast magic-angle spinning*, Chemical Physics Letters **547** (2012), no. 1 103–109. `https://doi.org/10.1016/j.cplett.2012.07.053`.

[148] M. H. Levitt, *Symmetry-Based Pulse Sequences in Magic-Angle Spinning Solid-State NMR*. John Wiley Sons, Chichester, UK, 9 ed., 2002.

[149] K. He, M. Sawczyk, C. Liu, Y. Yuan, B. Song, R. Deivanayagam, A. Nie, X. Hu, V. P. Dravid, J. Lu, C. Sukotjo, Y. peng Lu, P. Král, T. Shokuhfar, and R. Shahbazian-Yassar, *Revealing nanoscale mineralization pathways of hydroxyapatite using in situ liquid cell transmission electron microscopy*, Sci. Adv. **6** (2020), no. 47 eaaz7524. `https://doi.org/10.1126/sciadv.aaz7524`.

[150] A. Oyane, K. Onuma, A. Ito, H.-M. Kim, T. Kokubo, and T. Nakamura, *Formation and growth of clusters in conventional and new kinds of simulated body fluids*, Journal of Biomedical Materials Research Part A **64A** (2002), no. 2 339–348. `https://doi.org/10.1002/jbm.a.10426`.

[151] A. Oyane, H.-M. Kim, T. Furuya, T. Kokubo, T. Miyazaki, and T. Nakamura, *Preparation and assessment of revised simulated body fluids*, Journal of Biomedical Materials Research Part A **65A** (2003), no. 2 188–195. `https://doi.org/10.1002/jbm.a.10482`.

[152] L. M. Epasto, T. Georges, A. Selimović, J.-M. Guigner, T. Azaïs, and D. Kurzbach, *Formation and evolution of nanoscale calcium phosphate precursors under biomimetic conditions*, Anal. Chem. **93** (2021), no. 29 10204–10211. `https://doi.org/10.1021/acs.analchem.1c01561`.

[153] A. Equbal, S. K. Jain, Y. Li, K. Tagami, X. Wang, and S. Han, *Role of electron spin dynamics and coupling network in designing dynamic nuclear polarization*, Progress in Nuclear Magnetic Resonance Spectroscopy **126-127** (2021), no. 1 1–16. `https://doi.org/10.1016/j.pnmrs.2021.05.003`.

[154] Y. Li, W. Weng, K. Cheng, P. Du, G. Shen, J. Wang, and G. Han, *Preparation of amorphous calcium phosphate in the presence of poly(ethylene glycol)*, Journal of Materials Science Letters **22** (2003), no. 1 1015–1016. `https://doi.org/10.1023/A:1024741426069`.

[155] K. Ugurbil, H. Holmsen, and R. G. Shulman, *Adenine nucleotide storage and secretion in platelets as studied by 31p nuclear magnetic resonance*, *PNAS* **76** (1979), no. 5 2227–2231. `https://doi.org/10.1073/pnas.76.5.2227`.

[156] S. K. Jain, T. Tabassum, L. Li, L. Ren, W. Fan, M. Tsapatsis, S. Caratzoulas, S. Han, and S. L. Scott, *P-site structural diversity and evolution in a zeosil catalyst*, *J. Am. Chem. Soc.* **143** (2021), no. 4 1968–1983. `https://doi.org/10.1021/jacs.0c11768`.

[157] T. Biedenbänder, V. Aladin, S. Saeidpour, and B. Corzilius, *Dynamic nuclear polarization for sensitivity enhancement in biomolecular solid-state nmr*, *Chemical Reviews* **122** (2022), no. 10 9738–9794. `https://doi.org/10.1021/acs.chemrev.1c00776`.

[158] Y. Tang, Y. Zhou, D. Zhou, Y. Chen, Z. Xiao, J. Shi, J. Liu, and W. Hong, *Electric field-induced assembly in single-stacking terphenyl junctions*, *Journal of the American Chemical Society* **142** (2020), no. 45 19101–19109. `https://doi.org/10.1021/jacs.0c07348`.

[159] A. Equbal, Y. Li, T. Tabassum, and S. Han, *Crossover from a solid effect to thermal mixing 1h dynamic nuclear polarization with trityl-ox063*, *J. Phys. Chem. Lett.* **11** (2020), no. 9 3718–3723. `https://doi.org/10.1021/acs.jpclett.0c00830`.

[160] J. Dubochet and A. McDowal, *Vitrification of pure water for electron microscopy*, *Journal of Microscopy* **124** (1981), no. 3 RP3–RP4. `https://doi.org/10.1111/j.1365-2818.1981.tb02483.x`.

[161] P. Brüggeller and E. Mayer, *Complete vitrification in pure liquid water and dilute aqueous solutions*, *Nature* **288** (1980), no. 1 569–571. `https://doi.org/10.1038/288569a0`.

[162] Y. Xiao, R. Ghosh, and K. K. Frederick, *In-cell nmr of intact mammalian cells preserved with the cryoprotectants dmso and glycerol have similar dnp performance*, *Frontiers in Molecular Biosciences* **28** (2022), no. 1. `https://doi.org/10.3389/fmolb.2021.789478`.

[163] R. Ghosh, Y. Xiao, J. Kragelj, and K. K. Frederick, *In-cell sensitivity-enhanced nmr of intact viable mammalian cells*, *J. Am. Chem. Soc.* **143** (2021), no. 1 18454-18466. `https://doi.org/10.1021/jacs.1c06680`.

[164] A. Baudot, L. Alger, and P. Boutron, *Glass-forming tendency in the system water–dimethyl sulfoxide*, *Cryobiology* **40** (2000) 151–158. `https://doi.org/10.1006/cryo.2000.2234`.

[165] faCellitate, *What are the most commonly used cryoprotectants?*, facellitate.com/what-are-the-most-commonly-used-cryoprotectants/.

[166] R. Paberit, E. Rilby, J. Göhl, J. Swenson, Z. Refaa, P. Johansson, and H. Jansson, *Cycling stability of poly(ethylene glycol) of six molecular weights: Influence of thermal conditions for energy applications*, ACS Appl. Energy Mater. **3** (2020), no. 11 10578–10589. `https://doi.org/10.1021/acsaem.0c01621`.

[167] R. Ghosh, J. Kragelj, Y. Xiao, and K. K. Frederick, *Cryogenic sample loading into a magic angle spinning nuclear magnetic resonance spectrometer that preserves cellular viability*, JoVE **163** (2020) 1–12. `https://doi.org/10.3791/61733`.

[168] M. J. Abraham, T. Murtola, R. Schulz, S. Páll, J. C. Smith, B. Hess, and E. Lindahl, *GROMACS: High performance molecular simulations through multi-level parallelism from laptops to supercomputers*, SoftwareX **1-2** (2015) 19–25. `https://doi.org/10.1016/j.softx.2015.06.001`.

[169] A. Bondi, *van der waals volumes and radii*, The Journal of Physical Chemistry **68** (1964), no. 3 441–451. `https://doi.org/10.1021/j100785a001`.

[170] P. Eastman, J. Swails, J. D. Chodera, R. T. McGibbon, Y. Zhao, K. A. Beauchamp, L.-P. Wang, A. C. Simmonett, M. P. Harrigan, C. D. Stern, R. P. Wiewiora, B. R. Brooks, and V. S. Pande, *OpenMM 7: Rapid development of high performance algorithms for molecular dynamics*, PLoS Computational Biology **13** (2017), no. 7 e1005659. `https://doi.org/10.1371/journal.pcbi.1005659`.

[171] H. C. Andersen, *Rattle: A "velocity" version of the shake algorithm for molecular dynamics calculations*, Journal of Computational Physics **52** (1983), no. 1 24–34. `https://doi.org/10.1016/0021-9991(83)90014-1`.

[172] S. Miyamoto and P. A. Kollman, *Settle: An analytical version of the SHAKE and RATTLE algorithm for rigid water models*, Journal of Computational Chemistry **13** (1992), no. 8 952–962. `https://doi.org/10.1002/jcc.540130805`.

[173] M. Rahbari-Sisakht, M. Taghizadeh, and A. Eliassi, *Densities and viscosities of binary mixtures of poly(ethylene glycol) and poly(propylene glycol) in water and ethanol in the 293.15 - 338.15 K temperature range*, Journal of Chemical & Engineering Data **48** (2003), no. 5 1221–1224. `https://doi.org/10.1021/je0301388`.

[174] C. Combes and C. Rey, *Amorphous calcium phosphates: Synthesis, properties and uses in biomaterials*, Acta Biomaterialia **6** (2010), no. 1 3362–3378. `https://doi.org/10.1016/j.actbio.2010.02.017`.

[175] Y. Zelenova, S. W. Morgan, and G. S. Boutis, *Effects of experimental imperfections on a spin counting experiment*, Solid State Nuclear Magnetic Resonance **53** (2013), no. 1 27–37.
`https://doi.org/10.1016/j.ssnmr.2013.03.003`.

[176] K. Pakravanan, M. R. Roknabadi, F. Farzanegan, A. Hashemzadeh, and M. Darroudi, *Amorphous calcium phosphate nanoparticles-based mouthwash: preparation, characterization, and anti-bacterial effects*, Green Chemistry Letters and Reviews **12** (2019), no. 3 278–285.
`https://doi.org/10.1080/17518253.2019.1643412`.

[177] M. J. Potrzebowski, J. Gajda, W. Ciesielski, and I. M. Montesinos, *Distance measurements in disodium atp hydrates by means of 31p double quantum two-dimensional solid-state nmr spectroscopy*, J. Magn. Reson. **179** (2006), no. 2 173–181. `https://doi.org/10.1016/j.jmr.2005.11.016`.